Alma Mater Studiorum - University of Bologna

DEIS – DEPARTMENT OF ELECTRONICS, COMPUTER SCIENCE AND SYSTEMS

PhD Course in Electronics, Computer Science and Telecommunications

XXIII CYCLE – SCIENTIFIC-DISCIPLINARY SECTOR ING-INF/02

CO-SIMULAZIONE E CO-PROGETTO NON LINEARE / ELETTROMAGNETICO DI LINK A MICROONDE IN AMBIENTI AD ALTO INQUINAMENTO E / O FORTEMENTE DISOMOGENEI

NONLINEAR / ELECTROMAGNETIC CO-SIMULATION AND CO-DESIGN OF MICROWAVE LINKS IN HIGHLY POLLUTED AND / OR STRONGLY INHOMOGENEOUS ENVIRONMENTS

Candidate:

FRANCESCO DONZELLI

Tutor:

Chiar.mo Prof. Ing. VITTORIO RIZZOLI

Advisors:

Prof. Ing. ALESSANDRA COSTANZO

Dott. Ing. DIEGO MASOTTI

PhD Course Coordinator:

Chiar.mo Prof. Ing. PAOLA MELLO

Final Examination Year 2011

NONLINEAR / ELECTROMAGNETIC CO-SIMULATION AND CO-DESIGN OF MICROWAVE LINKS IN HIGHLY POLLUTED AND / OR STRONGLY INHOMOGENEOUS ENVIRONMENTS

To my parents

"The important thing in science is not so much to obtain new facts as to discover new ways of thinking about them"

William Henry Bragg

INTRODUCTION

Background and motivation

In the last decades the progress of the world of ICT research has been used to overtake with unexpected developments: a good example is the introduction of computer-aided design (CAD) in the world of microwave engineering, more than twenty years ago. Initially considered utopian or too elaborated to be easily handled by designers, now CAD represents a solid reality for any kind of project or system performance prediction: that is a triumph for many research groups and their efforts towards the creation of a full abstraction of intricate physical phenomena into programming language. Supported by such faith the author is confident that what is here proposed could have a significant impact on the future state-of-the-art of radio link analysis.

During the last twenty years the world of wireless telecommunications has been exceptionally growing in complexity as well as size: the widespread deployment of high-capacity networks and the proliferation of ubiquitous mobile computing devices such as affordable smart phones is now reality, and has gone hand in hand with decisive innovations in electronics and manufacturing technologies. For example the trend of miniaturization in modern wireless systems has led to a progressive encapsulation of both radiating and digital processing systems into the same module: since there are limits for the miniaturization of discrete electronic components, substrate technologies such as Low Temperature Co-fired Ceramics (LTCC) have become the answer for space-saving strategies permitting the integration of passive and active devices into a single multilayer structure. In Fig. 1-1 two appreciable examples of system integration by means of LTCC technology are depicted:

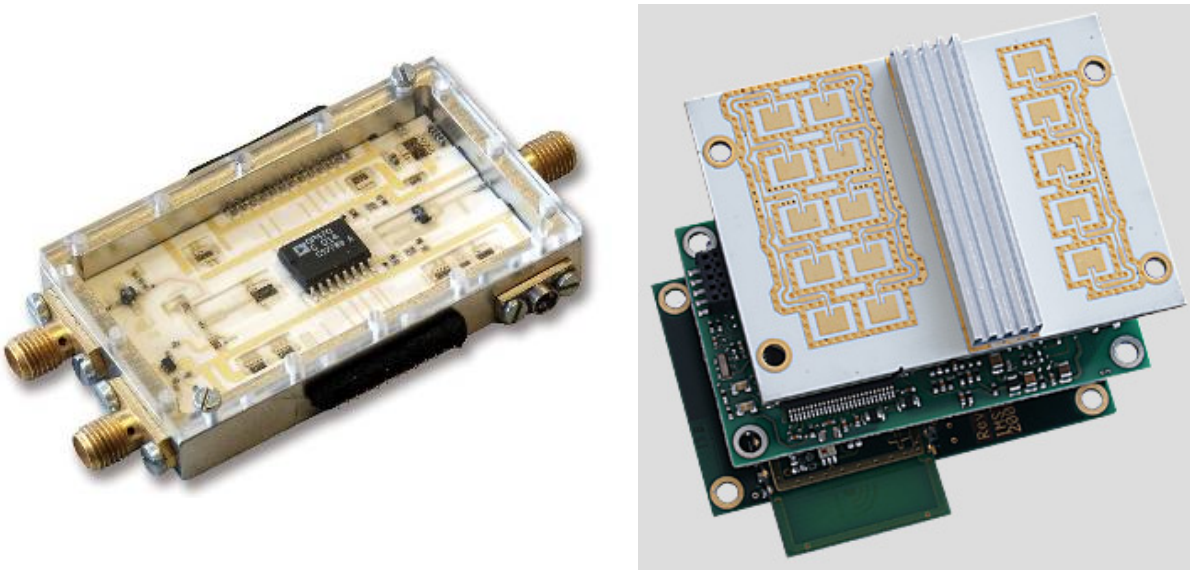

(a) (b)

Fig. 1-1. Two examples of LTCC multilayer technology from IMST GmbH, Germany:
(a) LMDS Transceiver, (b) 24 GHz RADAR sensor

Thus new opportunities have grown as well as challenges for the efficient design, modeling, and optimization of front-end architectures for wireless systems: now circuit simulation softwares have to deal with high-complexity circuit topologies, based on hundreds or thousands of discrete devices. Furthermore electromagnetic (EM) CAD tools have gradually joined traditional circuit simulators for better characterizing frequency-dispersive components and any possibile EM mutual coupling effect not only at the radiation side but among the radiofrequency (RF) chains integrated on a single chip.

In addition new trends are emerging in the world of radio link analysis: the coexistence into humanized environments of different wireless standards has progressively lead to the creation of a densely heterogeneous wireless environment. That implies that even the most simple RF link should be modeled accurately: the sinergy of channel modeling strategies by means of statistical or deterministic approaches is becoming more and more important for the accurate performance evaluation of complex RF and microwave systems, such as Multiple-Input Multiple-Output (MIMO). Not to mention that a special effort should be always put on the evaluation of nonlinear side-effects among the entire chain, such as nonlinear signal distortion or unwanted power transfers between adjacent radio channels due to spectral regrowth.

The purpose of the present Ph.D. thesis is to introduce an omni-comprehensive and rigorous CAD procedure for generic radio systems, answering to all the above needs by a

smart combination of nonlinear, EM and propagation analysis tools. Many different application scenarios are then furnished.

Computer-aided design (CAD): generalities

The development of CAD for RF and microwave circuits dates back to the middle of 1950's, roughly in correspondence with the birth of the computer era. Most of the important early developments in microwave engineering were made possible when the EM environment was made capable of being translated into a computational and efficient description: by that way many physical interactions between devices in terms of electric and magnetic fields were studied and new concepts were tested and optimized. That immediately appeared essential in the universe of microwave engineering in which the most important work hypothesis of the classical electronics – circuit analysis based on lumped element abstraction and voltage-current concepts – often fall down.

During the last three decades advances in numerical techniques for the analysis of nonlinear circuits and systems have marked key improvements in modern circuit simulators: in particular *harmonic balance* (HB) technique has become the basis for the efficient simulation of large-signal steady-state RF/microwave circuits in the mixed time-frequency domain, achieving a great efficiency gain over traditional time-domain simulators like SPICE for steady-state problems.

Nevertheless, today the massive level of integration in RF/microwave integrated circuits (IC) and the enhanced complexity of radio systems require a multilevel multifaceted characterization capable of modeling a variety of heterogeneous effects.

Generally speaking modern microwave and wireless communication systems can be described through a hierarchical modeling procedure as depicted in Fig. 1-2:

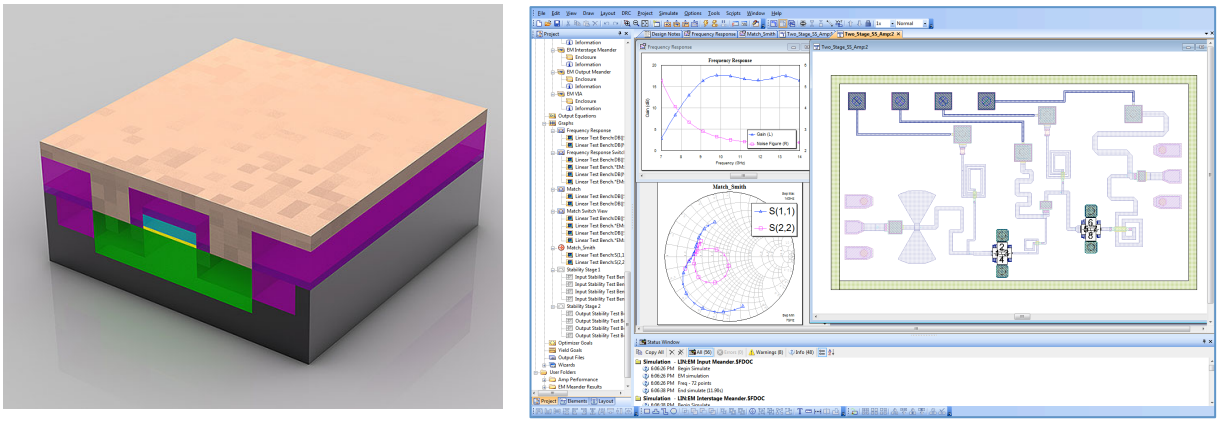

Fig. 1-2. Modeling herarchy for modern RF/microwave IC design and systems: (a) transistor-level, (b) circuit-level, (c) system-level modeling.

At the bottom a device description (*transistor-level*) is made possible by directly approaching the computation of physical phenomena involved into semiconductors. Extremely accurate but hugely time-consuming also, it will not be treated in the thesis work.

At the top a socalled *system-level* description is provided by means of interconnection of behavioural blocks without prior knowledge of their internal circuitry or topology. The result is a very fast simulation approach but intrinsecally inaccurate, especially in relation to the implicit work hypothesis of *unilateral* signal flow along the chain. No industrial process can exclusively rely on such approach.

The *circuit-level* approach stands in between and describes each device behaviour through equivalent-circuit or phenomenological equations. The basis is to have all the subparts meant as electromagnetically shielded from the enviroment and interacting only through their respective terminals in terms of voltage and current. Since no EM coupling or parasitic effect is explicitely accounted for – except for specific components like coupled lines described by

few closed formulas – this kind of analysis is more and more often supported by EM simulation tools: in correspondence of some problematic layout areas a direct Maxwell's equations algebraic calculation is performed among a discretized 2D or 3D domain through an appropriate mesh. *Look-up tables* are still an alternative if provided (e.g. Tee joints in coplanar waveguide technology in Microwave Office Environment).

In order to achieve an exhaustive guideline in the last years several research groups have developed higher-order link-analysis approaches: in Jensen's [1] and Wiesbeck's [2] studies MIMO wireless systems are analyzed replacing a pedestrian antenna description in the form of 50-Ohm-internal-resistance source generator with accurate full-wave EM simulations and emphasizing the mutual coupling effects upon the deformation of the radiation patterns. Such side-effects are then inserted into a suitable link capacity formulation, as well as beamforming.

In [3], [4] limited effects of signal coupling in MIMO radio receiver front-ends are examinated by means of lumped-element equivalent circuits.

Furthermore some authors propose substantial improvements in the classic behavioural modeling of RF/microwave links including nonlinear dynamics and the effects of interference [5], or block mismatches derived by large-signal scattering parameters measurement [6].

But none of these approaches seem to include all these features simultaneously, and additional points are still disregarded, in particular the interaction between the incoming radio signal and the system front-end in terms of polarization mismatch or impact on nonlinear regime perfomances.

The objective of the present Ph.D. thesis is to put the basis of an all-embracing analysis procedure that may form a general reference scheme for the future state-of-the-art of radio link design: it is basically designed as a circuit-level simulation of an entire RF link, with – generally multiple – transmitting and receiving antennas examined by EM analysis. In this way the influence of mutual couplings on the frequency-dependent near-field and far-field performance of each element is fully accounted for. The set of transmitters is treated as a unique nonlinear system loaded by the multiport antenna, and is analyzed by nonlinear circuit techniques. In order to establish the connection between transmitters and receivers, the far fields incident on the receivers are evaluated by EM analysis and are combined by extending an available ray tracing technique to the link study. EM theory is used to describe the receiving array as a linear active multiport network. Link performances in terms of bit-error-rate (BER) are eventually verified *a posteriori* by a fast system-level algorithm.

A complete MIMO link design in a realistic propagation scenario is meant to constitute the reference case study, leaving simpler cases as a natural prosecution.
A first step towards the integration of EM tools and circuit-level simulation was made in [7] with the application of reciprocity theorem in a EM compatibility study. Then in 2006 a first link analysis [8] was developed exploiting an extended version of the algorithm.

REFERENCES

[1] J. W. Wallace, M. A. Jensen, "Mutual coupling in MIMO wireless systems: a rigorous network theory analysis," *IEEE Trans. Wireless Commun.,* Vol. 3, no. 4, pp. 1317-1326, July 2004.

[2] C. Waldschmidt, S. Schultieis, W. Wiesbeck, "Complete RF System Model for Analysis Of Compact MIMO Arrays", *IEEE Trans. Vehicular Tech.,* Vol. 53, no.3, pp. 579-586, May 2004.

[3] M. L. Morris, M. A. Jensen, "Impact of receive amplifier signal coupling on MIMO system performance", *IEEE Trans. Vehicular Tech.,* Vol. 55, no.3, pp. 1678 - 1683, September 2005.

[4] C. Kuhnert, S. Schulteis, A. Hangauer, W. Wiesbeck, "Impact of receiver inter-chain coupling on BER performance of space-time coded MIMO systems", *2006 Vehicular Technology Conference,* pp. 2752 – 2756, Melbourne 2006.

[5] J. Wood, D. Root, N. Tufillaro, "A behavioral modeling approach to nonlinear model-order reduction for RF/microwave ICs and systems", *IEEE Trans. Microwave Theory and Techniques,* Vol. 52, no. 5, pp. 2274 – 2284, September 2004.

[6] F. X. Estagerie, A. Bennadji, T. Reveyrand, S. Mons, R. Quere, L. Constancias, P. Le Helleye, "Implementation of a Behavioral Model of SSPAs taking into account mismatches for efficient System Simulation of Modern AESA", *2007 Asia-Pacific Microwave Conference*, Bangkok, pp. 1 – 4, December 2007.

[7] V. Rizzoli, A. Costanzo, G. Monti, "General electromagnetic compatibility analysis for nonlinear microwave integrated circuits", *2004 IEEE MTT-S Int. Microwave Symp. Digest*, Fort Worth, TX, pp. 953-956, June 2004.

[8] V. Rizzoli, A. Costanzo, D. Masotti, P. Spadoni, "Prediction of the End-to-End Performance of a Microwave/RF Link by means of Nonlinear/Electromagnetic Co-

Simulation", *IEEE Transactions on Microwave Theory Techniques*, Vol. 54, pp. 1149-1160, Dec. 2006.

CIRCUIT-LEVEL ANALYSIS TOOLS

As illustrated in the previous chapter, the aim of the overall approach is to reduce a radio link evaluation to a circuit-level analysis verified a posteriori by a system level fast algorithm. It is essential to rely on a stable circuit-level simulation technique in presence of high-power driving signal and capable to deal with a large number of variables. An accurate description of the well-known HB technique, implemented in the in-house circuit-level simulator Nonlin, is furnished here under.

Harmonic balance (HB): fundamentals and solution algorithms

By the HB technique a nonlinear circuit analysis is reduced to the solution of a nonlinear algebraic system, which is usually obtained by some sort of iterative procedure. Its origins can be ascribed to Galerkin's method in which a solution of a nonlinear system is assumed as a linear combination of a set of basis functions – complex phasors in the present case – with unknown coefficients adjusted to minimize the error in the governing equations. This method was first applied to Kirchoff's current laws for nonlinear circuits by Bailey [1] and Lindenlaub [2] in the 1960's.

A peculiar feature is that, assuming a fully connected electrical network driven by a finite number of sinusoidal tunes, the computation of the transient response is avoided and only the steady state response given by the amplitudes and phases of the sinusoids is required. The choice of HB as circuit-level simulation technique under single and multitone excitation allows to overcome stability troubles of frequency-domain Volterra-series methods – especially for strong nonlinearities – and the huge computational effort requested by the time-domain analysis of dispersive RF/microwave circuits. Nowadays HB is the most widespread technique for the analysis of nonlinear steady-state high-frequency regimes.

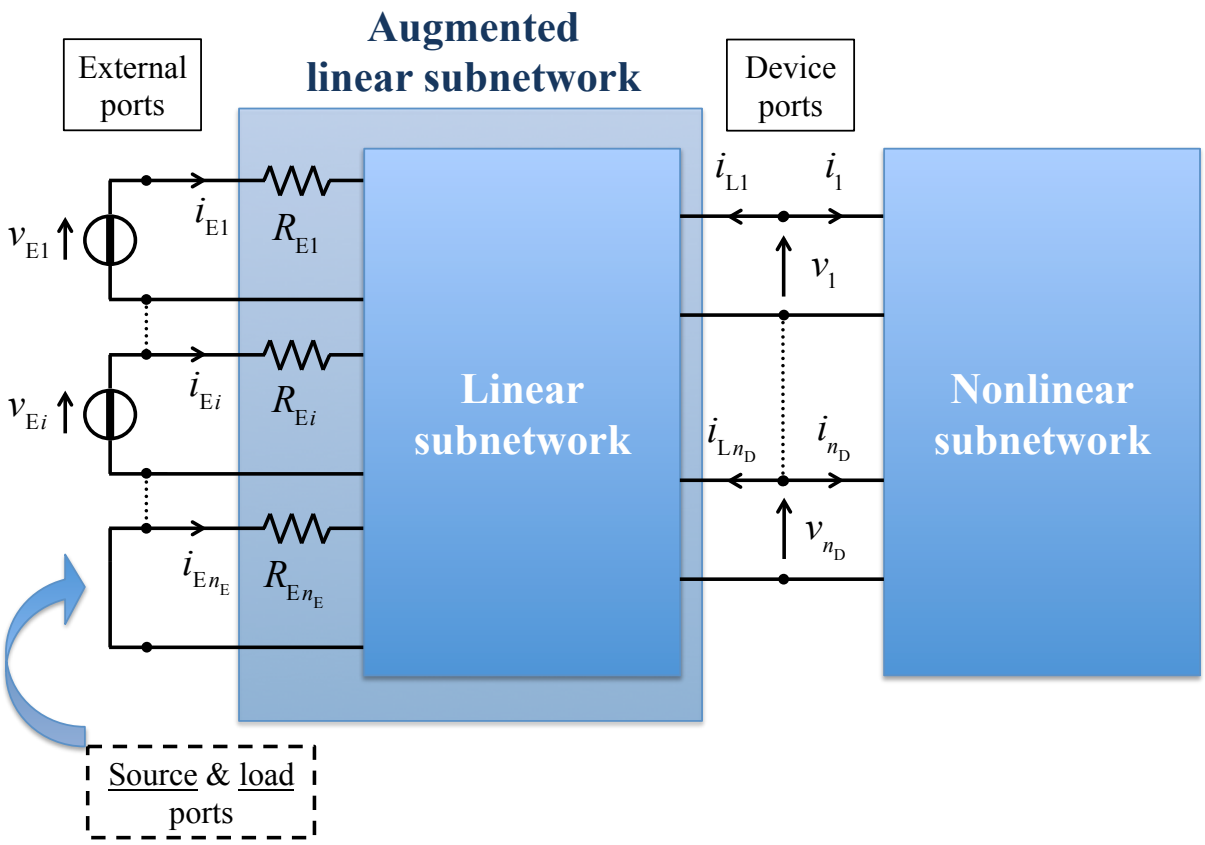

Fig. 2-1. Circuit decomposition for piecewise HB

Let us consider a nonlinear microwave circuit under quasi-periodic steady-state regime generated by the superposition of F sinusoidal tones of incommensurable fundamental angular frequencies ω_i. Any signal $a(t)$ inside the circuit can be expressed as a truncated Fourier series expansion:

$$a(t) = \sum_{\mathbf{k} \in \boldsymbol{S}} \mathbf{A}_{\mathbf{k}} e^{j\Omega_{\mathbf{k}} t} \tag{2.1}$$

where $\Omega_{\mathbf{k}}$ is a generic mixing – *intermodulation* (IM) – product for all the forcing tones, in detail

$$\Omega_{\mathbf{k}} = \sum_{i=1}^{F} k_i \omega_i = \mathbf{k}^{tr} \boldsymbol{\omega} \tag{2.2}$$

In (2.2) k_i is an integer harmonic number, $\mathbf{k}$ is an F-vector of harmonic numbers and $\boldsymbol{\omega}$ is the F-vector of the fundamentals. The vector $\mathbf{k}$ stands for a finite harmonic spectrum overall the

infinite set of linear combinations $\Omega_{\mathbf{k}}$ conventionally named *signal spectrum* S – containing DC-product. We shall denote by S^+ the subset of S such that $\Omega_{\mathbf{k}} \geq 0$ for $\mathbf{k} \in S^+$.

In (2.1) Fourier coefficients $\mathbf{A}_{\mathbf{k}}$ are the harmonic of $a(t)$ at $\Omega_{\mathbf{k}}$, or **k**-th harmonic of $a(t)$. The hermitian simmetry for real signals is still valid: $\mathbf{A}_{-\mathbf{k}} = \mathbf{A}_{\mathbf{k}}^*$, where * stands for the complex conjugate quantity.

The HB technique can be implemented following two different philosophies: the socalled *nodal technique* was first introduced by Kundert and Sangiovanni-Vincentelli in 1986 [3]: Kirchoff's current law is applied to any node of the circuit and the final solving system dimension is given by the product between the cardinality of S and the number of internal nodes. A peculiar feature is that the zero-elements in the final nodal admittance matrix arise in the absence of topological connection between any couple of nodes, resulting in a highly sparse matrix: apposite solving algorithms can thus be straightforwardly integrated in the procedure. The computational effectiveness is demonstrated when the number of devices is limited.

The concurrent *piecewise technique* (Fig. 2-1) was introduced in 1975 by Nachla and Vlach [4]: the approach consists in partitioning the whole circuit into a linear and nonlinear subnetworks respectively, connected by n_{D} device ports. Kichoff's current law is then applied at the interconnection nodes exclusively.

One of the main advantages is the possibility to describe both types of networks in their more suitable reference domain: as for the nonlinear subpart, following a state-variable approach [5] voltages and currents at the common device ports can be expressed by parametric equations depending on a set of time-varying state variables (SV), in the form:

$$\begin{aligned} \mathbf{v}(t) &= \mathbf{u}\left[\mathbf{x}(t), \frac{d\mathbf{x}(t)}{dt}, \ldots, \frac{d^n\mathbf{x}(t)}{dt^n}, \mathbf{x}_{\mathrm{d}}(t)\right] \\ \mathbf{i}(t) &= \mathbf{w}\left[\mathbf{x}(t), \frac{d\mathbf{x}(t)}{dt}, \ldots, \frac{d^n\mathbf{x}(t)}{dt^n}, \mathbf{x}_{\mathrm{d}}(t)\right] \end{aligned} \qquad (2.3)$$

In (2.3) $\mathbf{x}(t)$ is the n_{D}- vector of SV, $\mathbf{x}_d(t)$ is the n_{D}- vector of time-delayed SV, $\mathbf{v}(t)$ and $\mathbf{i}(t)$ are n_{D}- vectors of currents and voltages at the common ports and **u**, **w** are nonlinear

memoryless functions of dimension n_D. The Multiple Fast Fourier Transform (MFFT) is used to compute the **k**-th harmonics $\mathbf{U_k}$ and $\mathbf{W_k}$ of the time-domain response **u**(*t*), **w**(*t*) of the nonlinear subcircuit. Those are compared to the frequency-domain response of the linear circuit, by applying the Kichoff's current law at the interconnection nodes n_D. So let the linear subnetwork be described by the frequency-domain equation – at any IM product $\Omega_\mathbf{k}$

$$\mathbf{I}_{Lk} = \mathbf{Y}(\Omega_\mathbf{k})\mathbf{V}_\mathbf{k} + \mathbf{Y}_\mathbf{T}(\Omega_\mathbf{k})\mathbf{V}_{Ek} = \mathbf{Y}(\Omega_\mathbf{k})\mathbf{V}_\mathbf{k} + \mathbf{N}_\mathbf{k} \tag{2.4}$$

where $\mathbf{Y}(\Omega_\mathbf{k})$ is the admittance matrix at the device ports when all the external ports are short-circuited; $\mathbf{Y}_T(\Omega)$ is the transadmittance matrix of the augmented linear subnetwork – i.e. including the source and load resistances as shown in Fig. 2-1. **N** is a vector containing impressed equivalent Norton sources. $\mathbf{V_k}$ and $\mathbf{V}_{Ek}$ are the vectors of voltage at the device ports and external ports respectively, and $\mathbf{I}_{Lk}$ stands for the vector of currents, where the subscript 'L' denotes the currents entering the *linear* subnetwork ports.

The set of complex HB errors at the generic IM product $\Omega_\mathbf{k}$ has the expression

$$\mathbf{E}_\mathbf{k}(\mathbf{X}) = \mathbf{Y}(\Omega_\mathbf{k})\mathbf{U}_\mathbf{k}(\mathbf{X}) + \mathbf{W}_\mathbf{k}(\mathbf{X}) + \mathbf{N}(\Omega_\mathbf{k}) \tag{2.5}$$

In order to avoid negative frequencies the nonlinear solving system is expressed in terms of real and imaginary parts of the first member of (2.5) for $\mathbf{k} \in \mathcal{S}^+$. Final expression for the solving nonlinear system is

$$\mathbf{E}(\mathbf{X}) = \mathbf{0} \tag{2.6}$$

The system size for (2.6) is $N = n_D(2n_H + 1)$ with n_H the cardinality of the spectrum $\mathcal{S}^+$. **E**: $\Re^N \rightarrow \Re^N$ is supposed to be continously differentiable.

By means of such mixed approach nonlinear subnetwork enjoys a straightforward time-domain characterization, while frequency-dispersive linear components are still expressed in the suitable frequency-domain. The solving matrix is fundamentally dense but regardless of the number of internal nodes, the only affecting parameter is the number of nonlinear devices in the respective subnetwork. That implies also the possibility to integrate generic results of EM simulations by means of simple linear **Y**, **Z**, or **S** matrix: in other words piecewise

technique ensures full compatibility with an accurate characterization of the linear subnetwork in the frequency domain without affecting the nonlinear analysis cost.
The most efficient way to solve (2.6) is to make use of a Newton iteration

$$\mathbf{E}(\mathbf{X}_i) + \mathbf{J}(\mathbf{X}_i)\mathbf{n}_i = \mathbf{0} \qquad , \quad \mathbf{X}_{i+1} = \mathbf{X}_i + \mathbf{n}_i \tag{2.7}$$

coupled with a *globalization algorithm* based on a trust region [6]. If the number of unknows N is too elevated, the continous storage and factorization of the Jacobian matrix $\mathbf{J}(\mathbf{X}) = \partial\mathbf{E}/\partial\mathbf{X}$ can be avoided by generating a sequence of iterates and finding at each step some update $\mathbf{s}_i$ and some *forcing term* f_i $(0 \le f_i < 1)$ so that

$$\left\|\mathbf{E}(\mathbf{X}_i) + \mathbf{J}(\mathbf{X}_i)\mathbf{s}_i\right\| \le f_i \left\|\mathbf{E}(\mathbf{X}_i)\right\| \qquad , \quad \mathbf{X}_{i+1} = \mathbf{X}_i + \mathbf{s}_i \tag{2.8}$$

with f_i as a measure of the allowed deviation of the *inexact* update from the ordinary Newton iteration. ||•|| denotes the Euclidean norm. The N-vector

$$\mathbf{r}_i = \mathbf{E}(\mathbf{X}_i) + \mathbf{J}(\mathbf{X}_i)\mathbf{s}_i \tag{2.9}$$

indicates the socalled *residual* associated with $\mathbf{s}_i$. If $f_i = 0$, $\mathbf{s}_i$ reduces to $\mathbf{n}_i$. $\mathbf{X}_{i+1}$ defines the inexact Newton iteration. The procedure is terminated when the relative error on each element of $\mathbf{E}(\mathbf{X}_i)$ drops below a prescribed threshold.
The forcing term is updated at each step, making use of the formula suggested in [7]:

$$\begin{aligned} f_0 &= 0.5 \\ f_i &= \frac{\left\|\mathbf{E}(\mathbf{X}_i) - \mathbf{E}(\mathbf{X}_{i-1}) - \mathbf{J}(\mathbf{X}_{i-1})\mathbf{s}_{i-1}\right\|}{\left\|\mathbf{E}(\mathbf{X}_{i-1})\right\|} \qquad (i \ge 1) \end{aligned} \tag{2.10}$$

The working principle is to update f_i in a way that it gradually approaches zero-value and therefore the inexact iteration process a gradually ordinary Newton iteration. The advanced

updating procedure through Krylov subspaces is described in [8] and not reported for brevity. This kind of solution approach is known as *inexact Newton harmonic balance* (INHB).

Modulation-oriented harmonic balance (MHB)

The *envelope-* or *modulation-oriented harmonic balance* (MHB) consists in a variation of the ordinary HB in cases of RF/microwave circuits driven by a sinusoidal carrier modulated by an arbitrary baseband signal. The circuit is simulated by a sequence of HB analyses based on a Krylov-subspace method driven by an inexact Newton loop, and suitably modified to account for coupling with a finite number of preceding time instants.

Let us assume that the impressed voltage of the forcing sources are quasi-periodic phase- and amplitude-modulated signals. The modulation laws are transmitted by the nonlinearities to the SV and to any signal waveform supported by the circuit, therefore the following expression is valid for the state vector $\mathbf{x}(t)$:

$$\mathbf{x}(t) = \sum_{\mathbf{k}} \mathbf{X}_{\mathbf{k}}(t) e^{j\Omega_{\mathbf{k}} t} \tag{2.11}$$

where $\Omega_{\mathbf{k}}$ is a generic IM product of a set of incommensurable fundamental frequencies ω_i. The expression of $\Omega_{\mathbf{k}}$ is again (2.2).

The complex quantity $\mathbf{X}_{\mathbf{k}}(t)$ indicates the *complex modulation law* – or *envelope* – or the *time-dependent phasors* of the **k**-th IM product, or the *time-dependent* **k**-*th harmonic* of $\mathbf{x}(t)$. The set of all the time-dependent harmonics $\mathbf{X}_{\mathbf{k}}(t)$ will constitute the *time-dependent spectrum* of $\mathbf{x}(t)$.

It is also assumed that the modulation laws are arbitrary band-limited functions of time for which Fourier-integral representations always exist, e.g.,

$$\mathbf{X}_{\mathbf{k}}(t) = \int_{-\Omega_{\mathrm{B}}}^{\Omega_{\mathrm{B}}} \mathcal{X}_{\mathbf{k}}(\omega) e^{j\omega t} d\omega \tag{2.12}$$

where $\mathcal{X}_{\mathbf{k}}(\omega)$ is not dependent on time. The set of all complex quantities $\mathcal{X}_{\mathbf{k}}(\omega)$ constitutes the *physical spectrum* of $\mathbf{x}(t)$. In this case Ω_{B} must be intended as the largest of the modulation bandwidths for all the signals of interest – thus accounting for the well-known

spectral regrowth nonlinear effects and a possible broadening of the circuit response bandwidth with respect to the excitations.

General approach for situations without bandwidth limitations (except for the assumption that the modulation sidebands of different harmonics do not overlap) has been presented in [9]. For ordinary communication system applications, the modulation laws may be considered baseband functions so Ω_B is intended to be small with respect to any of the IM products of the RF fundamentals:

$$\Omega_B << \Omega_{\mathbf{k}} \tag{2.13}$$

(2.13) states that the electrical regime may be described as a sequence of RF steady states [10]. This condition is obviously violated for $\mathbf{k} = \mathbf{0}$ ($\Omega_0 = 0$), which implies a special treatment for the DC component, as will be discussed later on.

The modulation laws are sampled at a number of uniformly spaced time instants t_n $(1 \le n \le n_S)$, chosen in such a way as to satisfy the sampling theorem. A generic t_n will be conventionally called a *modulation-law sampling* (MS) *instant*. The complex quantities $\mathbf{X}_{\mathbf{k}}(t_n)$ represent the problem unknowns.

According to the piecewise HB technique fundamentals, n_D device ports interconnect a linear and a nonlinear subnetwork into which a circuit is subdivided. The latter is again described by the set of parametric equations (2.3). At a generic angular frequency Ω, the frequency-domain equations of the linear subnetwork are newly in the form (2.4) here recalled:

$$\mathbf{I}_L(\Omega) = \mathbf{Y}(\Omega)\mathbf{V}(\Omega) + \mathbf{Y}_T(\Omega)\mathbf{F}(\Omega) \tag{2.14}$$

with $\mathbf{F}(\Omega)$ as the vector of complex phasors of the free sinusoidal voltage sources of angular frequency Ω connected to the source ports.

The nonlinear subnetwork response to (2.11) is described by the time-dependent harmonics $\mathbf{U}_{\mathbf{k}}(t_n)$, $\mathbf{W}_{\mathbf{k}}(t_n)$. The procedure for their computation by means of MFFT for the case of periodic modulation laws is described in [10]. For aperiodic cases, the envelope derivatives at the MS instants may be approximated by one-sided multipoint incremental rules of the form

$$\left.\frac{d\mathbf{X}_{\mathbf{k}}(t)}{dt}\right|_{t=t_n} \approx \sum_{m=0}^{M} a_m \mathbf{X}_{\mathbf{k}}(t_{n-m}) \tag{2.15}$$

The coefficients a_m are explicitly listed in many mathematical handbooks [11], and may be regarded as known. $M = 3$ was empirically chosen as the default value. Due to (2.15) $\mathbf{U}_{\mathbf{k}}(t_n)$, $\mathbf{W}_{\mathbf{k}}(t_n)$ result being nonlinear functions of $\mathbf{X}_{\mathbf{k}}(t_n)$, $\mathbf{X}_{\mathbf{k}}(t_{n-1})$, ..., $\mathbf{X}_{\mathbf{k}}(t_{n-M})$ for any value of $\mathbf{k}$.

The n_D - vector of time-domain linear currents $\mathbf{i}_L(t)$ may be expressed in terms of with time-dependent harmonics $\mathbf{I}_{Lk}(t)$ – in a form similar to (2.11). More, the physical spectra of $\mathbf{v}(t)$, $\mathbf{i}(t)$, $\mathbf{i}_L(t)$, namely $\mathcal{U}_{\mathbf{k}}(\omega)$, $\mathcal{W}_{\mathbf{k}}(\omega)$, $\mathcal{I}_{Lk}(\omega)$ can be defined starting from a Fourier-integral representations similar to (2.12). From the linear subnetwork equation (2.14) we then obtain:

$$\mathcal{I}_{\mathbf{Lk}}(\omega) = \mathbf{Y}(\Omega_{\mathbf{k}} + \omega)\,\mathcal{U}_{\mathbf{k}}(\omega) + \mathbf{Y}_{\mathbf{T}}(\Omega_{\mathbf{k}} + \omega)\,\mathcal{F}_{\mathbf{k}}(\omega) \tag{2.16}$$

Under the assumption (2.13), if ω is a baseband frequency satisfying $|\omega| \le \Omega_B$, a frequency change by ω will produce a very small modification of the microwave circuit admittances. Thus for all $\mathbf{k} \neq \mathbf{0}$ we may introduce the approximation

$$\mathbf{Y}(\Omega_{\mathbf{k}} + \omega) \approx \mathbf{Y}(\Omega_{\mathbf{k}}) + \left.\frac{d\mathbf{Y}(\Omega)}{d\Omega}\right|_{\Omega=\Omega_{\mathbf{k}}} \omega \tag{2.17}$$

A similar expansion is valid for $\mathbf{Y_T}$. Approximations up to the linear terms are normally acceptable for all practical purposes, but the extension to Taylor expansions containing higher order terms in ω is straightforward. Making use of (2.11), (2.15) and (2.17), $\mathbf{I}_{Lk}(t_n)$ may be directly computed as a function of $\mathbf{X}_{\mathbf{k}}(t_n)$, $\mathbf{X}_{\mathbf{k}}(t_{n-1})$, ..., $\mathbf{X}_{\mathbf{k}}(t_{n-M})$ for any value of $\mathbf{k}$.

(2.17) holds with sufficient accuracy for all $\mathbf{k} \neq \mathbf{0}$. For $\mathbf{k} = \mathbf{0}$ the situation may be quite different, because of the huge time constants of the DC circuit in comparison to those typical in microwave circuit, and mainly due to relatively large DC blocking capacitors and RF chokes. Thus if Ω_B is large enough, the DC modulation laws may operate in fully dynamic conditions, so that the approximation (2.17) may be grossly in error. In order to cope with this problem, a special algorithm has been implemented to compute the DC components (**0**-th

harmonics) of the linear subnetwork response. The step responses at the linear subnetwork ports are evaluated and stored once for all. The excitations are approximated by staircase functions, and the baseband responses for each t_n are simply evaluated by linear superposition. In this way a uniform accuracy is obtained for all values of **k**.

If we now balance the linear and nonlinear currents at all device ports (Fig. 2-1) and all MS instants, we obtain the time-domain equations

$$\mathbf{I}_{\mathbf{Lk}}(t_n) + \mathbf{W}_{\mathbf{k}}(t_n) \overset{\Delta}{=} \mathbf{E}_{\mathbf{k}}(t_n) = \mathbf{0} \tag{2.18}$$

If the time-dependent harmonics $\mathbf{I}_{\mathrm{Lk}}(t_n)$, $\mathbf{W}_{\mathbf{k}}(t_n)$ have been computed exactly, the set of (2.18) via (2.12) would also represent a sufficient condition for the physical spectra $\mathcal{I}_{\mathrm{Lk}}(\omega)$ + $\mathcal{W}_{\mathbf{k}}(\omega)$ to vanish. As a matter of fact the time-dependent harmonics are computed only approximately on the basis of the quasi-stationary assumption (2.13), so that the spectra are balanced only approximately by imposing (2.18). The approximation becomes worse as the modulation laws become faster.

Denoting again by n_{H} the number of significative positive IM products $\Omega_{\mathbf{k}}$ and n_{S} the number of sampling instants, (2.18) becomes a system of n_{T} real equations in n_{T} real unknowns $\mathbf{X}_{\mathbf{0}}(t_n)$, $\Re\left[\mathbf{X}_{\mathbf{k}}(t_n)\right]$ and $\Im\left[\mathbf{X}_{\mathbf{k}}(t_n)\right]$, where

$$\begin{aligned} n_{\mathrm{T}} &= N n_{\mathrm{S}} \\ N &= n_{\mathrm{D}}(2n_{\mathrm{H}} + 1) \end{aligned} \tag{2.19}$$

and

$$\begin{aligned} &\mathbf{E}_{\mathbf{0}}(t_n) = \mathbf{0} \\ &\Re\left[\mathbf{E}_{\mathbf{k}}(t_n)\right] = \mathbf{0} \\ &\Im\left[\mathbf{E}_{\mathbf{k}}(t_n)\right] = \mathbf{0} \qquad (\forall \mathbf{k} : \Omega_{\mathbf{k}} > 0; 1 \le n \le n_{\mathrm{S}}) \end{aligned} \tag{2.20}$$

Owing to the peculiar nature of the errors (2.18), a fast approach to the solution can be devised readily. For a fixed n and all $\mathbf{k}$ let us stack the real and imaginary parts of the errors into a real error vector $\mathbf{E_n}$, and the real and imaginary parts of the complex vector phasors $\mathbf{X_k}(t_n)$ into a vector $\mathbf{S}_n$ of real unknowns unknowns. Recalling that $\mathbf{I_{Lk}}(t_n)$, and thus $\mathbf{E_k}(t_n)$ as well, is a nonlinear function of $\mathbf{X_k}(t_n)$, $\mathbf{X_k}(t_{n-1})$, ... , $\mathbf{X_k}(t_{n-M})$ for all values of $\mathbf{k}$, (2.18) may be rewritten in the synthetic form

$$\mathbf{E}_n\left[\mathbf{S}_n,\mathbf{S}_{n-1},...,\mathbf{S}_{n-M}\right]=\mathbf{0} \qquad , \quad 1\le n\le n_S \tag{2.21}$$

For a given n, (2.21) can be viewed as a real system of N equations in many unknowns (the entries of $\mathbf{S}_n$) with $\mathbf{S}_{n-1}$, ..., $\mathbf{S}_{n-M}$ playing the role of parameters. Thus with a suitable intialization of $\mathbf{S}_{n-1}$, ..., $\mathbf{S}_{n-M}$ for $1 \le n \le M$, (2.21) can be solved as a sequence of n_S independent HB systems of size N. For $n = 1$ a conventional HB system is solved. For $n > 1$ each nonlinear system is modified with respect to an ordinary HB analysis because the unknowns appear in it both in the normal way and through the approximations (2.15) of the envelope derivatives.

If N is relatively large, the nonlinear system associated with each MS instant can be most efficiently solved by a Krylov-subspace method driven by an inexact Newton loop, as is the case for ordinary HB analysis. If the MS instants were uncoupled, the analysis would reduce to a sequence of independent HB analyses, and each Jacobian matrix would be computed by the methods discussed in [12]. As a matter of fact, due to couplings established by (2.15), the Jacobian matrix is considerably more involved than the one obtained for ordinary HB [12], but retains the same formal structure. Thus it is still possible to carry out Jacobian-vector multiplications mostly by the Fast Fourier Transform (FFT). This ensures that Krylov-subspace methods can be applied to modulation-oriented analysis with virtually the same efficiency that is already well established for ordinary multitone harmonic balance [12].

Domain partitioning harmonic balance (DHB)

It is noteworthy to mention two important upgrades in INHB approach: the first one is the *domain partitioning harmonic balance* (DHB) providing for a decomposition of the nonlinear subnetwork into many interconnected subparts. The solution is carried out through the

definition of some auxiliary variables at the block connection ports. Then DHB with *reduced spectra*.

DHB technique has been developed in the last years in order to enhance the efficiency of system-oriented HB simulation. The innovative feature is that it can optimally exploit the block structure of the system to be analysed. In this paragraph, we will give only an overview of this technique; analytical details may be found in [13].

The basic idea is to introduce a set of auxiliary SV consisting of the voltages at the subsystem ports, which creates in the Jacobian matrix a well-defined sparsity pattern. Such sparsity can be effectively exploited in a hierarchical solution approach if ordinary HB techniques are used [14], or in the simultaneous solution for all the unknowns when the HB analysis is performed by Krylov-subspace methods [12]. The overhead introduced by the auxiliary unknowns is normally small, so that important savings of both memory and CPU time are obtained, and really huge simulation tasks may be brought within the reach of even ordinary PC's. All the nonlinear interactions between subsystems are exactly accounted for in the analysis, both in band and out of band, and all the peculiar advantages of SV-based HB analysis are fully retained by the new technique. In particular, an arbitrary number of linear subsystems of any complexity may be included in the system without substantially affecting memory and CPU time requirements.

The technique has been coupled to the envelope-oriented harmonic balance (DHB-MHB) too [9]. In this case, once the circuit has been suitably subdivided into blocks, a further significant enhancement in analysis performance may be obtained by limiting each block's spectrum to the set of lines that are relevant to the block electrical function. In fact, an RF/microwave transceiver would typically consist of interconnected sections that operate at different frequency bands, such as the RF, the intermediate frequency (IF), and baseband sections. This situation is exploited to significantly reduce the overall number of unknowns by DHB algorithm based on a hierarchical domain decomposition. A regular multitone HB analysis with all the IM products of the unmodulated forcing carriers is first performed to identify the subcircuits that operate with similar spectra. This defines the 1st-tier decomposition. The spectrum for each 1st-tier block is automatically redefined by eliminating the negligible lines, and the interblock connection equations are accordingly modified (again, in an automatic way). Within each 1st-tier block a 2nd-tier near-optimal decomposition is then automatically operated by the algorithm discussed in [9]. The carrier(s) modulation is then reintroduced, and the bulk of the simulation is performed by envelope-oriented analysis based on DHB [9].

REFERENCES

[1] E. M. Bailey, “Steady state harmonic analysis of nonlinear networks”, Ph.D. dissertation, Stanford Univ., Stanford, CA 1968.

[2] J. C. Lindenlaub, “An approach for finding the sinusoidal steady state response of nonlinear systems”, *7th Annual Allerton Conf. Circuit and System Theory*, Univ. Illinois, Chicago, 1969.

[3] K. S. Kundert, A. Sangiovanni-Vincentelli, "Simulation of nonlinear circuits in the frequency domain", *IEEE Trans. Computer-Aided Design*, vol. 5, pp. 521-535, October 1986.

[4] M. S. Nakhla, J. Vlach, "A piecewise harmonic-balance technique for determination of periodic response of nonlinear systems", *IEEE Trans. Circuits and Systems.*, vol. 23, pp. 85-91, February 1976.

[5] V. Rizzoli, A. Neri, "State of the art and present trends in nonlinear microwave CAD techniques", *IEEE Trans. Microwave Theory and Techniques,* Vol. 36, pp. 343-365, February 1988.

[6] V. Rizzoli, D. Masotti, F. Mastri, and A. Costanzo, “Multitone intermodulation and RF stability analysis of MEMS switching circuits by a globally convergent harmonic-balance technique,” *Proc. Eur. Microw. Assoc.*, vol. 1, no. 1, pp. 45–54, March 2005.

[7] S. C. Eisenstat, H. F. Walker, “Choosing the forcing terms in an inexact Newton method,” Dept. Math. Statistics, Utah State Univ., Logan, UT, Research Report 6/94/75, June 1994.

[8] V. Rizzoli, F. Mastri, C. Cecchetti, and F. Sgallari, "Fast and robust inexact Newton approach to the harmonic-balance analysis of nonlinear microwave circuits", *IEEE Microwave Guided Wave Lett.*, vol. 7, no. 10, pp. 359-361, October 1997.

[9] V. Rizzoli, E. Montanari, D. Masotti, F. Mastri, “System-Oriented Harmonic-Balance Algorithms for Circuit-Level Simulation”, *IEEE Trans. Computer-Aided Design of Integrated Circuits and Systems*, Vol. 30, pp. 256-269, February 2011.

[10] V. Rizzoli, A. Neri, and F. Mastri, “A modulation-oriented piecewise harmonic-balance technique suitable for transient analysis and digitally modulated signals”, *Proc. 26th European Microwave Conf.* (Prague), pp. 546-550, September 1996.

[11] M. Abramowitz and I. A. Stegun, *Handbook of Mathematical Functions*. New York: Dover, 1965.

[12] V. Rizzoli, F. Mastri, C. Cecchetti, and F. Sgallari, "Fast and robust inexact-Newton approach to the harmonic-balance analysis of nonlinear microwave circuits", *IEEE Microwave Wireless Components and Letters*, Vol. 14, pp. 349-351, July 2004.

[13] V. Rizzoli, A. Lipparini, D. Masotti, and F. Mastri, "Efficient Circuit-Level Analysis of Large Microwave Systems by Krylov-Subspace Harmonic Balance", 2001 *IEEE IMS Int. Microwave Symp. Digest*, Phoenix, AZ, pp. 25-28, May 2001.

[14] V. Rizzoli, C. Cecchetti, A. Lipparini, and F. Mastri. "General purpose harmonic balance analysis of nonlinear microwave circuits under multitone excitation," IEEE Transactions on Microwave Theory Technique, vol. 36, pp. 1650-1660, December 1988.

CIRCUIT-LEVEL NONLINEAR / EM SIMULATION OF A GENERIC MICROWAVE LINK

Motivation

As explained in the first chapter during the last years the many puzzling aspects in modern wireless links design have progressively driven the interest of many research groups into the development of exhaustive procedures for better characterizing RF/microwave wireless systems.

A system-level link simulated under several modulated RF drive – signal plus interferers – is implemented by Pedro and alii in [1]. In this case the communication path analysis is addressed by considering low-pass equivalent behavioural blocks aided by circuit based models. The limited number of nonlinear devices and the radio channel modeled by a simple *path-loss* scheme [2] entail a degree of accuracy considereably low in comparison with the proposed method.

In [3] a simplified numerical transmission chain is enhanced by bilateral nonlinear blocks customized to include mismatches and power reflections always neglected by unilateral system simulators. Such blocks are based on measured large-signal scattering parameters.

Mostly for MIMO systems many authors have already stressed the problem of investigating the link under the assumption of significant near-field couplings between antenna elements, both on receiver and transmitter side. Waldschmidt and alii [4] formulate a channel transfer function with respect to a set of coefficients reporting the interactions between antenna elements in terms of **Z** or **S** matrix transmittance. In particular the whole link is treated as a unique merged **S**-matrices chain: given a voltage level at the transmitter side the influence of near-field mutual couplings is embedded into a scattering matrix for the transmitter and the receiver front-end. Then the antenna properties are calculated by a full-wave EM analysis and the farfield are correlated by a path model including a set of significant rays, each of them characterized by magnitude and phase. Jensen and Wallace [5] focus on a thorough modeling of the entire MIMO channel via the evaluation of antenna-array couplings impact on system performances: again a customized scattering chain matrix for both transmitter and receiver front-ends and wireless channel is furnished.

Some further features such as receiver amplifier signal couplings are automatically considered in [6], [7] by exploiting EM simulations limited to few critical points among the multiple receiver layout. The conclusion is a generic wireless system model in which the

ultimate quality factor signal-to-noise ratio (SNR) turns out to be dependent on electromagnetic couplings, leading also to a correspondence with a reduced channel capacity.

In all these works the attention is dedicated to the determination of channel capacity under polarization diversity – analyzing the impact of the cross-polarized electric field component – therefore assuming antennas and incident waves polarization properties as known: under no circumstances an explicit scalar product between incident and scattered EM field is presented as the reciprocity theorem prescribes. In addition, apparently no effort is put in the evaluation of the impact of EM couplings on the nonlinear steady-state regimes, which imply information also on front-end performances.

Our purposes is to answer to the above issues embracing all the information provided by EM analysis and nonlinear regime into a complete circuit-level link analysis based on HB technique: the core of the approach is to assimilate the radiating elements into the linear subsystem and thus interacting with environmental EM field as a whole. As a consequence the radiated far-field on the transmitter side may be directly computed by MHB technique when the driven signal is a modulated waveform. On the receiver side the circuit-level receiver excitation is directly derived through EM theory from the complex envelope of the incident field on the receiver linear subsystem, which once again includes the receiving antennas. Radio channel characterization is developed by an advanced 3D *Ray-Tracing* (RT) algorithm. A Bit Error Rate (BER) evaluation is eventually performed between transmitted and received digital signal at baseband. The computational efficiency of the overall procedure, particularly critical in case of digitally modulated RF carriers, is guaranteed by exploiting model-reduction techniques based on Krylov subspaces; further improvements are due to recent computational advances in the envelope-oriented HB related on automatic domain partitioning (DHB).

Of course such exhaustive approach is not intended to be a competitor for real-time evaluation algorithm such as *Maximum Likelihood* (ML) estimation technique, but to be applied as a in-depth performance investigator or alternatively for validation purposes. Undoubtedly system designers need a faster link design for their tasks: but any puzzling problematic regarding EM couplings, nonlinear side effects would mean a significative upgrade to an omnicomprehensive approach, like the one presented here. That implies also that the modularity of the proposed approach put the basis for a possible top down design metodology starting from a simplified – e.g. behavioural – link modeling: critical link subparts such as channel description can be simply loaded from the present analysis and inserted into a common commercial tool block chain.

Transmitter analysis

What follows here is a rigorous CAD implementation of the proposed approach by considering a generic case of a multiple-input multiple-output (MIMO) wireless link: less complex cases just follow accordingly.

Fig. 3-1 shows a block representation of a multiple transmitter including the antenna array. The multiple RF/microwave front ends are described as a unique nonlinear system consisting of an arbitrary set of nonlinear devices interconnected by a linear subnetwork.

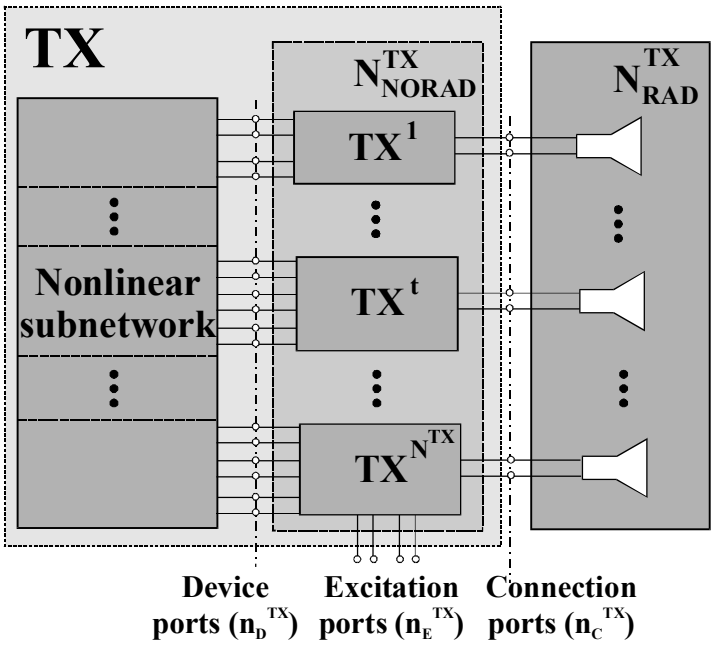

Fig. 3-1. Block diagram of a generic multiple-antenna transmitter

The piecewise HB technique is the chosen tool for circuit-level analysis: the linear and nonlinear subnetworks are connected by $n_{\mathrm{D}}^{\mathrm{TX}}$ device ports where

$$n_{\mathrm{D}}^{\mathrm{TX}} = \sum_{t=1}^{\mathrm{N}^{\mathrm{TX}}} n_{\mathrm{D}}^{t} \tag{3.1}$$

N^{TX} is the number of transmitters, and n_{D}^{t} is the number of device ports belonging to the *t*-th transmitter. The linear subnetwork is referred to as $\mathrm{N}_{\mathrm{NORAD}}^{\mathrm{TX}}$ and is treated by conventional circuit analysis algorithms.

The antenna array is referred to as $\mathrm{N}_{\mathrm{RAD}}^{\mathrm{TX}}$. According to the favourable characteristics of piecewise HB technique it is possible to describe the whole radiating system by means of an exhaustive full-wave EM analysis without affecting HB computational efficiency. This analysis simultaneously provides the antenna scattering matrix and the three-dimensional far-field radiation pattern at all frequencies of interest. The $\mathrm{N}_{\mathrm{NORAD}}^{\mathrm{TX}}$ ports may be grouped into three sets, as shown again in figure, namely, $n_{\mathrm{D}}^{\mathrm{TX}}$ ports for nonlinear device connection, $n_{\mathrm{E}}^{\mathrm{TX}}$ excitation ports, and $n_{\mathrm{C}}^{\mathrm{TX}}$ ports for connection to the $\mathrm{N}_{\mathrm{RAD}}^{\mathrm{TX}}$ network.

The voltages or currents at the third group of ports – as computed by nonlinear analysis of the transmitters – represent the antenna array excitation. In this way the array excitation is automatically embedded into the HB analysis, and any power transfer effect – or reflection due to mismatch - between the antenna elements and nonlinear subsystems is rigorously acconted for.

Let us now assume that each transmitter front end is excited by a sinusoidal IF signal of angular frequency $\omega_{\mathrm{IF}}^{\mathrm{TX}}$ and by a sinusoidal local oscillator (LO) of angular frequency $\omega_{\mathrm{LO}}^{\mathrm{TX}}$. The resulting large-signal regime will be quasi-periodic with spectral lines at all the IM products

$$\Omega_{\mathbf{k}}^{\mathrm{TX}} = k_1 \omega_{\mathrm{IF}}^{\mathrm{TX}} + k_2 \omega_{\mathrm{LO}}^{\mathrm{TX}}; \qquad \mathbf{k} = \begin{bmatrix} k_1 & k_2 \end{bmatrix}^{tr} \tag{3.2}$$

where the k_i's are integer harmonic numbers. A multitone HB analysis may be carried out by well-known algorithms to compute the $n_{\mathrm{D}}^{\mathrm{TX}}$ - vectors of the voltage harmonics at the transmitter device ports, namely $\mathbf{X}_{\mathbf{T},\mathbf{k}}$, at all discrete lines defined by (3.2). One of the spectral lines is the RF frequency ω_{RF} of the signal to be transmitted, which will be obtained for some **k**, say **k** = **s** – alternatively $\omega_{\mathrm{RF}} = \Omega_{\mathbf{s}}^{\mathrm{TX}}$. After carrying out an HB analysis of the transmitter, the complex phasors of the currents flowing out of the n_{T} connection ports may be expressed from the linear subnetwork equations as

$$-\mathbf{I}_{\mathbf{s}}^{\mathrm{TX}} = \mathbf{Y}_{\mathrm{DT}}^{\mathrm{TX}}\left(\omega_{\mathrm{RF}}\right)\mathbf{X}_{\mathbf{s}}^{\mathrm{TX}} + \mathbf{Y}_{\mathrm{TT}}^{\mathrm{TX}}\left(\omega_{\mathrm{RF}}\right)\mathbf{V}_{\mathbf{s}}^{\mathrm{TX}} \tag{3.3}$$

directly following (2.4).

$\mathbf{Y}_{\mathrm{DT}}^{\mathrm{TX}}$ is the $[n_{\mathrm{D}}^{\mathrm{TX}} \times n_{\mathrm{C}}^{\mathrm{TX}}]$ admittance submatrix of the $\mathrm{N}_{\mathrm{NORAD}}^{\mathrm{TX}}$ network relating the device ports to the connection ports, $\mathbf{Y}_{\mathrm{TT}}^{\mathrm{TX}}$ is the $[n_{\mathrm{C}}^{\mathrm{TX}} \times n_{\mathrm{C}}^{\mathrm{TX}}]$ admittance submatrix seen from the connection ports, and $\mathbf{V}_{\mathbf{s}}^{\mathrm{TX}}$ is the vector of voltage phasors at the connection ports. Furthermore, if $\mathbf{Y}_{\mathrm{A}}^{\mathrm{TX}}$ is the $[n_{\mathrm{C}}^{\mathrm{TX}} \times n_{\mathrm{C}}^{\mathrm{TX}}]$ admittance matrix of the multi-element antenna resulting from EM analysis, we have

$$\mathbf{I}_{\mathbf{s}}^{\mathrm{TX}} = \mathbf{Y}_{\mathrm{A}}^{\mathrm{TX}}\left(\omega_{\mathrm{RF}}\right)\mathbf{V}_{\mathbf{s}}^{\mathrm{TX}} \tag{3.4}$$

By combining (3.3) and (3.4) we obtain

$$-\mathbf{V}_{\mathbf{s}}^{\mathrm{TX}} = \left[\mathbf{Y}_{\mathrm{A}}^{\mathrm{TX}}\left(\omega_{\mathrm{RF}}\right) + \mathbf{Y}_{\mathrm{TT}}^{\mathrm{TX}}\left(\omega_{\mathrm{RF}}\right)\right]^{-1}\mathbf{Y}_{\mathrm{DT}}^{\mathrm{TX}}\left(\omega_{\mathrm{RF}}\right)\mathbf{X}_{\mathbf{s}}^{\mathrm{TX}} \tag{3.5}$$

For the *t*-th array element, with the assumption of free-space propagation, we may then express the total radiated field at ω_{RF} in the form [8]:

$$\mathbf{E}_{\mathbf{T}}^{t}\left(r,\theta,\phi;\omega_{\mathrm{RF}}\right) = \frac{\exp\left(-j\beta r\right)}{r}\left[A_{\theta}^{t}\left(\theta,\phi;\omega_{\mathrm{RF}}\right)\hat{\boldsymbol{\theta}} + A_{\phi}^{t}\left(\theta,\phi;\omega_{\mathrm{RF}}\right)\hat{\boldsymbol{\phi}}\right]V_{\mathbf{s}}^{\mathrm{TX},t} \tag{3.6}$$

where A_{θ}^{t}, A_{ϕ}^{t} are the scalar components of the normalized field in a spherical coordinate system with origin in the phase center $\mathrm{O_T}$ of the transmitting array. $\hat{\boldsymbol{\theta}}$, $\hat{\boldsymbol{\phi}}$ are the unit vectors in (θ,ϕ) directions respectively. Such components are generated by EM simulation with a unit-voltage sinusoidal source of angular frequency ω_{RF} connected to the *t*-th port and the remaining ports short-circuited. In this way the actual frequency-dependent array admittance and the *embedded radiation pattern* of each array element become available and can be combined with any suitable channel description tool such as the ray-tracing algorithm.

In case of a digitally-modulated-carrier driving signal at the transmitter side, due to the circuit nonlinearity modulation law is transferred onto all IM products of the carrier frequencies. The transmitter front-end state $\mathbf{x}_{\mathrm{T}}(t)$ may thus be represented – converting (2.11) in suitable vectorial form – for time-dependent complex envelopes:

$$\mathbf{x}_{\mathbf{T}}(t) = \sum_{\mathbf{k}} \mathbf{X}_{\mathbf{T},\mathbf{k}}(t)\, e^{\,j\Omega_{\mathrm{T},\mathbf{k}}\, t} \tag{3.7}$$

Any signal waveform internally supported by the circuit can be modeled through a similar expression. In such conditions, the circuit may be analysed by MHB, whereby the circuit simulation is reduced to a sequence of multitone harmonic-balance analyses associated with the envelope sampling instants and backwards-coupled through the envelope dynamics. In principle, the linear subnetwork response should be exactly evaluated by time-domain convolution but a simplified and much more efficient approach based on the Taylor expansion of the linear subnetwork circuit matrices in the neighborhood of each IM product $\Omega_{\mathrm{T},\mathbf{k}}$ ($\mathbf{k} \neq \mathbf{0}$) is allowed if the relative signal bandwidth is not too broad (i.e., up to about 20% of the RF carrier) [9]. In such cases, the envelope-oriented harmonic-balance technique allows frequency-domain phasor equations to be directly converted into equivalent time-domain equations among complex envelopes. This is also true for the far-field envelope from the *t*-th transmitter, which may be treated just as any other linear subnetwork response:

$$\mathbf{E}_{\mathbf{T}}^{t}\left(r,\theta,\phi;t\right) \approx \frac{\exp\left(-j\beta r\right)}{r}\, \mathbf{A}_{\mathbf{T}}^{t}\left(\theta,\phi;\omega_{RF}\right) \bullet \mathbf{V}_{\mathbf{s}}^{\mathrm{TX},t}\left(t\right) - j\,\frac{1}{r}\,\frac{d\left[\exp\left(-j\beta r\right)\mathbf{A}_{\mathbf{T}}^{t}\left(\theta,\phi;\omega\right)\right]}{d\omega}\bigg|_{\omega_{\mathrm{RF}}} \bullet$$
$$\bullet\, \frac{d\,\mathbf{V}_{\mathbf{s}}^{\mathrm{TX},t}\left(t\right)}{dt} - \frac{1}{r}\,\frac{d^{2}\left[\exp\left(-j\beta r\right)\mathbf{A}_{\mathbf{T}}^{t}\left(\theta,\phi;\omega\right)\right]}{d\omega^{2}}\bigg|_{\omega_{\mathrm{RF}}} \bullet \frac{d^{2}\mathbf{V}_{\mathbf{s}}^{\mathrm{TX},t}\left(t\right)}{dt^{2}} \tag{3.8}$$

with

$$\mathbf{A}_{\mathbf{T}}^{t}\left(\theta,\phi;\omega\right) = \hat{\boldsymbol{\theta}}\mathrm{A}_{\theta}^{t}\left(\theta,\phi;\omega\right) + \hat{\boldsymbol{\phi}}\mathrm{A}_{\phi}^{t}\left(\theta,\phi;\omega\right) \tag{3.9}$$

Note that for our present purposes, the expansions should include up to the quadratic terms, because antennas are normally resonant systems.

Non-ideal radio channel characterization

For a generic link study multiple path phenomenon is taken for granted: RF/microwave signals will reach the receiving antenna from the transmitter by two or more paths: as usual

causes of multipath generally include ionospheric reflection and refraction and reflection from water bodies and terrestrial objects such as mountains, buildings or ground.

The ability of *Ray Tracing* (RT) models to describe with precision a multipath scenario and thus the time- and angle-dispersion of the radio signal is particularly appreciated in the analysis of MIMO systems, where a massive exploitation of diffraction and reflection phenomena is adopted to increase the transmission capacity of the radio channel. Generally speaking, RT technique can be described as a deterministic site modeling through a 2D or 3D computer model of propagation environment. The response of the model to electromagnetic excitation can be straightforwardly computed through computational techniques. The technique is thus based on geometrical optics, supplemented by diffraction theory to enhance accuracy in shadowed regions. Although RT models are presently recognized among the most appropriate field prediction tools for the study and planning of radio systems in complex propagation environments, the main obstacle to their widespread use has been the need for a detailed 3D database of the environment. However, this requirement is now becoming less and less critical thanks to the steadily increasing availability of digitized maps or commercially available urban maps obtained through aerophotogrammetry.

In the present case a three-dimensional RT model developed at the Villa Griffone Laboratories (VGRL) has been embedded into link analysis procedure. From a computational standpoint VGRL's RT algorithm consists of two steps, 1) the creation of a visibility tree, 2) a backtracking procedure. Details can be found in [10].

As soon as the rays from the transmitter to the receiver are tracked, each of them is associated with its coherent vector field $\mathbf{E_T}$, and influenced by reflection and diffraction coefficients – according to geometric optics and theory of diffraction. Of course a loyable database is requested, containing measured data about the material conductivity c [S/m] and the dieletric constant ε_r.

Therefore, the electric field of each radio path (ray) is represented by a complex vector, which depends on the travelled distance and on the interactions (reflections, diffractions, etc.) experienced by the propagating wave.

More specifically, in the present work the so called *narrowband array* assumption is made: the multipath pattern is assumed to be unique for a given couple of transmit/receive phase-centre positions. By tracing all the rays between the two radio terminals a multidimensional characterization of the array-dependent MIMO channel matrix is derived. Let (θ_D, ϕ_D) be the initial – departure – direction of the q-th ray with respect to a local reference system on the transmitter side. The far-field $\mathbf{E}_\mathbf{T}^{q,t}(r_D, \theta_D, \phi_D; \omega_{RF})$ radiated by the t-

th antenna on the q-th ray at a reference distance r_{D} – conventionally chosen as 1 m – in the direction $(\theta_{\mathrm{D}}, \phi_{\mathrm{D}})$ is computed by (3.8), and represents the input to the RT algorithm for the ray under consideration. Considering the q-th ray path and its interactions with obstacles in terms of interaction losses, spreading factors, and phase shifts, the corresponding field incident on the phase centre of the receiving array and referred to the position of its r-th element is given by

$$\mathbf{E}_{\mathbf{R}}^{r,q,t}\left(r_{A},\theta_{\mathrm{A}},\phi_{\mathrm{A}};\omega_{\mathrm{RF}}\right)=\Gamma^{q,t}\left(s_{1}^{q},..,s_{i}^{q},..,s_{\mathrm{N^q}}^{q}\right)\ \underline{\underline{\mathbf{D}}}\ \mathbf{E}_{\mathbf{T}}^{q,t}\left(r_{\mathrm{D}},\theta_{\mathrm{D}},\phi_{\mathrm{D}};\omega_{\mathrm{RF}}\right)e^{\pm j\beta d^{r,q,t}} \tag{3.10}$$

The field on the left-hand side of (3.10) is described in a reference frame local to the receiver, with $(\theta_{\mathrm{A}}, \phi_{\mathrm{A}})$ representing the direction of arrival of the q-th ray and r_{A} the distance at which $\mathbf{E}_{\mathbf{R}}^{r,q,t}(\cdot)$ is evaluated. The right-hand side of (3.10) provides an explicit formulation of the propagation effects along the ray. Γ^{q} is the *scalar spreading factor* accounting for the natural attenuation of the field as it propagates along the ray. The q-th ray is a piecewise straight line consisting of N^{q} cascaded segments, and s_{l}^{q} is the length of the ℓ-th of such segments. The exponential factor accounts for the phase shift along the q-th ray between the t-th transmitting and the r-th receiving antenna element. The distance $d^{r,q,t}$ is the overall ray length taking into account the antenna element positions referred to their respective phase centers. Finally, $\underline{\underline{\mathbf{D}}}$ is a dyadic accounting for the effect of ray interactions (reflections, diffractions, etc.) which may be cast in the form

$$\underline{\underline{\mathbf{D}}}=\left[\prod_{\ell=\min\left\{\mathrm{l},\mathrm{N^{q,t}}\right\}}^{\mathrm{N}^{q}}\underline{\underline{\mathbf{D}}}_{\ell}^{q}\right] \tag{3.11}$$

where $\underline{\underline{\mathbf{D}}}_{\ell}^{q}$ is an appropriate dyadic which decomposes the field into orthogonal components at the ℓ-th interaction point and incorporates the proper interaction coefficients [11].

The peculiar feature of the RT model is its natural ability to accurately describe the multipath nature of the radio link, including its angular spreading which is fundamental for MIMO performance. Obviously simpler cases such Line-of-Sight (LOS) or single-ray radio channels follow as a natural prosecution.

It is worth to mention that the hybrid-domain circuit simulation tools – especially modulated-oriented harmonic balance algorithm – are also full compatible with statistical channel models based on time-domain characterizations. Therefore less accurate but relatively faster link analysis can be straightforwardly implemented.

All the information provided by the analysis of the non-ideal radio channel is fed into the receiver analysis.

Receiver analysis

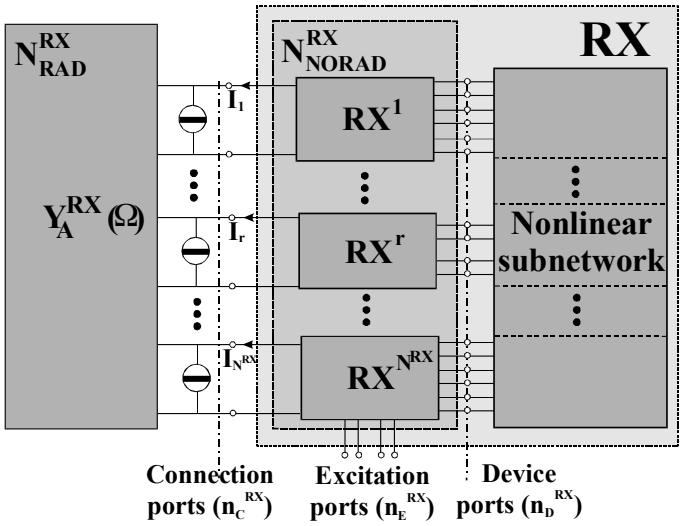

Fig. 3-2. Block diagram of a generic multiple-antenna receiver

The receiver analysis (Fig. 3-2) is oriented on the conversion of the incoming EM field into a correct equivalent independent source, rigorously embracing the interaction between environment and receiver antenna system. Then the whole analysis is again perfomed by piecewise harmonic balance technique with the linear subnetwork matrix developed through full-wave analysis.

In order to define the channel transfer matrix, the receiver excitation can be computed as function of a suitable channel description. The multiple receiving front end is described by the block diagram shown in fig. above. In this case n_C^{RX} connection ports between the N_{RAD}^{RX} and the N_{NORAD}^{RX} linear subnetworks are used to transfer the signal received by the array to the N^{RX} receivers. The receiving array is again characterized by a frequency-domain 3-D EM simulation, and the corresponding ($n_C^{RX} \times n_C^{RX}$) admittance matrix $\mathbf{Y}_A^{RX}$ is computed at each frequency of interest.

The q-th ray radiated by the t-th element of the transmitting antenna will excite voltages and currents in the receiver array. In such conditions the $\mathrm{N}_{\mathrm{RAD}}^{\mathrm{RX}}$ network is active, though linear, and may be represented by a Norton equivalent circuit as in (2.4), which leads to the circuit equations

$$\mathbf{I}_{\mathbf{s}}^{\mathrm{RX},q,t} = \mathbf{Y}_{\mathrm{A}}^{\mathrm{RX}}\left(\omega_{\mathrm{RF}}\right)\mathbf{V}_{\mathbf{s}}^{\mathrm{RX},q,t} + \mathbf{J}_{\mathbf{s}}^{\mathrm{RX},q,t} \tag{3.12}$$

$\mathbf{J}_{\mathbf{s}}^{\mathrm{RX},q,t}$ is the vector of unknown Norton current sources at the $n_{\mathrm{C}}^{\mathrm{RX}}$ connection ports, representing the circuit equivalent of the incident field associated with the channel path under consideration. In order to find $\mathbf{J}_{\mathbf{s}}^{\mathrm{RX},q,t}$, for each array port we make use of a two-step procedure based on the reciprocity theorem. In the first step we suppress the incident ray, and operate the receiving array in a transmitting mode. The array is now fed by a unit voltage source connected to the r-th port, and all remaining ports are short-circuited. In such conditions the normalized radiated far-field $\mathbf{E}_{\mathbf{RN}}^{r}\left(\theta_{\mathrm{A}}', \phi_{\mathrm{A}}'; \omega_{\mathrm{RF}}\right)$ – i.e., the physical field multiplied by $re^{j\beta r}$ – and the input admittance parameters Y_{TT}^{r} are computed by EM analysis. Here, $(\theta_{\mathrm{A}}', \phi_{\mathrm{A}}')$ are the angular coordinates of the ray direction of arrival in a receiver-referred spherical reference frame. In the second step we reintroduce the incident field and short-circuit all the antenna ports, so that the entries of $\mathbf{J}_{\mathbf{s}}^{\mathrm{RX},q,t}$ coincide with the port currents. Such currents may then be expressed by a straightforward application of the reciprocity theorem. Specifically, for the q-th path due to the t-th element, the r-th entry of $\mathbf{J}_{\mathbf{s}}^{\mathrm{RX},q,t}$ may be cast in the form:

$$J_{\mathbf{s}}^{r,q,t} = j\frac{2}{\eta}\lambda\, Y_{\mathrm{TT}}^{r}\, \mathbf{E}_{\mathbf{RN}}^{r}\left(\theta_{\mathrm{A}}', \phi_{\mathrm{A}}'; \omega_{\mathrm{RF}}\right) \bullet \mathbf{E}_{\mathbf{R}}^{r,q,t}\left(r_A, \theta_{\mathrm{A}}, \phi_{\mathrm{A}}; \omega_{\mathrm{RF}}\right) \quad , \quad \left(1 \le r \le \mathrm{N}^{\mathrm{RX}}\right) \tag{3.13}$$

A superposition of the contributions spanning all the incoming wireless paths finally yields the current source at the r-th port:

$$J_{\mathbf{s}}^{r} = \sum_{t=1}^{\mathrm{N}^{\mathrm{TX}}} \sum_{q=1}^{\mathrm{N}_{\mathrm{RAY}}^{t}} J_{\mathbf{s}}^{r,q,t} \tag{3.14}$$

where N_{RAY}^{t} is the number of channel paths originating from the t-th transmitter element. This method allows the actual receiver excitations to be exactly computed with the multiple receiver terminated by the EM-generated frequency-dependent receiver array impedance matrix. For a given channel scenario this procedure may thus be used to efficiently compute the impact of different antenna structures and relative positions on receiver performance.

We may now express each current J_s^r ($1 \le r \le N^{RX}$) as a linear combination of the voltages V_s^t ($1 \le t \le N^{TX}$). In other words, we have established a linear map between the vector $\mathbf{J}_s^{RX}$ of the receiver excitation currents at the receiving antenna ports and the vector $\mathbf{V}_s^{TX}$ of the transmitting antenna excitation voltages. If we cast this map in the form

$$\mathbf{J}_s^{RX} = \mathbf{H}(\omega_{RF})\,\mathbf{V}_s^{TX} \tag{3.15}$$

the complex ($N^{RX} \times N^{TX}$) matrix $\mathbf{H}(\omega_{RF})$ represents our definition of the channel transfer matrix. Unlike previous approaches to the same problem, $\mathbf{H}(\omega_{RF})$ simultaneously accounts for selective fading due to multipath propagation in the channel and for all electromagnetic couplings existing between the transmitting and receiving antennas. This result is believed to mark a considerable advance in MIMO link simulation techniques.

At this stage, we write the receiver N_{NORAD}^{RX} equations in a way similar to (3.3), namely

$$-\mathbf{I}_s^{RX} = \mathbf{Y}_{DT}^{RX}\left(\omega_{RF}\right)\mathbf{X}_s^{RX} + \mathbf{Y}_{TT}^{RX}\left(\omega_{RF}\right)\mathbf{V}_s^{RX} \tag{3.16}$$

where the superscript 'RX' stands for "receiver", and the meanings of all quantities are otherwise identical to those appearing in (3.3).

When the incident field is modulated (with a carrier frequency ω_{RF}), constant complex phasors are replaced by time-dependent complex envelopes. By an argument similar to the one developed in the transmitter analysis, we may cast the vector of Norton source envelopes in the form

$$\mathbf{J}_{\mathbf{s}}^{\mathrm{RX}}(t) \approx \mathbf{H}(\omega_{\mathrm{RF}})\mathbf{V}_{\mathbf{s}}^{\mathrm{TX}}(t) - j\left.\frac{d\mathbf{H}(\omega)}{d\omega}\right|_{\omega_{\mathrm{RF}}} \frac{d\mathbf{V}_{\mathbf{s}}^{\mathrm{TX}}(t)}{dt} - \left.\frac{d^2\mathbf{H}(\omega)}{d\omega^2}\right|_{\omega_{\mathrm{RF}}} \frac{d^2\mathbf{V}_{\mathbf{s}}^{\mathrm{TX}}(t)}{dt^2} = \mathbf{I}_{\mathbf{R}}(t) + j\,\mathbf{Q}_{\mathbf{R}}(t) \tag{3.17}$$

At this stage, a nonlinear analysis of the receiver front-end in the presence of the incident field may be again carried out by envelope-oriented harmonic balance [9]. The receiver excitations consist of a local oscillator of angular frequency ω_{LO} and of a set of modulated sinusoidal current sources of carrier frequency ω_{RF} and modulation laws expressed by (3.17), connected in parallel to the linear subnetwork ports. In the multitone harmonic balance analysis associated with each envelope sampling instant, the spectral lines are located at the IM products of ω_{RF}, ω_{LO}. The envelope-oriented analysis then provides the complex envelopes of all signals supported by the receiver, including the IF output voltage.

REFERENCES

[1] N. B. Carvalho, J. C. Pedro, W. Jang, M. B. Steer, "Nonlinear RF circuits and systems simulation when driven by several modulated signals", *IEEE Trans. Microwave Theory and Techniques,* Vol. 54, pp. 572-579, February 2006.

[2] M. Hata, "Empirical formula for propagation loss in land mobile radio services," *IEEE Transactions on Vehicular Technology*, Vol. 29, pp. 317-325, September 1981.

[3] F. X. Estagerie, A. Bennadji, T. Reveyrand, S. Mons, R. Quere, L. Constancias, P. Le Helleye, "Implementation of a Behavioral Model of SSPAs taking into account mismatches for efficient System Simulation of Modern AESA", *2007 Asia-Pacific Microwave Conference*, Bangkok, pp. 1 – 4, December 2007.

[4] C. Waldschmidt, S. Schultieis, W. Wiesbeck, "Complete RF System Model for Analysis Of Compact MIMO Arrays", *IEEE Trans. Vehicular Tech.,* Vol. 53, no.3, pp. 579-586, May 2004.

[5] J. W. Wallace, M. A. Jensen, "Mutual coupling in MIMO wireless systems: a rigorous network theory analysis," *IEEE Trans. Wireless Commun.,* Vol. 3, no. 4, pp. 1317-1326, July 2004.

[6] M. L. Morris, M. A. Jensen, “Impact of receive amplifier signal coupling on MIMO system performance”, *IEEE Trans. Vehicular Tech.,* Vol. 55, no.3, pp. 1678 - 1683, September 2005.

[7] C. Kuhnert, S. Schulteis, A. Hangauer, W. Wiesbeck, “Impact of receiver inter-chain coupling on BER performance of space-time coded MIMO systems”, *2006 Vehicular Technology Conference,* pp. 2752 – 2756, Melbourne 2006.

[8] V. Rizzoli, A. Costanzo, D. Masotti, P. Spadoni, "Prediction of the End-to-End Performance of a Microwave/RF Link by means of Nonlinear/Electromagnetic Co-Simulation”, *IEEE Transactions on Microwave Theory Techniques*, Vol. 54, pp. 1149-1160, Dec. 2006.

[9] V. Rizzoli, A. Neri, F. Mastri, and A. Lipparini, "A Krylov-subspace technique for the simulation of RF/microwave subsystems driven by digitally modulated carriers", *Int. Journal RF Microwave Computer-Aided Eng.*, Vol. 9, pp. 490-505, November 1999.

[10] P. Daniele, V. Degli Esposti, G. Falciasecca, G. Riva, “Field prediction tools for wireless communications in outdoor and indoor environments” *Proc. IEEE MTT-Symp. European Topical Congress "Technologies for Wireless Applications",* Turin, Italy, November 1994.

[11] C. A. Balanis, Advanced Engineering Electromagnetics. New York: Wiley, 1989.

MIMO LINK NONLINEAR / EM CO-SIMULATION

Motivation

Primary motivation for the introduction of multiple-transmit and multiple-receive wireless communication systems was the possibility to exploit spatial diversity strategies – as already demonstrated by Winters [1] in the 1980's. With the hypothesis to transmit the same signal reply on D different incorrelated channels, the overall probability to have the same fading effect among all the paths is remarkably reduced: intuitively if p is the outage probability for a single channel, the correspondent probability for all the D incorrelated channels is $p_{eq} = p^D$, much lower than p. Another crucial advantage is the potential of MIMO systems to reach remarkable capacity gains [1] – [3] in rich multipath environments.

While coding and signal processing are key elements to successful implementation of a MIMO system, propagation channel and antenna plus frontend design are the major parameters that ultimately impact on system performances. As a result, considerable research has been recently devoted to these areas. For example while a spatial diversity is conventionally obtained by the use of multiple antenna system with an array step of 10λ or more, many authors have stressed the importance of the identification of optimum small antenna spacing case by case [4], [5] capable of compensating the selective fading with larger values of $\mathbf{H}(\omega)$. In these cases mutual couplings between the radiating elements are found responsible for such favourable effects.

The proposed CAD procedure is aimed to overcome many ineffectivenesses among the different study approaches on wireless radio systems, focusing on a variety of physical side effects that significantly influence the system performances. Its functional validity makes it a serious candidate for a future state-of-the-art general reference scheme.

Commercial EM simulation tools provide for an accurate description of all the radiating elements in terms of circuit matrix including mutual coupling effects. A careful computation of the non-ideal radio channel is developed by a RT technique: the reciprocity theorem allows to extrapolate a very careful equivalent impressed source at the receiver side combining interactions between signal, radio channel and antenna radiation pattern and converging into a unique exhaustive propagation scenario. The objective is to reduce the all-embracing analysis into a circuit-level simulation implemented by HB technique.

It is important to stress that not only a link analysis is provided here but the extention to a somehow electromagnetic compatibility problem is immediate: any kind of external interferer

is inexpensively included in the analysis through an appropriate addictional equivalent source generator.

Proposed scenario: generalities

A general reference end-to-end block is proposed in Fig. 4-1: from left to right, the first block is the bit generator, whose output is a random bit streams at a fixed bit rate. After that, the bit sequence is transformed into a symbol sequence by a mapper, which is different according to the modulation law used. The digital signal is now ready be transformed into an analog signal, thanks to a modulator. Average power, pulse shaping filter type and center frequency of the output envelope signal have to be specified in this block. The modulator output is the IF complex envelope waveform.

In the receiver chain, the dual components are used in order to transform the receiver IF output to its corresponding bit streams. Successively, a demodulator convert the signal in a symbol sequence, a detector takes the demodulator output and converts it in a bit sequence, and, in the end, a bit error rate meter tests whether the received bit streams corresponds to the transmitted one.

System-level analysis is implemented in AWR VSS system simulator.

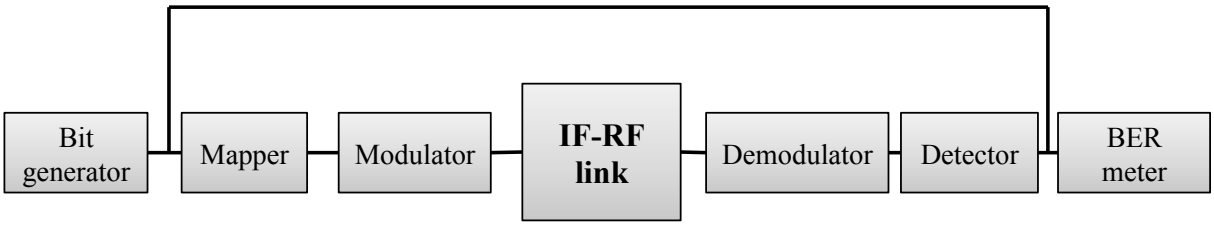

Fig. 4-1. Microwave link in terms of its functional blocks

Here a 2×2 MIMO link designed for WLAN application at 2,437 GHz is considered. The transmitter and receiver side are presented with regard to their topology and performances.

Neural network approach for BER computation

BER computation introduces an additional problem, since it is well known that a very large number of symbols of the order of several hundred thousands need be considered in

order to obtain meaningful results [6]. This would lead to unrealistic CPU times even with advanced nonlinear simulation algorithms based on model-order reduction techniques: for example the proposed all-embracing link analysis for the scenario under test with a flowing signal of only 2,048 bit on 16-QAM modulation format would require 36,000 s on a DELL Latitude C840 PC.

In order to overcome this difficulty we resort to ANN modeling. The model features that we are looking for are high accuracy and low identification time, as well as the ability to achieve a reliable training making use of a small-size training set. On the other hand, for our present purposes generality is not an issue. In other words we do not seek a link model allowing the response to be computed under arbitrary input drive conditions, but rather an ANN that can extend a short sequence of output samples generated by simulation for a specific modulation format and input drive level. In addition, we are not looking for a cascadable system model, but only for a model of the system operating between known terminations. Referring to [6], we thus use only the input and output voltages and their time derivatives as state variables. In a discrete-time environment this can be simply done by resorting to a recursive ANN of the kind discussed in [7], [8]. Specifically, at a given envelope sampling instant t_n, we feed to the network input the input signal envelope samples computed at t_n and the input and output samples computed at a finite number m of preceding instants, namely, $t_{n-1}, t_{n-2}, \ldots, t_{n-m}$. The ANN thus has $2(2m+1)$ inputs and 2 outputs, and its I/O maps may be cast in the form:

$$I_{out}(t_n) = F_I\left[I_{in}(t_n), Q_{in}(t_n), I_{in}(t_{n-1}), Q_{in}(t_{n-1}), \ldots, I_{in}(t_{n-m}), Q_{in}(t_{n-m}), I_{out}(t_{n-1}), Q_{out}(t_{n-1}), \ldots \right.$$
$$\left. \ldots I_{out}(t_{n-m}), Q_{out}(t_{n-m})\right] \tag{4.1}$$

$$Q_{out}(t_n) = F_Q\left[I_{in}(t_n), Q_{in}(t_n), I_{in}(t_{n-1}), Q_{in}(t_{n-1}), \ldots, I_{in}(t_{n-m}), Q_{in}(t_{n-m}), I_{out}(t_{n-1}), Q_{out}(t_{n-1}), \ldots \right.$$
$$\left. \ldots I_{out}(t_{n-m}), Q_{out}(t_{n-m})\right] \tag{4.2}$$

where $I_{in}(t) + jQ_{in}(t)$ and $I_{out}(t) + jQ_{out}(t)$ are the complex envelopes of the input and output IF signals, respectively. The nonlinear functions F_I, F_Q are implemented by a standard feedforward three-layer perceptron [7], and the total number of state variables is defined by the integer m. In principle, the optimum value of m should be determined by the embedding process [6] whose application to a large system would require long CPU times. However the

very stringent restriction imposed on the input excitation (fixed modulation and power) justifies the heuristic conjecture that only a small number of internal states be excited and consequently a small number of state variables be needed. Thus only $m = 1$, $m = 2$ and $m = 3$ have been tested for several circuits and it has been found that $m = 1$ and a set of several hundred samples appear to be sufficient to train an ANN that is able to accurately determine the link response to the specific selected excitation at all subsequent instants. A number of hidden-layer neurons of the order of 20 to 30 are normally sufficient to achieve excellent results. Training is then performed by the Levenberg-Marquardt algorithm coupled with a stop criterion based on cross-validation in order to minimize the generalization error [8].

Antenna system

A crucial feature is that all the non-idealities in the antenna systems on both transmitting and receiving side are remitted to a full-wave EM analysis. In this case CST Microwave Studio tool is exploited.

CST Microwave studio

CST (Computer Simulation Technology) Microwave Studio can be classified as time-domain 3D EM simulator based on *Finite Integration Technique* (FIT).
FIT is a integral-form variant of the more familiar FDTD (*finite-difference time-domain*) computational electromagnetic modeling, firstly traceable to Yee [9]: the spatial structure is divided into an hexahedral mesh and the Maxwell equations in the integral form are therefore discretized into equation in cartesian coordinates and solved by numerical derivatives. As depicted in Fig. 4-2, discrete elements are cuboids in 3D case. Understandably, the electromagnetic properties and the size of the meshing elements can all be different.

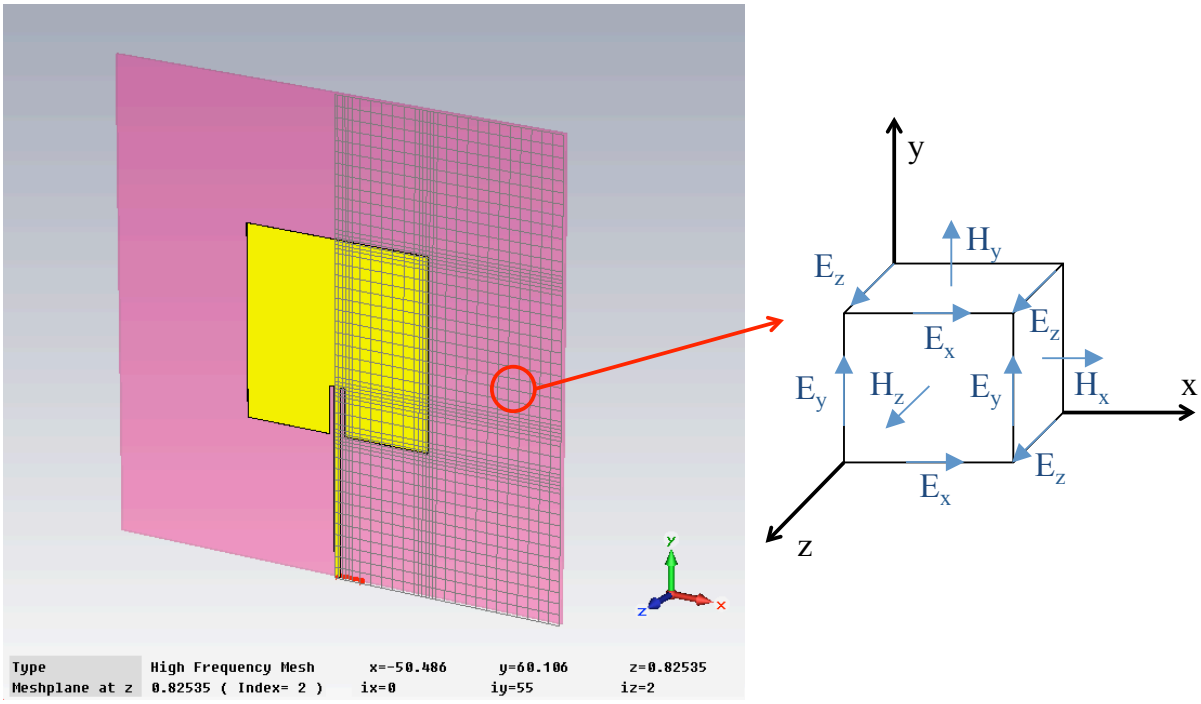

Fig. 4-2. Mesh view from CST Studio and three-dimensional Yee cell showing the staggered positions of the field component samples.

The analysis starts from a simple time impulse applied in a customized waveguide port and Maxwell's integral equations are then replaced by matrix equations that can be solved either by matrix inversion or by iterative techniques. Dispersive parameters such as **S**-matrix elements are carried out through a FFT over the bandwidth, by calculating the ratio between output and input signal at all ports. The integration of *perfect boundary approximation* (PBA) allows the structure to be sampled rather coarsely, thus reducing memory requirements and computational effort. Typical output functions for such analysis are current density **J**, **E-H** fields over the metalizations, **S-Y-Z** matrix and radiation function in case of antennas.

The cell size is basically determined as a function of dispersion caused by different propagation velocities at different frequencies through a generic heterogeneous material. Over each FIT cell dimension the electromegnetic field is supposed not to change significantly, so the grid size should ba a fraction of the wavelenght for the highest significant frequency content f_u [10] of the excitation impulse. An empyrical criterion proves a good cell size to be $\lambda_u/10$ [11] in the material medium.

Once the cell size is estabilished, the time step can be determined straightforwardly: the guideline is the well-known *Courant stability criterion* expressed by

$$\Delta t \leq \frac{\sqrt{\mu\varepsilon}}{\sqrt{\left(\frac{1}{\Delta x}\right)^2 + \left(\frac{1}{\Delta y}\right)^2 + \left(\frac{1}{\Delta z}\right)^2}} \tag{4.3}$$

(4.3) formalizes the idea that any point on the wave must not travel more than one cell because during one time step the FIT algorithm can propagate the wave only from one cell to its nearest neighbors, and any slightly larger time step would cause numerical instability. In (4.3) Δx, Δy and Δz describe the cell size and $(\mu\varepsilon)^{-1/2}$ is the speed of light.

Antenna topology

For the simulated scenario the antenna array at both sides is constituted by a two half-wave dipoles (Fig. 4-3) printed on separate substrates and analyzed by CST Studio for several element spacing. The substrate is Taconic (ε_r = 6.15, tanδ = 0.0028) with a thickness of 0.635 mm. The metalization is on Copper with thickness of 0.035 mm. Fig. 4-3 show the simulated array.

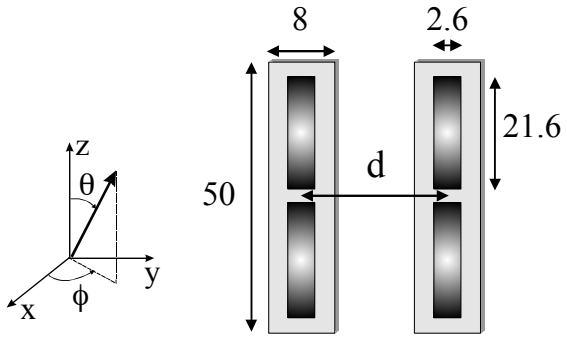

Fig. 4-3. Printed dipole array – dimensions in mm

The results in terms of scattering matrix can be observed in Fig. 4-4:

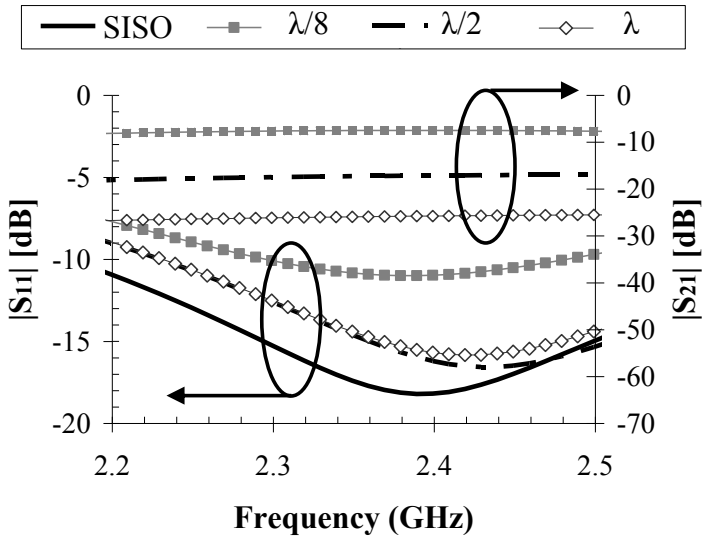

Fig. 4-4. Scattering parameters $|\mathbf{S}_{11}|$ and $|\mathbf{S}_{21}|$ of the two-port transmitting antenna for different dipoles spacing (d) and for the standalone dipole (SISO).

Intuitively the best result for $|\mathbf{S}_{11}|$ is for the standalone antenna (SISO case) while the coupling effect between the two elements has repercussions on lower values of the reflection coefficient at each antenna terminal. That side effect is reduced with a progressive increase of the array step.

At the same time a parasitic power transfer due to the proximity of the two antenna elements is highlighted by considerable values of $|\mathbf{S}_{21}|$: as far as the distance between antennas increases, the former value tend to become negligible as well.

In terms of radiation pattern the effect of parasitic coupling is shown in Fig. 4-5:

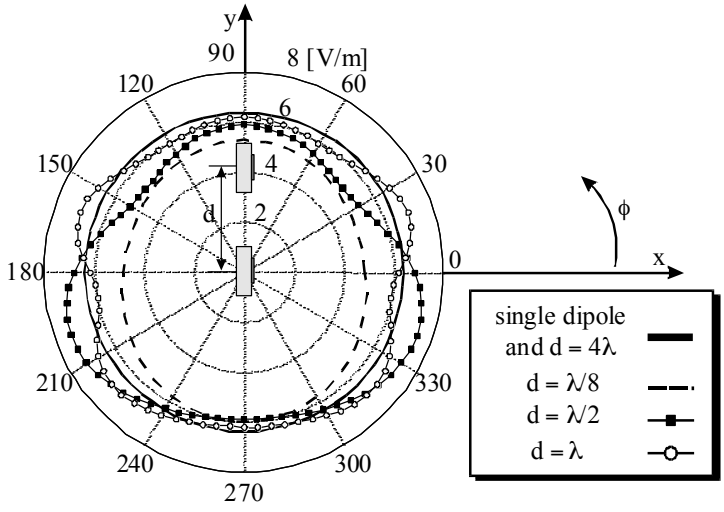

Fig. 4-5. H-plane radiation pattern of a standalone dipole and of one dipole in the presence of the other for different inter-element spacing.

A pattern modification due to the parasitic dipole in proximity of the fed one is clearly visible and – as stated before – less pronounced with large antenna spacing.
In conclusion theoretical approaches on MIMO analysis based on the assumption of isolated antennas do not represent a valid description of real-world compact systems.

Transmitter front-end: topology and details

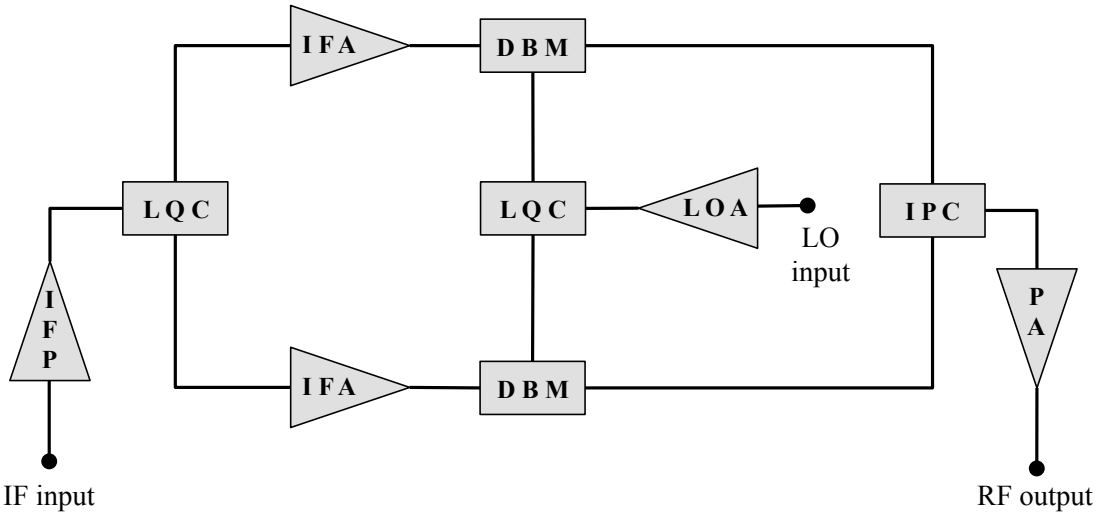

IFP = IF preamplifier
IFA = IF amplifier
IPC = In-phase power combiner
DBM = Doubly-balanced mixer
LQC = Lumped quadrature coupler
LOA = LO amplifier
PA = Power amplifier

Fig. 4-6. Transmitter front-end – functional blocks only.

For any single transmitter a single-conversion architecture is considered here including a doubly-balanced quadrature mixer arranged in a lower-sideband-suppressing configuration, amplifiers, passive coupling circuits, and several linear parasitics. The block scheme in Fig. 4-6 shows the transmitter in terms of its functional blocks. After an IF preamplifier, a lumped quadrature coupler splits the signals in two different paths. Another amplifier, for each way, precedes the doubly-balanced mixer, whose task is to up-convert the IF signal to RF. In order to fulfil its function, the mixer makes use of a local oscillator (LO) signal at high power. Finally, the two signals are phased and combined by an in-phase power combiner, then the resulting RF signal is amplified before flowing out at the transmitter output port.

For the present case the number of internal nodes is 2,370 and 196 device ports are present. The input 400 MHz IF carrier is phase- and amplitude- modulated according to a 16-QAM format. The LO signal is sinusoidal with -10 dBm available power at 2,037 MHz. 4

LO harmonics plus one lower and upper sideband per LO harmonic are taken into account. The total IF input power is -27dBm.

The symbol-rate of the signal propagating through the channel is 0.512 Msymb/s, with a consequent bit rate of 1.28 Mbit/s and an oversampling of two sample-per-bit.

The overall in-band transducer gain is found to be 42 dB in SISO case, while is considereably reduced – down to 36 dB – in MIMO Configuration.

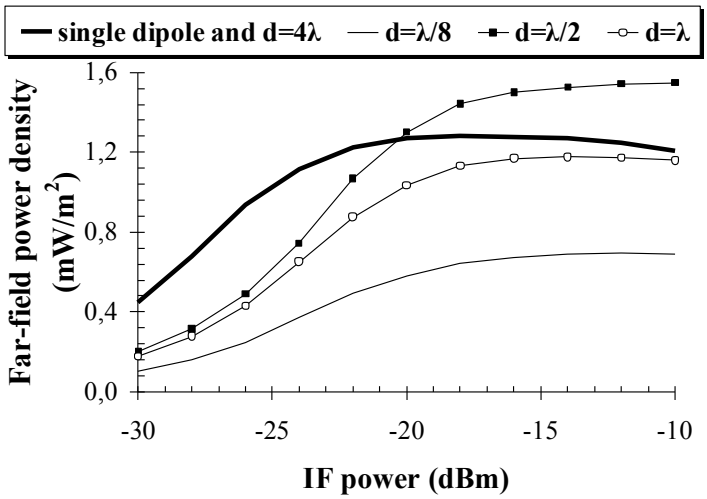

Fig. 4-7. Transmitter gain compression curve for different dipoles spacing.

An accurate characterization of the phenomena is required: let us consider Fig. 4-7 where the far-field radiated power density ($\mathbf{E_T} \bullet \mathbf{E_T}^*/2\eta$) evaluated by (3.6) is plotted against IF input power as a function of dipole spacing. For the sake of comparison, the same analysis is repeated for an identical standalone transmitter. The transmitter gain compression curve is found to be strongly influenced by the presence of neighbouring array elements. As previously mentioned frequency-dependent antenna interactions are widely recognized to have a primary influence on MIMO channel capacity [4], [5]. Fig. 4-7 shows that they also play an essential role in determining the linear and nonlinear transmitter performance. Indeed, such performance may be enhanced or degraded with respect to the SISO case depending on antenna spacing, thus exalting the importance of the proposed CAD approach.

Finally it should be added that in order to generate such results the set of N^{TX} transmitters is described as a unique nonlinear circuit loaded by a multiport network (the antenna array) with a non-diagonal admittance or scattering matrix, and is simulated by

nonlinear analysis techniques for large circuits [13]. This represents another distinctive feature of our CAD procedure as compared to previous work [4], [12].

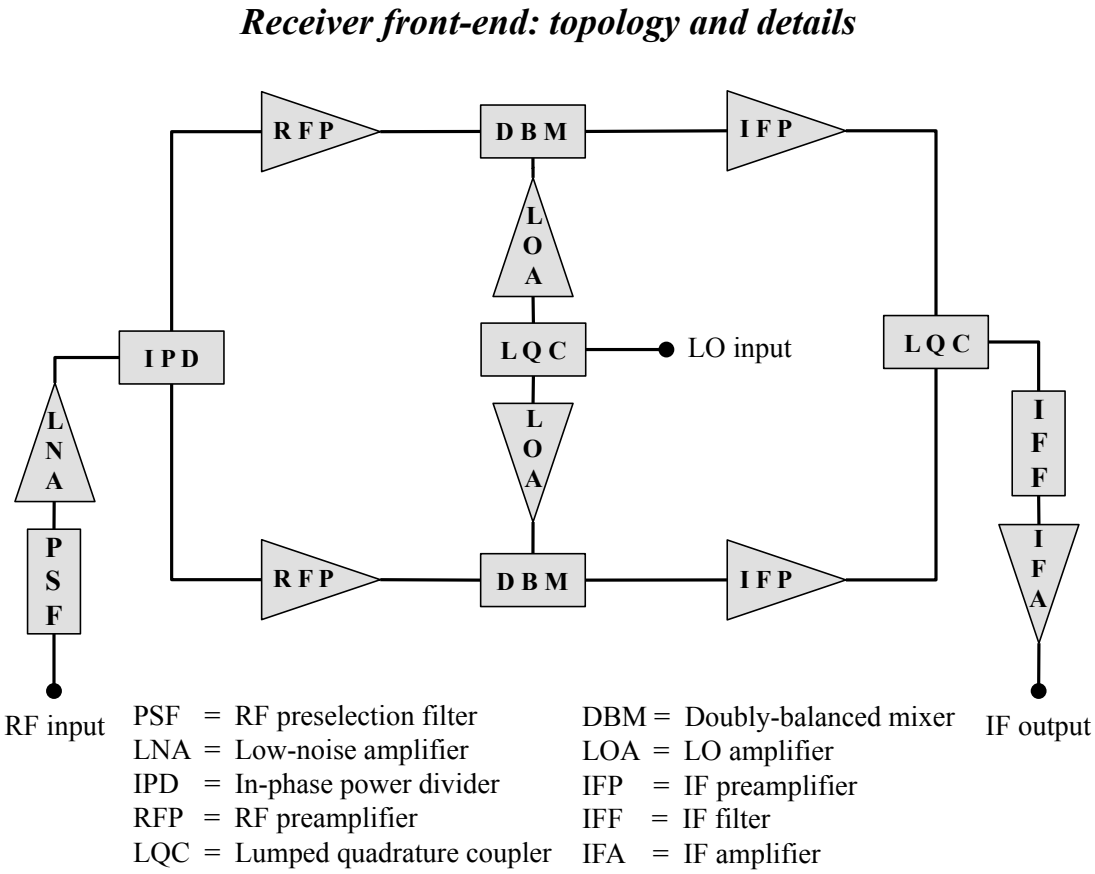

Fig. 4-8. Receiver front-end – functional blocks only.

The image-rejection receiver (Fig. 4-8) presents an architecture similar to that of the transmitter. The RF signal flows out from the antenna array, it is filtered and then amplified by a low-noise amplifier (LNA). After that, an in-phase power divider splits the signal in two different paths, and, before being down converted by the doubly-balanced mixer, each signal is again amplified. The mixer makes use of a 5 dBm local oscillator signal. A lumped quadrature coupler then recombines the two paths into the same signal, which is now at 90 MHz intermediate frequency. In the end, the last steps consists in filtering and amplifying the IF output signal.

Similarly to the transmitter, the receiver has a large number of nonlinear components: 416 device ports and 2,490 nodes confirm the high complexity of this nonlinear system.

Propagation scenario

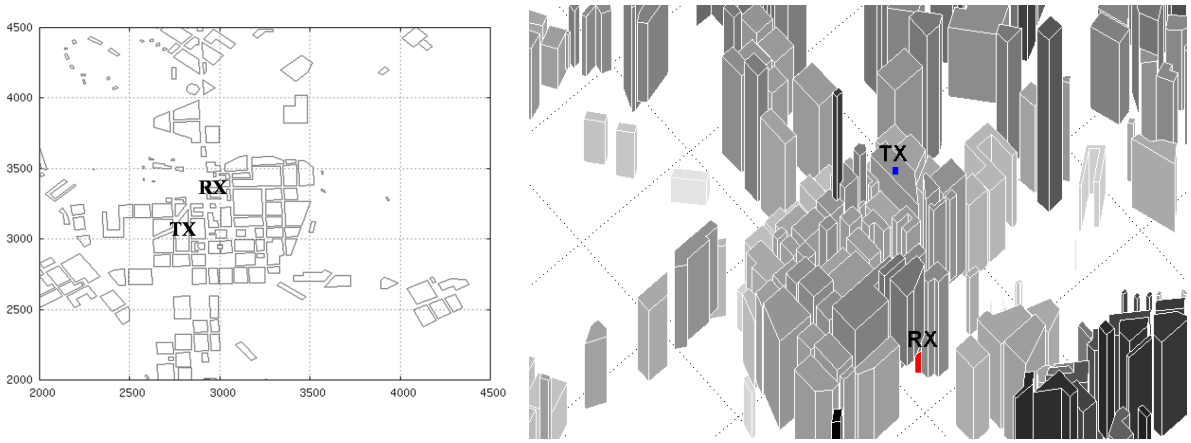

Fig. 4-9. Propagation scenario – 2D and 3D view.

The link under test is represented in Fig. 4-9 with regard to the radio channel, in 2D and 3D view. The scenario is a typical urban environment (Helsinki city centre) with transmitter and receiver in Non-Line-Of-Sight (NLOS) configuration. In the present case the total number of received paths to be taken into account is found to be about 3,000.

Link analysis results

What follows here are the most relevant results of the direct application of the proposed analysis approach for the link under test. The various relevant physical effects from a performance point of view are investigated through the different converging analysis techniques and then presented in the section.

The channel scenario needs more than 3,000 propagation rays and the transmitting antenna elements are kept at a fixed distance of 6.16 cm, corresponding to half a wavelenght. A sequence of nonlinear link analyses is carried out by varying the receiving antenna element spacing. The front-ends are excited by a sinusoidal IF signal. Figs. 4-10, 4-11 compare the magnitudes of the entries of the channel transfer matrix $\mathbf{H}(\omega_{\mathrm{RF}})$ for antenna spacing of $3\lambda/8$ and $\lambda/8$ respectively:

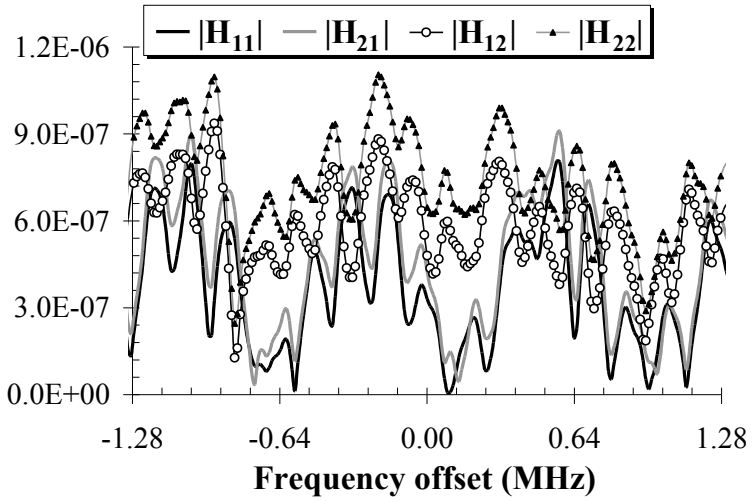

Fig. 4-10. Channel transfer matrix entries for $3\lambda/8$ dipoles spacing.

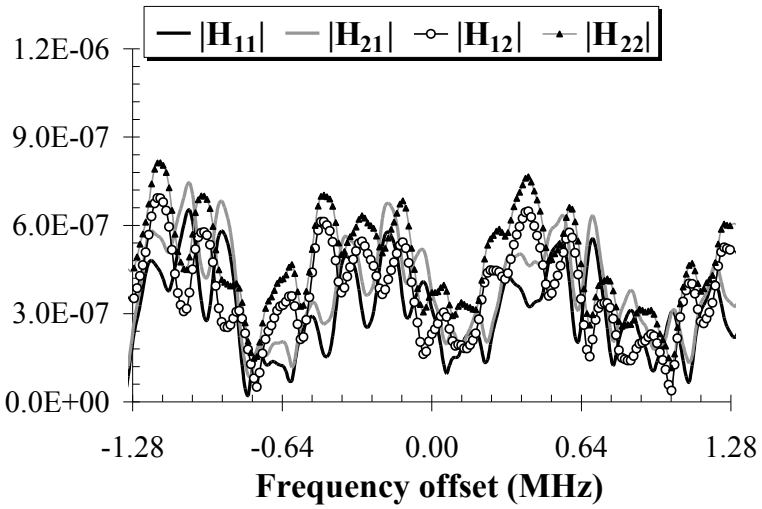

Fig. 4-11. Channel transfer matrix entries for $\lambda/8$ dipoles spacing.

The first subscript refers to the receiver dipole, the second one to the transmitter: the two plots clearly demonstrates that the channel selective fading may be effectively compensated by a suitable antenna spacing, since larger values of the $\mathbf{H}(\omega)$ entries automatically result in channel capacity improvement [4]. The next step is to optimize the antenna spacing for the given channel scenario and for a real-world digitally modulated signal. The selected modulation format is 16-QAM at a bit rate of 1.28 Mbit/s.

The system output signal is computed by combining in phase the output signals of the two receivers – according to the *equal-gain combining* technique. The adopted performance index is the BER in the presence of thermal noise described by a simple additive white Gaussian noise (AWGN) model. This is possible at the circuit level by the same technique introduced in [14] for the SISO case. Noise is modeled by an additional current source connected in parallel to J_s^r at each receiving antenna port. Fig. 4-12 shows the results obtained for a fixed SNR of 10 dB at the receiver input. Such results are based on a sequence of 1,600,000 samples generated by an artificial-neural-network link model trained by a sequence of 512 simulated samples. BER is estimated by direct I/O comparison [14]. For the scenario under consideration the optimum antenna spacing ($d \approx \lambda/4$) results in a BER reduction of about two orders of magnitude with respect to the SISO case.

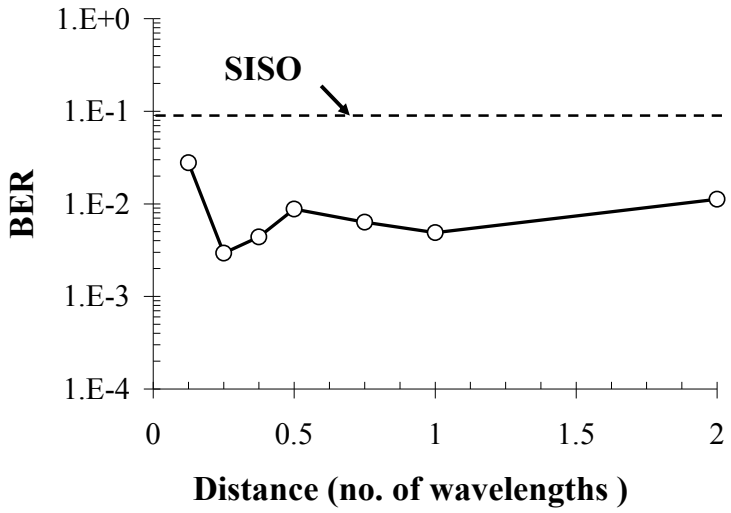

Fig. 4-12. Estimated BER for the MIMO link under test as a function of dipoles spacing

Other investigations on link performances can confirm the results above: what follows in Figs. 4-13 and 4-14 is a comparison of the output signal constellations of the MIMO link with optimal ($\lambda/4$) and non-optimal ($\lambda/8$) antenna spacing respectively.

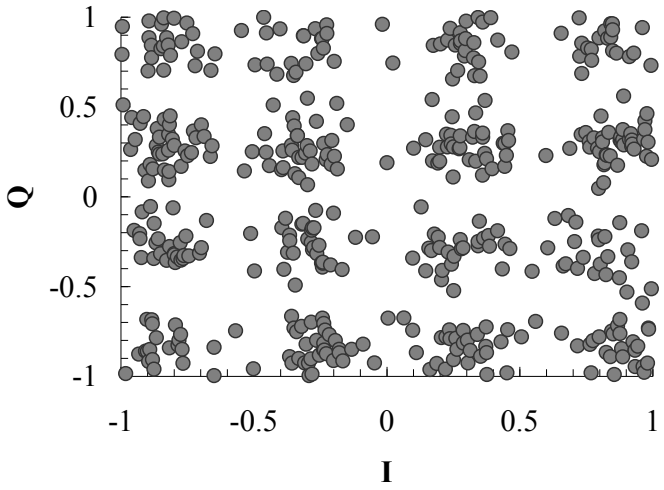

Fig. 4-13. Output signal constellation of the MIMO link under test with $\lambda/4$ antenna spacing

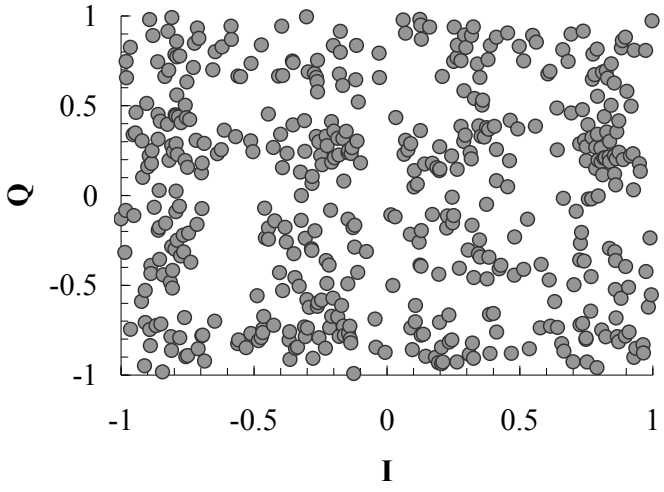

Fig. 4-14. Output signal constellation of the MIMO link under test with $\lambda/8$ antenna spacing

Up to now the only causes considered for signal corruption are noise and in-band linear distortion. Also nonlinear distortion deserve mention: it is found to be somewhat improved by the MIMO arrangement with respect to the corresponding SISO system (same circuits and channel), but the effect is not as dramatic as for BER. This is evident by comparison of Figs. 4-15, 4-16 and 4-17 where the input and output signal spectra are shown – in the absence of noise – for the MIMO system with optimal antenna spacing and for the corresponding SISO system, respectively. The adjacent-channel power ratio (ACPR) is reduced by about 4 dB in the MIMO case. Also, for a MIMO system nonlinear distortion is almost independent of antenna spacing. As an example, the output spectrum reported in last figure for a case of non-

optimal antenna spacing ($d \approx \lambda/8$) exhibits a distortion level quite similar to that observed before – the change in ACPR is less than 1 dB.

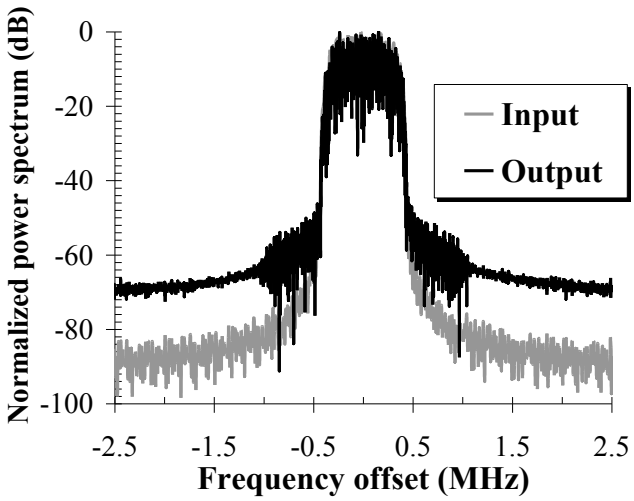

Fig. 4-15. Normalized power spectra of a MIMO link for optimal dipoles spacing.

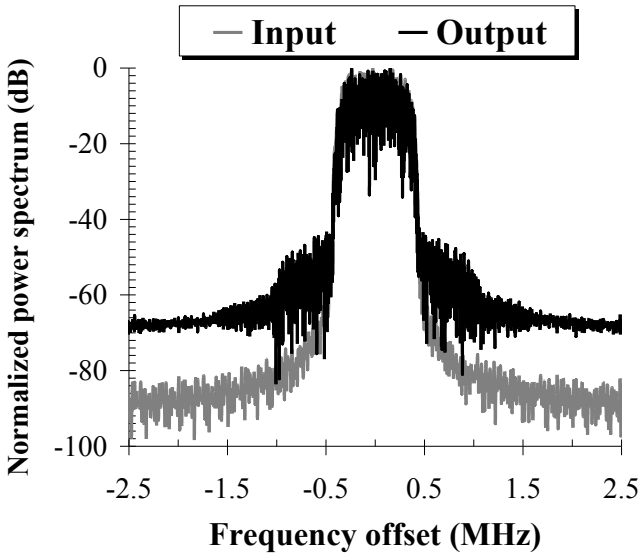

Fig. 4-16. Normalized power spectra of a SISO link for the same propagation scenario

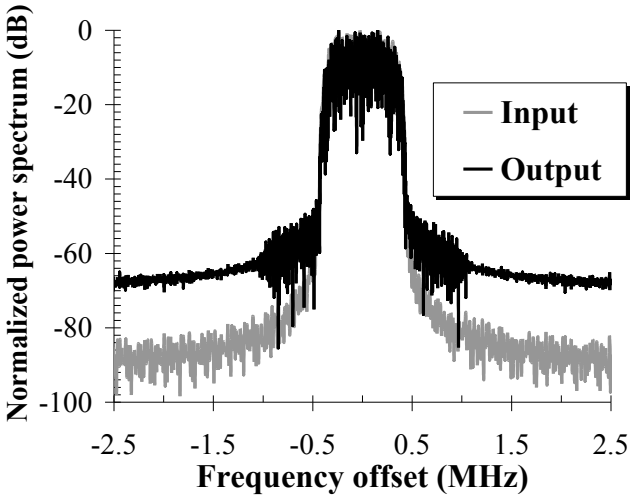

Fig. 4-17. Normalized power spectra of a MIMO link for non-optimal dipoles spacing.

A full nonlinear/electromagnetic multitone analysis of the 2×2 MIMO link requires about 100 minutes of CPU time on a 2.8 GHz PC. Within this budget, about 40% of the time is taken by the EM simulation of the transmitting and receiving antenna arrays, about 45% by the computation of the RT-based field prediction model, and the remaining 15% by the nonlinear analysis of the transmitter and receiver front ends.

Validation procedure

For validation purposes we here present a comparison of the MIMO link analysis results produced by our technique with those generated by time-domain analysis for multiport dispersive components making use of Spectre HDL [15].

Time-domain procedure: generalities

The counterpart is fundamentally based on a subprogram capable of computing the port currents (the component response) at a generic time instant starting from the knowledge of the time-dependent port voltages (the excitations) applied to its ports. The device (linear *N*-port network) is described exclusively through its frequency-domain scattering or admittance parameters, which may be generated by any frequency-domain analysis procedure, including layout-based EM simulation. This information is used in a preprocessing step to derive the ramp responses of the transfer functions between all couples of ports. The exciting voltages

are then approximated by piecewise linear functions, and the transient response is evaluated with high numerical efficiency.

The procedure can be formalized under the assumptions that

1) the time variable is uniformly discretized so that the response need only to be computed at a set of sampling instants

$$t_n = t_1 + (n-1)\tau \tag{4.4}$$

where n is an arbitrary integer

2) for $t \le t_1$ the circuit is in stationary (DC) regime, or equivalently the excitations satisfy the condition

$$V_j(t) = V_j(t_1) \qquad (t \le t_1, 1 \le j \le N) \tag{4.5}$$

The unit ramp function $r(t)$ of duration τ is defined as follows

$$r(t,\tau) = \begin{cases} 0 & if\ t \le 0 \\ \dfrac{t}{\tau} & if\ 0 \le t \le \tau \\ 1 & if\ t \ge \tau \end{cases} \tag{4.6}$$

and finally we define $R_{ij}(t,\tau)$ as the current entering the i-th port anytime $r(t,\tau)$ is applied as a voltage excitation at the j-th port and all the remaining ports are short-circuited.

Consequently any arbitrary voltage excitation $V(t)$ satisfying the condition (4.5) can be expressed at the sampling instants (4.4) by a piecewise approximation in the time interval $t_1 \le t \le t_n$

$$\begin{aligned} V(t) &\approx V(t_1) + r(t-t_1,\tau)\left[V(t_2) - V(t_1)\right] + r(t-t_2,\tau)\left[V(t_3) - V(t_2)\right] + \ldots = \\ &= V(t_1) + \sum_{p=2}^{n}\left[V(t_p) - V(t_{p-1})\right] r(t-t_p,\tau) \end{aligned} \tag{4.7}$$

For any real network $R_{ij}(t,\tau)$ must be causal – thus $R_{ij}(t,\tau) = 0$ for $t < 0$. At the i-th port, the network response to the excitation $V(t)$ will be a current of the form

$$I_{ij}(t) = Y_{ij}(0)V(t_1) + \sum_{p=2}^{n}\left[V(t_p) - V(t_{p-1})\right] R_{ij}(t - t_p, \tau) \tag{4.7}$$

where $Y_{ij}(0)$ is evaluated at DC. The *n*-th time-domain sample $I_{ij}(t)$ is then

$$I_{ij}(t_n) = Y_{ij}(0)V(t_1) + \sum_{p=2}^{n}\left[V(t_p) - V(t_{p-1})\right] R_{ij}(t_n - t_p, \tau) \tag{4.8}$$

In the general case, with a network excitation consisting of all the voltages $V_j(t)$ applied to the ports, the *i*-th current at the *n*-th sampling instant becomes

$$I_i(t_n) = \sum_{j=1}^{N} Y_{ij}(0)\, V_j(t_1) + \sum_{j=1}^{N}\sum_{p=2}^{n}\left[V_j(t_p) - V_j(t_{p-1})\right] R_{ij}(t_n - t_p, \tau) \tag{4.9}$$

The samples of $R_{ij}(t, \tau)$ are computed and stored by a preprocessing step based on FFT – omitted for brevity.

The complete procedure is implemented in an analog hardware-description language.

Link analysis validation

The frequency-domain channel model already presented in the previous sections as modeled through the convolution-like technique discussed above.

This procedure is really remanding in terms of CPU time since it basically relies upon a time-domain convolution. The other bottleneck is the slow (1.28 Mb/s) modulation of the 2,437 GHz RF carrier, which generates the need for an unreasonably large number of time-domain integration steps.

The unavoidable tradeoff between accuracy and CPU time is obtained by limiting the number of frequency-domain sampling points for the entries of the channel transfer matrix, and of time-domain sampling points in the integration process. Even so, the CPU time required to compute the results reported in figures below by time-domain analysis was about 22,000 times longer than by the CAD procedure discussed in the previous sections. The benchmark quantity used for comparison is the Norton equivalent current source defined by

(3.14). The analysis is limited to a 64-bit time slot. Fig. 4-18 provides a visual comparison of the time-domain waveforms of this current computed in the presence of digital modulation. More quantitative comparisons are provided in Figs. 4-19, 4-20, showing the in-phase and quadrature components of the complex envelope. In all cases the agreement may be considered very satisfactory, which provides a reliable validity check for our MHB analysis procedure.

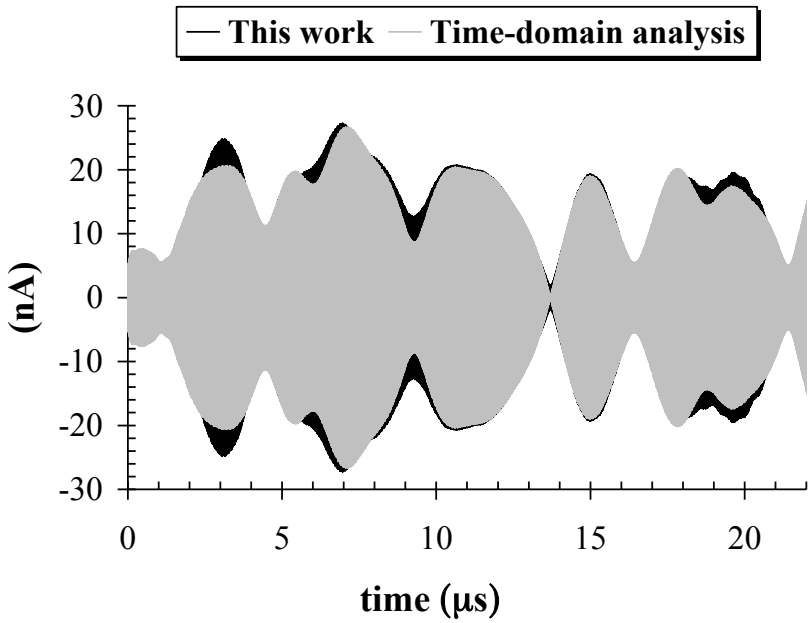

Fig. 4-18. Time-domain waveform of the modulated current source J_s^1 for the MIMO link with optimal dipoles spacing.

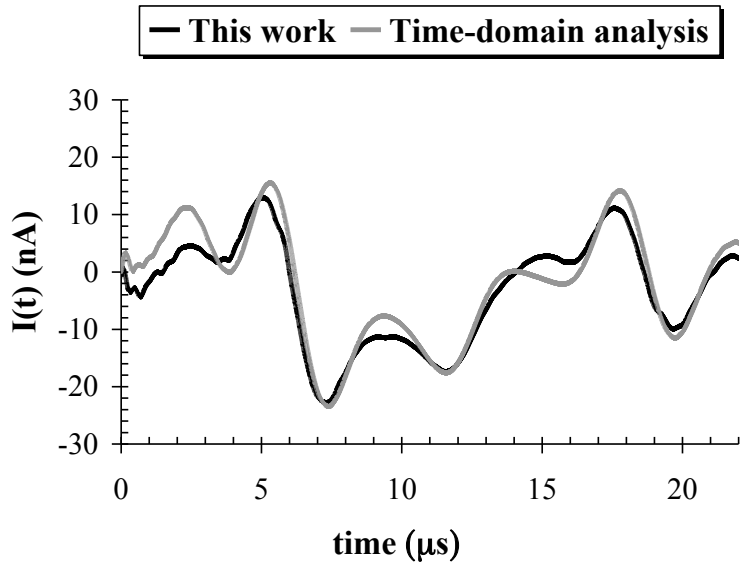

Fig. 4-19. In-phase component of the complex envelope for the modulated current source J_s^1.

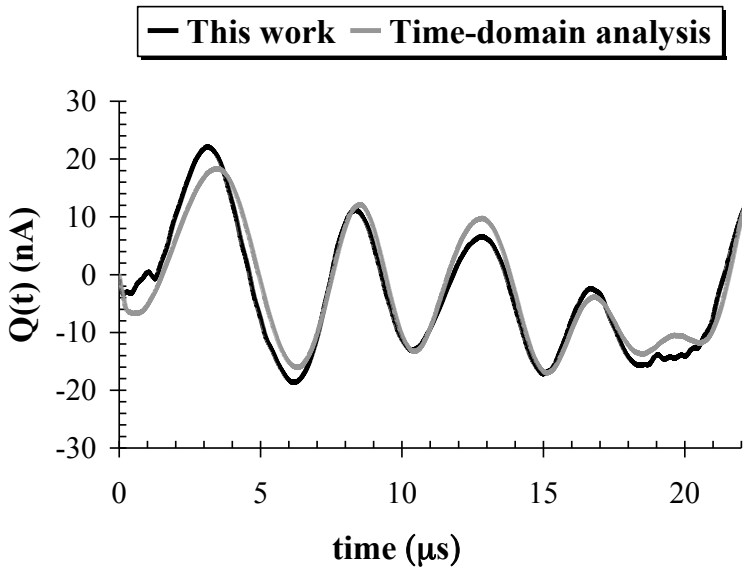

Fig. 4-20. Quadrature component of the complex envelope for the modulated current source J_s^1.

REFERENCES

[1] J. H. Winters, "On the capacity of radio communication systems with diversity in a Rayleigh fading environment," *IEEE J. Select. Areas Commun.*, vol. SAC-5, pp. 871–878, June 1987.

[2] G. J. Foschini, M. J. Gans, “On limits of wireless communications in a fading environment when using multiple antennas,” *Wireless Personal Commun.*, vol. 6, pp. 311–335, Mar. 1998.

[3] E. Telatar, “Capacity of multi-antenna Gaussian channels,” *Europ. Trans. Telecomm.*, vol. 10, no. 6, pp. 585–595, November – December 1999.

[4] J. W. Wallace, M. A. Jensen, “Mutual coupling in MIMO wireless systems: a rigorous network theory analysis,” *IEEE Trans. Wireless Commun.,* Vol. 3, no. 4, pp. 1317-1326, July 2004.

[5] K. Rosengreen, P.S. Kildal, “Radiation efficiency, correlation, diversity gain and capacity of a six-monopole antenna array for a MIMO system: theory, simulation and measurement in reverberation chamber”, *IEE Proc. Microwaves, Ant. and Prop.,* Vol. 152, pp. 7–16, February 2005.

[6] J. Liu, A. Bourdoux, J. Craninckx, B. Come, P. Wambacq, S. Donnay, and A. Barel, “Impact of front-end effects on the performance of downlink OFDM-MIMO transmissions”, *IEEE 2004 RAWCOM*, pp. 159-162.

[7] K. S. Narendra, K. Parthasarathy, “Identification and control of dynamical systems using neural networks”, *IEEE Trans. Neural Networks 1 (1)*, 1990, pp. 4-27.

[8] M. Kimura, R. Nakano, “Learning dynamical systems by recurrent neural networks from orbits”, *Neural Networks 11* (1998), pp. 1589-1599.

[9] K. S. Yee, “Numerical solution of initial boundary value problems in- volving Maxwell’s equations in isotropic media,” *IEEE Trans. Antennas Propagat.*, vol. AP-14, pp. 302–307, May 1966.

[10] W. L. Stutzman, G. A. Thiele, *Antenna Theory and Design*, New York: Wiley, 1997.

[11] D. G. Swanson, W. J. R. Hoefer, *Microwave Circuit Modeling Using Electromagnetic Field Simulation*. London: Artech House Publishers, 2003.

[12] C. Waldschmidt, S. Schultieis, W. Wiesbeck, "Complete RF System Model for Analysis Of Compact MIMO Arrays”, *IEEE Trans. Vehicular Tech.,* Vol. 53, no.3, pp. 579-586, May 2004.

[13] V. Rizzoli, A. Neri, F. Mastri, and A. Lipparini, "A Krylov-subspace technique for the simulation of RF/microwave subsystems driven by digitally modulated carriers", *Int. Journal RF Microwave Computer-Aided Eng.*, Vol. 9, pp. 490-505, November 1999.

[14] V. Rizzoli, A. Costanzo, D. Masotti, P. Spadoni, "Prediction of the End-to-End Performance of a Microwave/RF Link by means of Nonlinear/Electromagnetic Co-Simulation", *IEEE Transactions on Microwave Theory Techniques*, Vol. 54, pp. 1149-1160, Dec. 2006.

[15] V. Rizzoli, A. Costanzo, F. Mastri, A. Neri, "A general SPICE model for arbitrary linear dispersive multiport components described by frequency-domain data", 2003 *IEEE MTT-S International Microwave Symposium Digest*, Vol.1, pp. 9-12, June 2003.

ENERGY HARVESTING FROM COMMON RF SOURCES

The present chapter provides a second case study for the proposed approach, regarding the design, optimization and testing of various typologies of rectennas for power generation by common RF sources. The project was sponsorized by Eurotech S.p.A., based in Amaro (Udine – Italy).

Motivation

One of the most promising field of research is directed to provide sustainability and energetic autonomy to electronic devices and sensor networks, possibly avoiding bulky batteries. Such effort is also significantly animated by the state-of-the-art of modern micro/nano-electronics allowing for ultra-low power designs and therefore huge life expectancy. That purpose may be accomplished by extracting some of the required power from many sources already present in the environment, e.g. propagating radio waves, sunlight or vibrations. The pervasive presence of many and different RF sources such as mobile phones and/or WiFi hot spots in all humanized environments gives the opportunity to provide, at low distances, a sufficient amount of energy to be harvested, stored and used for supplying, as an example, a sensor node.

The powering of devices by incoming radio waves has been widely studied for passive or semi-passive radio identification systems (RFID) [1], [2]. In that case, tags are powered up by the query from the reader, conforming with a communication working principle based on backscattering modulation: inside the tag a fraction of the received signal is converted into DC voltage to bias the active devices, and the remaining part is conveyed into the demodulator. Different design configurations of charge-pump voltage multipliers have been proposed in the recent years [3], based on Schottky or CMOS technology. The received field is always known in terms of polarization, intensity and direction of arrival [4]

Nevertheless, the reported conversion efficiency is rather poor and that is due, according to the thesis motivation, to an ineffective system simulation approach. The exhaustive analysis method introduced in the previous chapters allows to exactly evaluate an arbitrary incoming field wave from a circuit standpoint by the application of EM theory. Then a full nonlinear analysis of the receiver including the antenna – described by EM simulation – is efficiently developed quantifying the rectified power. Any system optimization will be

eventually oriented to the maximization of the main figure of merit, the *conversion efficiency*, among all the frequency bands involved in the process.

Problem: generalities and solutions

One of the major challenges in RF energy scavenging is the need to deal with unknown sources characterized by an extremely variable link budget, especially for mobile phone systems. That is due to an unpredictable distance between base station and mobile terminal, and to a carrier frequency arbitrarly allocated within a specified range, according to multiple-access policies and traffic block probabilities.

The final target is to energy-scavenge from all the RF sources at the same time, for any polarization, angle of arrival and power intensity. The general scenario is depicted in Fig. 5-1:

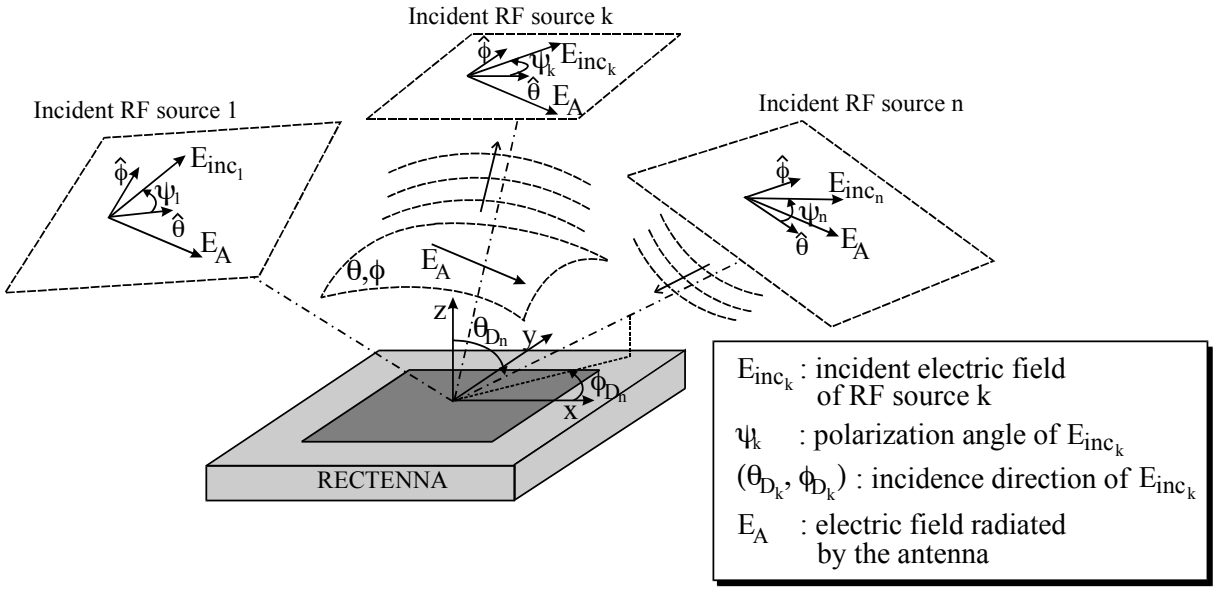

Fig. 5-1. General scenario of a rectenna in the presence of several radiating sources.

Several RF sources may exist and are described in terms of their respective radiated fields incident on the *rectenna* – antenna plus rectifying devices. As previously mentioned the respective frequency, direction of arrival and polarization may be arbitrary. Assuming that the RF sources are located in the far-field region of the harvester, a *k*-th incident field at the harvester location may be described as a uniform plane wave and thus by a constant complex vector $\mathbf{E}_{\text{inc}_k}$.

The proposed method as always exploits the reciprocity theorem to derive a rigorous equivalent circuit source for any possible RF excitation. As stated in the third chapter and exhaustively demonstrated in [5] for the straightforward application of such theory two EM configurations of the rectenna are considered, corresponding to the receiving and transmitting modes of operation respectively. Given the *k*-th RF incident field, (θ_{Dk}, ϕ_{Dk}) defining the direction of arrival, ω_k its angular frequency, η the free-space impedance and $Y_A(\omega)$ the frequency-dependent antenna admittance computed by EM analysis, the Norton equivalent source has again the form:

$$J_k(\omega_k) = j\frac{2}{\eta}\lambda_k Y_A(\omega_k)\,\mathbf{E}_{\mathrm{inc}_k} \bullet \mathbf{e}_A(\theta_{Dk},\phi_{Dk};\omega_k) \tag{5.1}$$

that immediately recalls (3.13) for one transmitter, one receiver and a single ray. In (5.1) the normalized quantity $\mathbf{e}_A$ is related to the radiated $\mathbf{E}_A(r,\theta,\phi;\omega)$ by the antenna in transmitting mode through the formula – under far field condition:

$$\mathbf{E}_A(r,\theta,\phi;\omega) = I\,\frac{e^{-j\beta r}}{r}\mathbf{e}_A(\theta,\phi;\omega) \tag{5.2}$$

In (5.2) we assume that the antenna is analyzed in transmitting mode through an arbitrary excitation by a current density *I* injected at the input port.

Thanks to the linearity of the excitation mechanism the contribution of all the ambient sources can take the form of a parallel of different Norton generators at the antenna terminals, as shown in Fig. 5-2:

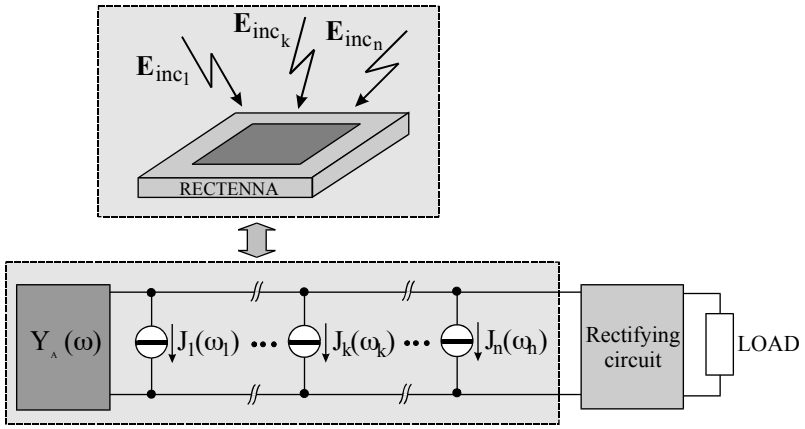

Fig. 5-2. Norton equivalent circuit of the rectenna under multiple excitations

The correct formulation of the system overall efficiency in terms of capability of DC-conversion starts from the well-known formulation of the equivalent available power at the input port, namely

$$P_{av} = \sum_k \frac{\left|J_k\left(\omega_k\right)\right|^2}{8\Re\left[Y_A\left(\omega_k\right)\right]} \tag{5.3}$$

comprehensive of all the RF sources involved.

The need for a rigorous computation of the rectified power the circuit implies the use of nonlinear analysis techniques such as HB: the whole nonlinear circuit will be studied under multitone excitation with a discrete spectrum with spectral lines located at tall the imtermodulation products of the exciting fundamental frequencies ω_k up to a prescribed order. The computational techniques have been already presented in the second chapter. It may be disclosed that in the rectenna single-frequency design four harmonics plus DC will be considered and IM products up to the fourth order for the multisource design.

Finally, once the DC power P_{out} is known, the EM conversion efficiency can be rigorously defined as

$$\eta_{\text{RF-DC}}^{\text{EM}} = \frac{P_{out}}{P_{av}} \tag{5.4}$$

This makes it possible to define simultaneous design goals on the conversion efficiency across the frequency bands of interest for the actual power levels pertaining to different

wireless standards. As in the MIMO case study, several crucial phenomena, such as power mismatch between antenna and receiver front end, polarization conflicts between incident electric fields and harvester antenna, and the simultaneous presence of different RF sources, are automatically included in all the evaluations. Obviously (5.4) constitutes the optimum figure of merit and the goal for any optimization process oriented to the minimization of impedance mismatches across the frequencies of interest, through a suitable matching network. The complete rectenna functional scheme is depicted in Fig. 5-3.

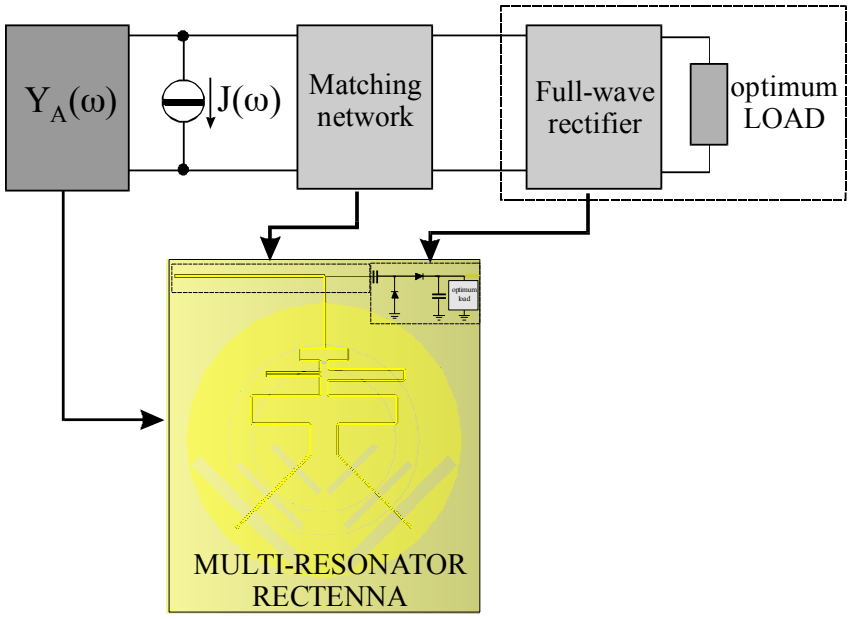

Fig. 5-3. Rectenna layout and rectifier topology

An important step of the design procedure is the selection of the rectifier topology, which is crucial for ultra-low power budgets. One degree of freedom is the number of stages. Our choice, in agreement with [6], is a single-stage full-wave peak-to-peak RF-DC power converter.

With regard to the choice of the nonlinear element, the low power intensity incoming from common RF standards drives towards the class of low-threshold devices such as Schottky diodes. The selection of the proper diode plays an essential role: major guidelines for a good conversion efficiency are the lowest possible zero-bias junction capacitance C_{j0}, and the highest saturation current I_s. The SPICE equivalent circuit parameters of several diodes available from the market are shown in Table 1.

	Skyworks SMS7630	Skyworks SMS7621	Skyworks SMS3922	Skyworks SMS1546	Macom MA4E2054	Agilent HSMS2852	Agilent HSMS8101
I_s [μA]	**5**	0.04	0.03	0.3	0.03	3	0.046
C_{j0} [pF]	**0.14**	0.1	0.7	0.38	0.13	0.18	0.18
V_{th} [V]	**0.34**	0.51	0.595	0.51	0.4	0.35	0.5
N	**1.05**	1.05	1.08	1.04	1.05	1.06	1.09
R_s [Ω]	**20**	12	9	4	11	25	6
I_{bv} [μA]	**100**	10	10	10	10	300	100
V_{bv} [V]	**2**	3	20	3	5	3.8	7.3
$\eta_{RF\_DC}^{EM}$	**13 %**	7.68 %	3.7 %	11.5 %	7.4 %	10.54 %	8.25 %

Table 1. Diodes SPICE parameters comparison

During the selection process a preliminar investigation was necessary for the conversion efficiency delivered by each of the previous components – as reported in the last row of Table 1. Without any optimization process a simple 1.38 dBm sinusoidal tone feeds a single-stage full-wave rectifier with 50-Ohm input and load impedances. The final choice was for Skyworks SMS7630 diode. The SOT-23 package equivalent circuit was conveniently inserted into the schematic during all the optimization process and nonlinear analysis.
The optimum load represents a further optimization goal.

Harvesting from known sources

A rectenna optimization can be considered under two different points of view: 1) the RF power to be rectified comes from one known source, whose location and frequency of operation are defined; 2) several RF sources radiating in different frequency bands and ubiquitously distribuited in the ambient. In that case a secondary subdivision is possible for single- or multi-frequency operations.

The following radiating element design answers to the first type of scavenging operation: a high efficient harvester operating in the Universal Mobile Telecommunication System (UMTS) / Global System for Mobile Communication (GSM) 1800 band. The photograph and dimensions of the entire system layout are shown in Fig. 5-4.

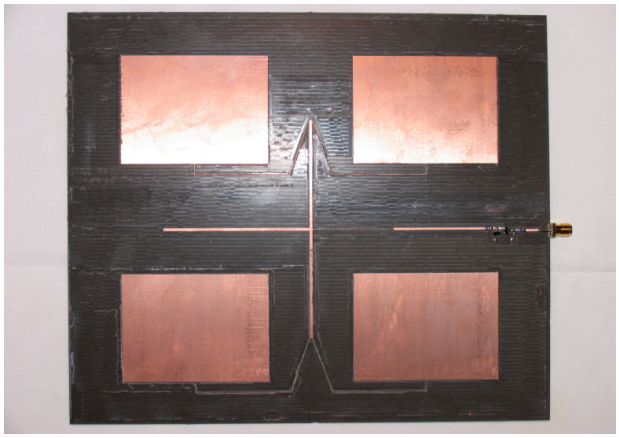

Fig. 5-4. harvester prototype based on a 2×2 linearly polarised patch antenna array - overall dimensions: 22×19 cm^2.

A high gain (≈ 13dB) linearly polarized four-patch array on a Rogers Duroid 5870 substrate has been designed together with the rectifier matching network and the load, having in mind the typical RF power levels available during a single phone call.

The computed conversion efficiency of the subsystem at 1.95 GHz before and after optimization is shown in Fig. 5-5, as well as a view of its frequency dependence in Fig. 5-6 due to the dispersive behaviour of the antenna itself.

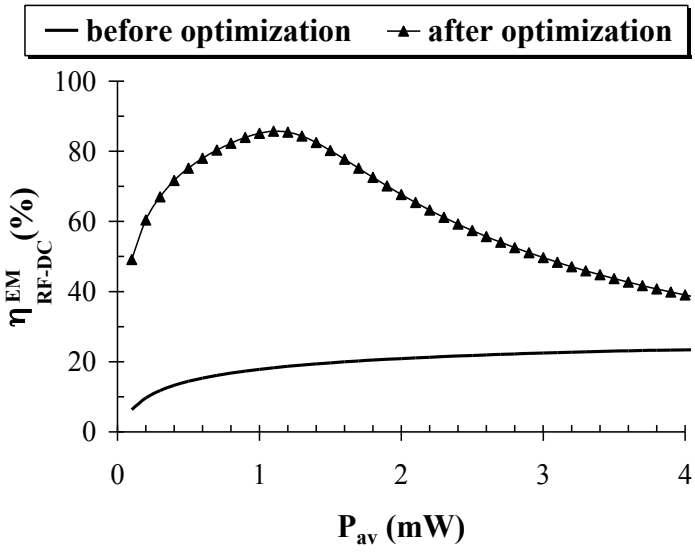

Fig. 5-5. Conversion efficiency of the 2×2 patch harvester at 1.95 GHz – before and after the optimization process.

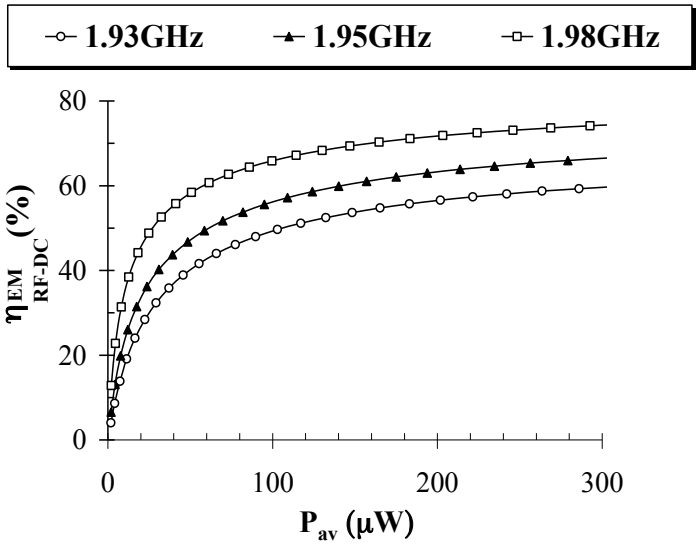

Fig. 5-6. Conversion efficiency of the 2×2 patch harvester among three different frequencies inside UMTS uplink band.

An intensive measurement campaign was developed by positioning the harvester in front of a cell phone and the open-circuit voltage at the load terminals is recorded during a transmission burst (which lasts approximately 500 μs) at several distances from the source.

The envelope-oriented HB technique – introduced in the second chapter – allows an accurate comparison between measurements and theory under those operating conditions: an excellent agreement is observed down to 50 cm distance between the cell phone and the tag (Fig. 5-7).

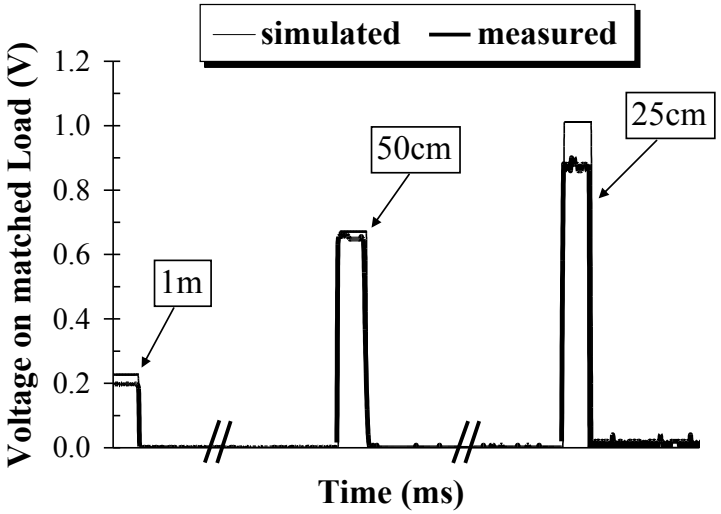

Fig. 5-7. Predicted and measured DC output voltage of the 2×2 patch harvester produced by a cell phone transmitting from different distances

At lower distances the predicted DC voltage begins to overestimate the measurements, probably due to electric field reflections between source and tag and the failure of the uniform plane wave approximation used at short distances. Further improvements in the general theory are under progress.

Harvesting from multiple unknown sources

Single-frequency operation

A second more sophisticated design has been conceived for exploiting - possibly - multiple sources operating in the GSM 1800 band. A coplanar slot antenna with a gain of about 2 dB has been used: the design was inspired from [7] and circular polarization is guaranteed by the T-shaped metallic strip from the ground plane towards the slot center. The prototype is shown in Fig. 5-8:

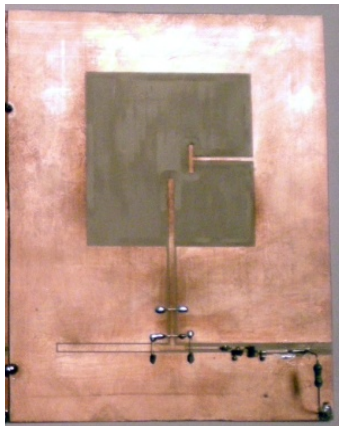

Fig. 5-8. Harvester propotype based on a coplanar-slot circularly polarized antenna - overall dimensions: 22×19 cm^2.

Tag performances are shown in Fig. 5-9 with respect to the same approach as in the previous section: conversion efficiency vs available power at the antenna terminals for several frequencies the GSM band. As before the dispersive behaviour of the antenna implies a slight difference in the rectenna capabilities – although the entire optimization process is regulated in a broadband configuration.

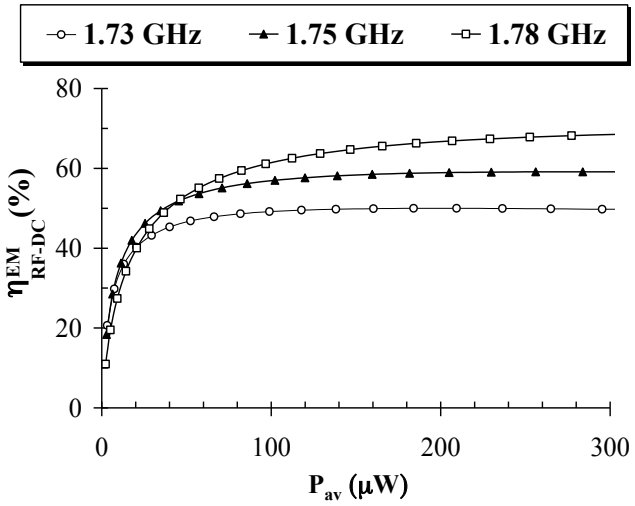

Fig. 5-9. Conversion efficiency of the circularly polarized harvester among three different frequencies inside GSM 1800 uplink band.

Measurements and theory are compared in Fig. 5-10 in terms of DC output power as a function of the measured incident power density at several operating frequencies

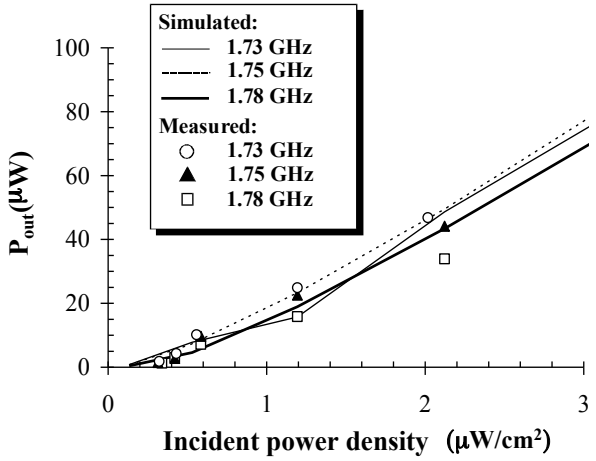

Fig. 5-10. Computed and measured DC output power for the circularly polarized harvester.

To best comprehend the versatility towards unknown RF sources, we assume here a single generic linearly-polarized electric field incident on the rectenna. The direction of polarization can be defined as follows:

$$\mathbf{E}_{\text{inc}_1} = \begin{cases} \left\|\mathbf{E}_{\text{inc}_1}\right\| \left(\cos\psi_1 \hat{\boldsymbol{\theta}} + \sin\psi_1 \hat{\boldsymbol{\phi}}\right) & \text{for } \theta_D \neq 0 \\ \left\|\mathbf{E}_{\text{inc}_1}\right\| \left(\cos\psi_1 \hat{\mathbf{i}} + \sin\psi_1 \hat{\mathbf{j}}\right) & \text{for } \theta_D = 0 \end{cases} \tag{5.5}$$

The coordinate systems and the angles refer to the scenario in Fig. 5-1; ψ_1 is the angle between the incident field direction of polarization and the θ-direction (for $\theta_D \neq 0$) or the x-direction (for $\theta_D = 0$). The receiving antenna is oriented in such a way that its broadside direction (for $\theta_D = 0$) is parallel to the ground, and its position is held fixed. In Figs. 5-11, 5-12 the rectified output power is plotted for several directions of incidence of $\mathbf{E}_{\mathrm{inc}_1}$:

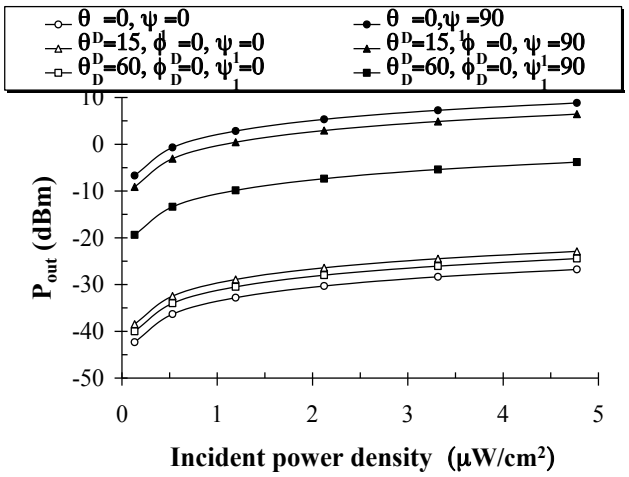

Fig. 5-11. Output DC power of the linearly polarised harvester for several directions of arrival of a linearly polarised incident RF field

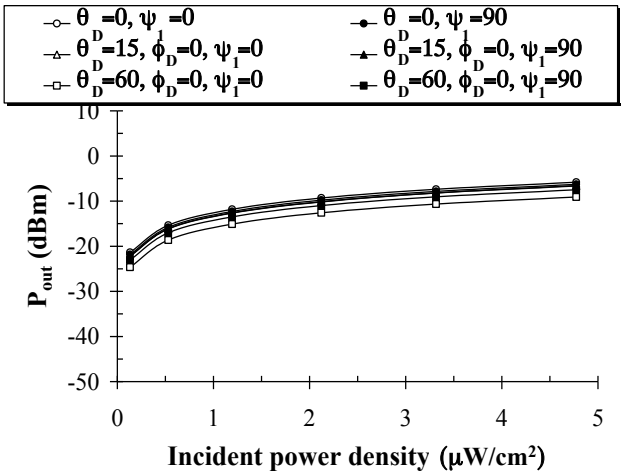

Fig. 5-12. Output DC power of the circularly polarised harvester for several directions of arrival of a linearly polarised incident RF field

The results for the 2×2 patch antenna harvester in the vertical direction, which is chosen to coincide with the y-axis, show that for $\theta_D = 0$, $\psi_1 = 90°$ the rectified DC power is highest due to a perfect polarization match between incident field and rectenna. However the harvested

power rapidly drops as the polarization mismatch increases. On the contrary the rectified power in case of a circularly polarized rectenna show much more versatility towards polarization angle.

Multi-frequency operation

The third example of harvester is aimed by the purpose to unify all the previous features into a unique architecture capable of exploiting three wireless standards at the same time from arbitrary directions of arrival and with unknown polarization. The exploitable RF sources are GSM 900, GSM 1800 and IEEE 802.11b, present in abundance in every humanized environment.

The answer for the specifications about multiband characteristics and circular polarization is a multilayer aperture-coupled printed antenna offering good integration properties, robustness and minimum thickness. The main advantage is a decoupling strategy between rectifier and antenna, in particular allowing the use of different kind of substrates, one for miniaturization purposes –for the microstrip feed line – and one ensuring good radiation efficiency – at the antenna side.

The complete scheme layer by layer is shown in Figs. 5-13, 5-14:

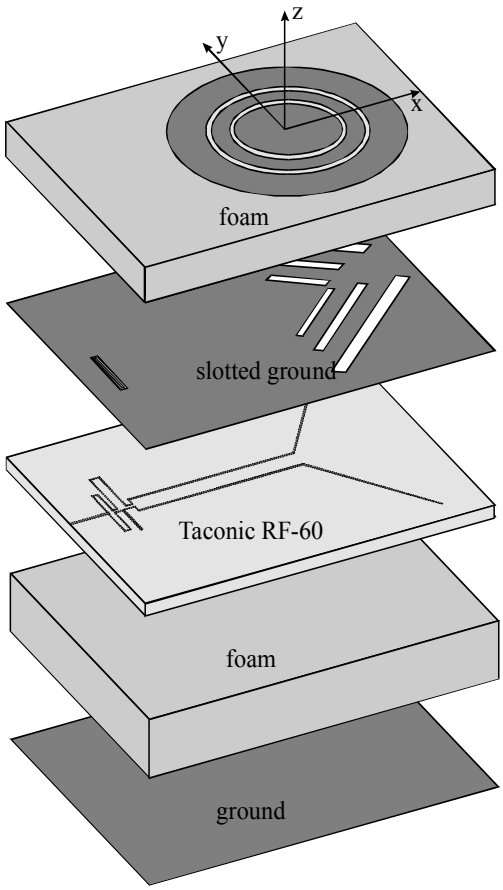

Fig. 5-13. Exploded view of the multilayer, multi-resonator rectenna.

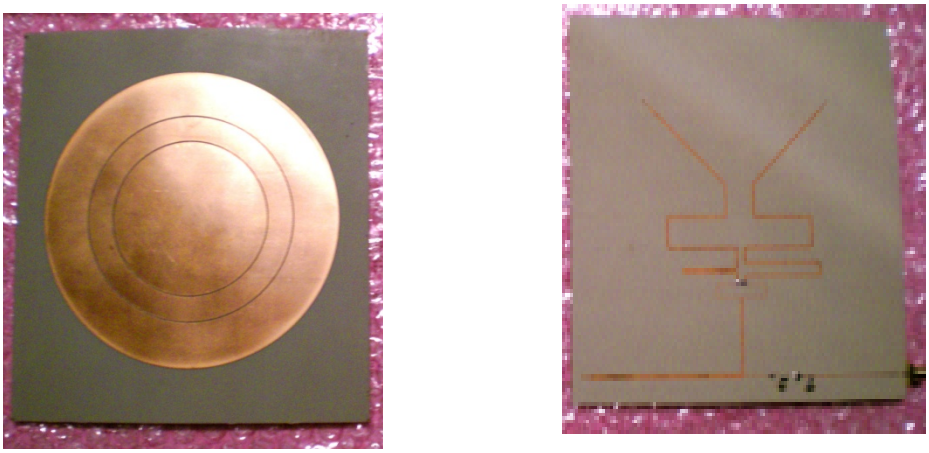

Fig. 5-14. Harvester propotype based on a multilayer, multi-resonator antenna - overall dimensions: 14 × 13 × 1.3 cm^2.

A three-band operation is achieved by exploiting the three structures on the top layer, i.e. the inner circular patch and the two proximity-coupled outer rings. At the highest frequency, the inner patch is active; in the intermediate frequency band, the active patch is obtained by coupling the inner patch with the inner ring; at the lowest frequency, the three structures make

up an approximately circular resonating patch. For each frequency band, the metallization not belonging to the resonant structure plays the role of a parasitic element and must be accounted for during the design process in order to check that it does not significantly affect the current distribution on the active patch or its radiating properties. To achieve this goal, the radius of the circular patch and those of the inner and outer rings are optimized together with the inter-element gaps by means of EM simulation all over the bands of interest.

On the ground plane of the circular patches (slotted ground in Fig. 5-13) two identical sets of three slots are etched to aperture-couple the bottom layer to the radiating patches. The two sets are orthogonal to each other in order to provide the antenna circular polarisation. The slot dimensions and relative positions are designed to simultaneously provide the tightest coupling and the smallest back radiation in each band of interest. This radiating structure, only a portion of which is active in each specific frequency band, may be conceptually related to the basic design concept of log-periodic antennas. Two orthogonal modes are excited by two symmetrical microstrip feed lines, printed on the Taconic substrate (Fig. 5-13). These lines depart from a 90-degree hybrid coupler whose topology, derived from [8], has beeen optimised to ensure acceptable return loss, equal power division between the output ports, and constant phase difference between the output ports over each frequency band of interest. The annular rings have outer radii of 57 mm and 41 mm, respectively, while the circular central patch has a 30-mm radius. The coupling gap widths are 0.5 mm. The three resonant slots obey the well-known relationship between working frequencies and physical lengths. Their 2-D sizes are 2.8 × 28 mm^2, 3 × 38 mm^2, and 5.5 × 65 mm^2, respectively, in order to approximately preserve a 1/10 ratio between length and width. The total thickness of the rectenna is approximately 1.3 cm. The dielectric supporting the patches consists of a 4 mm thick Polyurethanic foam (ε_r = 1.25, tanδ = 0.0012) ensuring mechanical stability, with negligible effects on antenna performances.

The 0.635 mm thick feeding circuit substrate under the ground plane is a Taconic RF-60 (ε_r = 6.15, tanδ = 0.0028). At the bottom the whole assembly is shielded by a ground plane separated from the feeding circuit by an 8 mm-thick foam layer. Such shielding guarantees isolation of the harvester in view of wearable applications. A broadband design of the antenna- rectifier matching network has been carried out together with the other design parameters described above. Figs. 5-15, 5-16 furnish an overview of simulated and measured performances in terms of return loss:

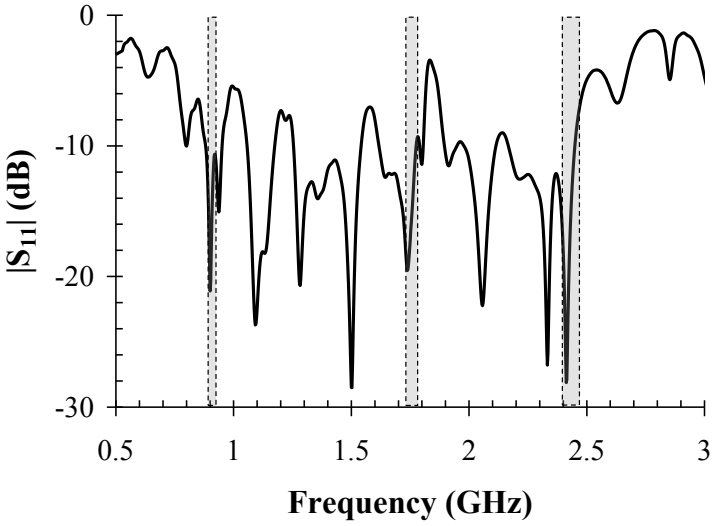

Fig. 5-15. Reflection coefficient for the stand-alone multilayer, multi-resonator antenna.

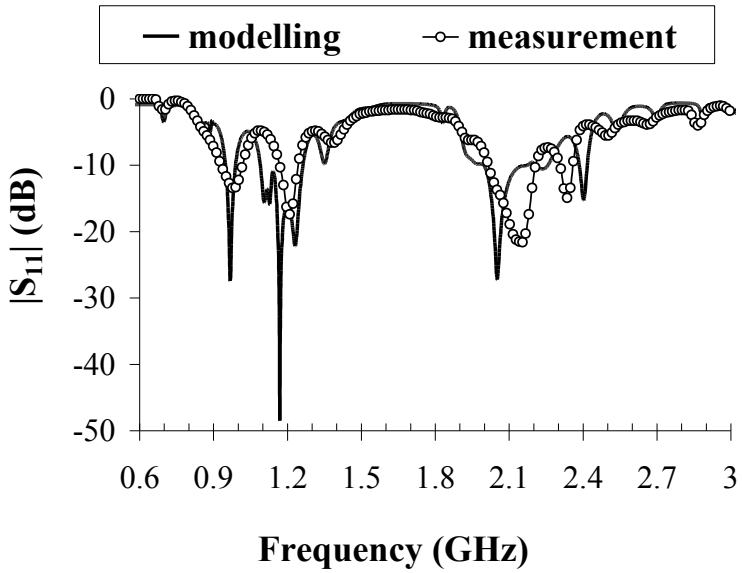

Fig. 5-16. Reflection coefficient for the antenna plus matching circuit.

With regard to the properties in terms of polarization, the normalized co-polarized and cross-polarized radiation patterns in the *x-z* plane at the center of each band, are plotted in Fig. 5-17 showing excellent circular polarisation performance: an axial ratio of more than 4 dB has been obtained all over the related bands. Similar behaviours are obtained for the *y-z* plane and are not plotted for brevity.

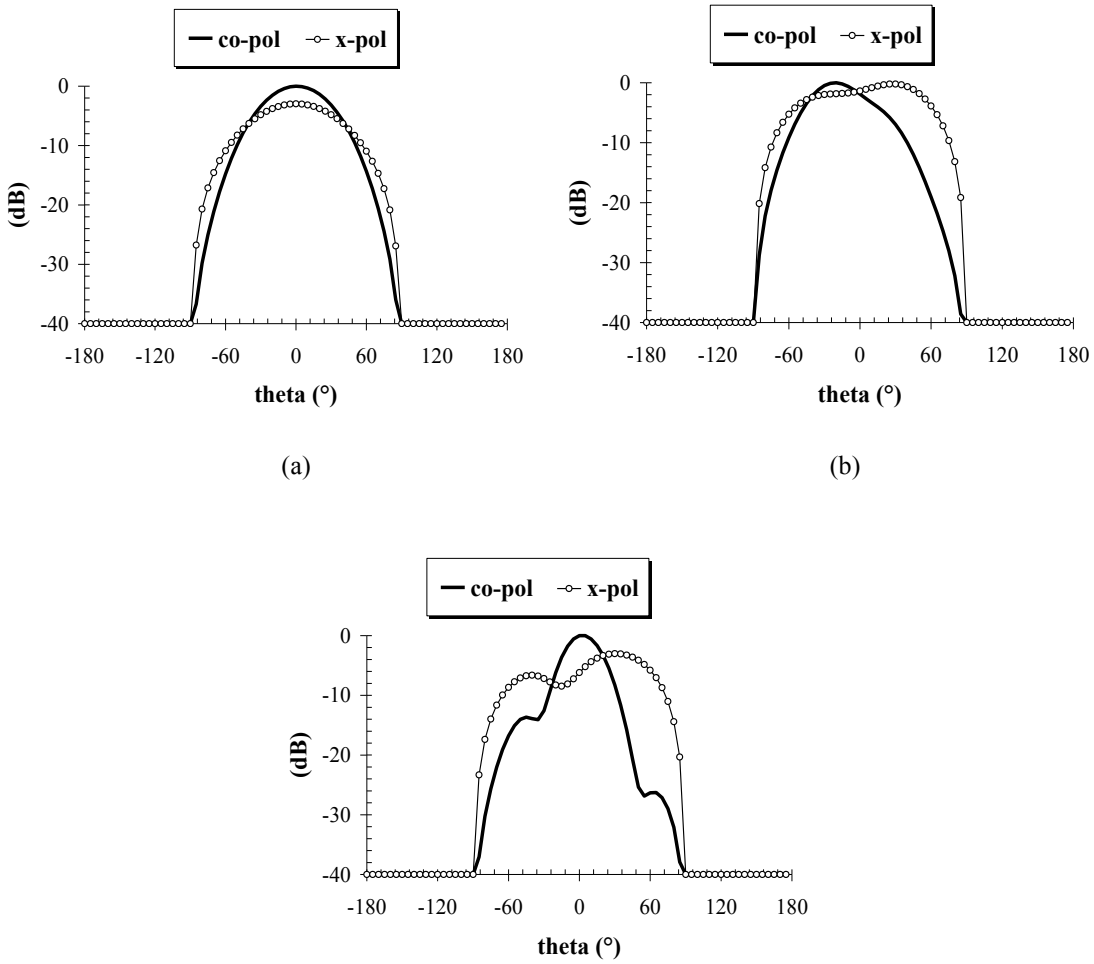

Fig. 5-17. *x-z* plane normalized radiation pattern for (a) 900 MHz, (b) 1.76 GHz and (c) 2.450 GHz

The antenna directivity is roughly constant (3.6 dB, 2.3 dB, and 3.4 dB, in the GSM 900, GSM 1800 and IEEE 802.11b bands, respectively) which implies that the effective area is strongly dependent on frequency, as shown in Fig. 5-18. As a consequence, the incident field power density that is required in order to produce a constant RF available power is strongly frequency dependent, as well. These power densities are also reported in Fig. 5-18 for P_{av} = 500 μW at the centre frequency of each band of interest.

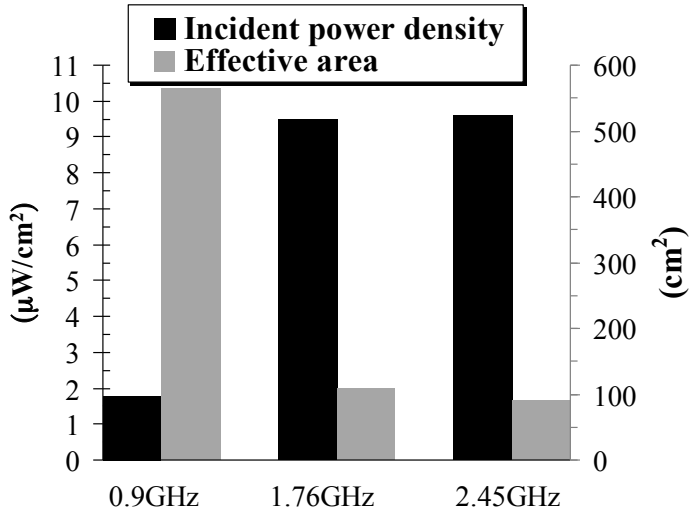

Fig. 5-18. Incident power density required to provide a 500 μW RF available power and effective area at each operating frequency

The design of the whole rectenna is carried out for a [-16 dBm +8 dBm] RF available power range. The large upper bound is chosen in order to guarantee that rectenna can handle high power levels, which may be encountered in some practical cases, e.g. when it is placed in a closed proximity of a radio base station. This choice corresponds to a maximum incident field intensity of 20 V/m. The load resistance R_L, that plays a crucial role in achieving the best conversion efficiency, is determined inside the same procedure. It is worth noting that R_L = 6.3 kOhm - the optimal value in this case - is meant to be comprehensive of the whole load. A new dynamic-switching conversion scheme based on active control for harvesting energy is under development and will be presented in future publications. Fig. 5-19 summarises the optimisation results by comparing the converted DC power to the actual power density and to the corresponding available RF power. Efficiency is better than 60% at the centre frequency of each band; for a given available RF power, significantly variable incident power levels are required at each design band.

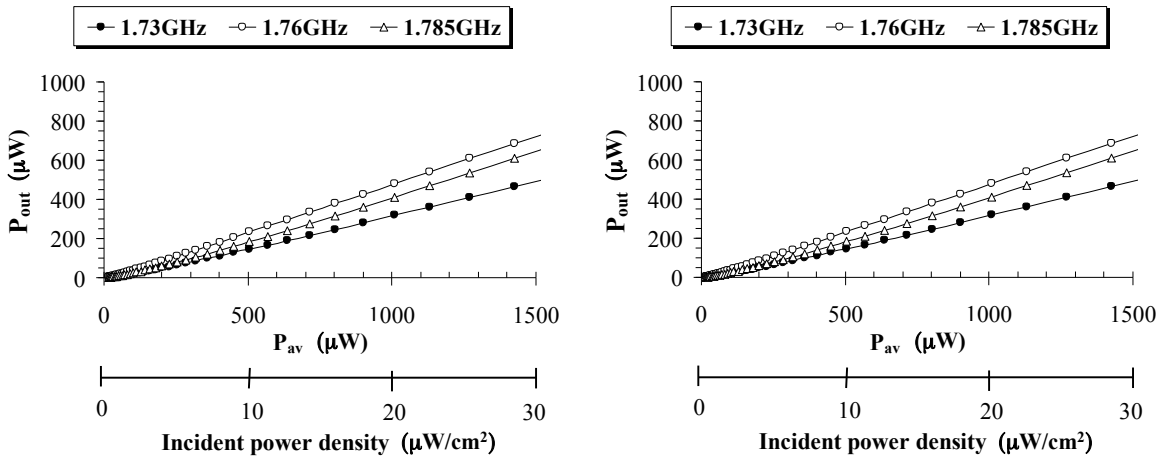

(a) (b)

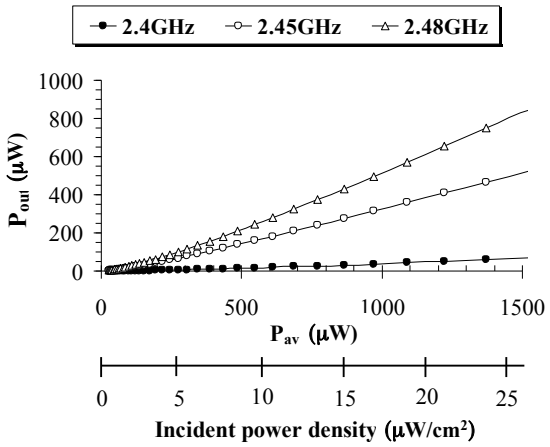

(c)

Fig. 5-19. Harvested power vs incident power density and RF available power: (a) in the GSM 900 band, (b) in the GSM 1800 band, (c) in the IEEE 802.11b band

The integrated procedure developed in this thesis allows the harvesting capabilities under multi-source excitation to be accurately predicted. Some results are plotted in Fig. 5-20 for three possible combinations of RF available powers in the three frequency bands. A comparison with the results of Fig. 5-19 puts into evidence the usefulness of our approach: three-tone excitation determines a frequency spectrum with intermodulation products whose effect cannot be a priori established and the multi-source operation cannot be simply predicted as a superposition of three single-tone ones. Furthermore, the complex frequency dependence of the antenna impedance is directly accounted for in this way.

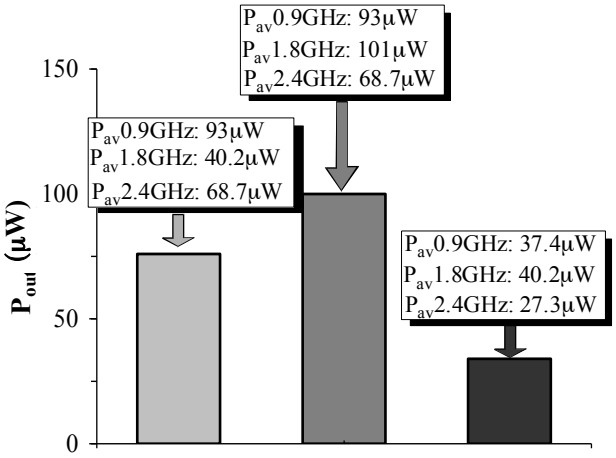

Fig. 5-20. Actual harvested power in the simultaneous presence of three RF sources for several combinations of RF available power levels.

Finally the multi-source RF harvesting design procedure has been validated by measuring its performance at ultra-low incident power densities. Fig. 5-21 (a) and (b) compare the predicted and measured DC output power when harvesting from a GSM 900 and a WiFi source, respectively.

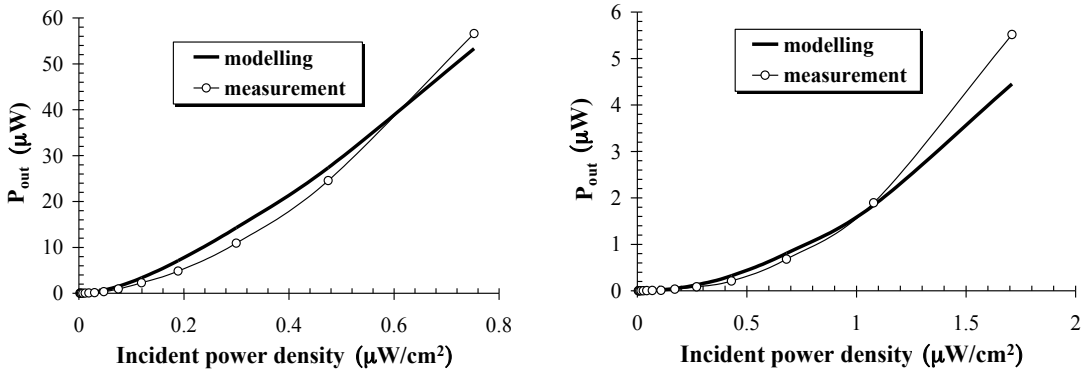

(a) (b)

Fig. 5-21. Measured and simulated converted DC power: (a) at 900 MHz, (b) at 2.450 GHz

REFERENCES

[1] V. Rizzoli, A. Costanzo, M. Rubini, D. Masotti, "Investigation of Interactions Between Passive RFID Tags By Means of Nonlinear/EM Co-Simulation", *Proc. 36th Europ. Microwave Conf.*, pp. 722-725, Sept. 2006.

[2] G. de Vita, G. Iannaccone, “Design criteria for the RF section of UHF and microwave passive RFID transponders”, *IEEE Trans. Microwave Theory and Techniques,* Vol. 53, pp. 2978-2990, September 2005.

[3] N. Shinohara, H. Matsumoto, “Experimental study of large rectenna array for microwave energy transmission”, *IEEE Trans. Microwave Theory and Techniques,* Vol. 46, pp. 261-268, March 1998.

[4] J. P. Curty, N. Joehl, C. Dehollain, M. J. Declercq, “Remotely powered addressable UHF RFID integrated system”, *IEEE Journal of Solid State Circuits*, Vol. 40, pp. 2193-2202, November 2005.

[5] V. Rizzoli, A. Costanzo, G. Monti, “General electromagnetic compatibility analysis for nonlinear microwave integrated circuits”, *2004 IEEE MTT-S Int. Microwave Symp. Digest*, Fort Worth, TX, pp. 953-956, June 2004.

[6] J. Essel, D. Brenk, J. Heidrich, R. Weigel, “A highly efficient UHF RFID frontend approach”, *IEEE MTT-S International Microwave Workshop on Wireless Sensing, Local Positioning and RFID (IMWS 2009 – Croatia),* Digest of Papers, 2009, 1-4

[7] J. Y. Sze, K. L. Wong, C. C. Huang, “Coplanar waveguide-fed square slot antenna for broadband circularly polarized radiation” *IEEE Trans. Antennas and Propagation,* Vol. 51, pp. 2141-2144, August 2003.

[8] Y. X. Guo, Z. Y. Zhang, L. C. Ong, “Improved wide-band Schiffman phase shifter”, *IEEE Trans. Microwave Theory and Techniques,* Vol. 54, pp. 1196-1200, March 2006.

PASSIVE RFID AT MILLIMETER WAVES

In the following paragraphs a novel way to implement passive RFID at millimeter waves is introduced. The aim is to exploit all the advantages of mm-wave identification systems in terms of *transponder* (tag) localization and miniaturization, through a commercial-device-based philosophy. The approach proposed in the thesis is again applied to the design and optimization of the passive transponder.

The study has been carried out in a 6-month stage at VTT Technical Research Centre of Finland (Espoo, Finland).

Motivation

Radio Frequency Identification (RFID): generalities

Radio based identification technique has developed in a variety of forms over the past decades, including keyless entry badge readers, automatic toll collection, smart cards, etc. However, modern Radio Frequency Identification (RFID) systems trace their roots to military *identification friend or foe* (IFF) systems that appeared in the Second World War, at about the same time as radar. One of the first consumer applications of RFID was access control, and key cards based on an inductive near field coupling are widely used even today. Then the availability of inexpensive CMOS technology and mostly the possibility to integrate Schottky diodes into CMOS processes enabled passive RFID – with no need for a battery – at Ultra High Frequencies (UHF) with reasonable cost and read range, at the end of 1990's.

Further developments are eagerly awaited in the field of logistic chain management, given that an automatic identification mechanism replaces manual work. As mentioned before many companies use inductive RFID-based access key cards in their offices. Car immobilizers as well. Various typologies of sensors are already being implemented with RFID tags.

A system overview

The identification system consists of a reader and a number of transponders able to uplink communication through a backscattering modulation mechanism. A general view of regulations and standards is beyond our purposes but the major classification of RFID

systems at the moment relies on 1) EM coupling, 2) operation frequency and 3) transponder powering.

In the first branch a subdivision should be made between *inductive-coupling*, *capacitive-coupling* and *electromagnetic-coupling* RFIDs. In the first two cases the near-fields of a coupling element, such as a coil or a capacitor, are the vehicle for carrying information between reader and transponder. In the third case the reader is excited in a farfield zone of the transponder.

The operation frequency goes hand-in-hand with the coupling mode: low frequencies – especially from 100 kHz to 13.56 MHz – are dedicated to near-field couplings; in particular the 13.56 MHz band is globally reserved for inductive RFID. The third tipology of link lies generally between 400 MHz and 5 GHz, but mostly around 900 MHz.

Finally, RFID systems are classified as *passive* – with the tag powered up by the incident RF power from the reader – or *semipassive* – with a battery-assisted tag but still relying on backscattering modulation for uplink – or *active* – capable of generating an RF carrier from the battery for uplink transmission.

Most of the interest in RFID over the last years has been concentrated on UHF RFID bringing the read range up to 10 meters with transponders that cost less than 10 Euro cent.

A conceptual block scheme for a generic passive UHF RFID system is depicted in Fig. 6-1:

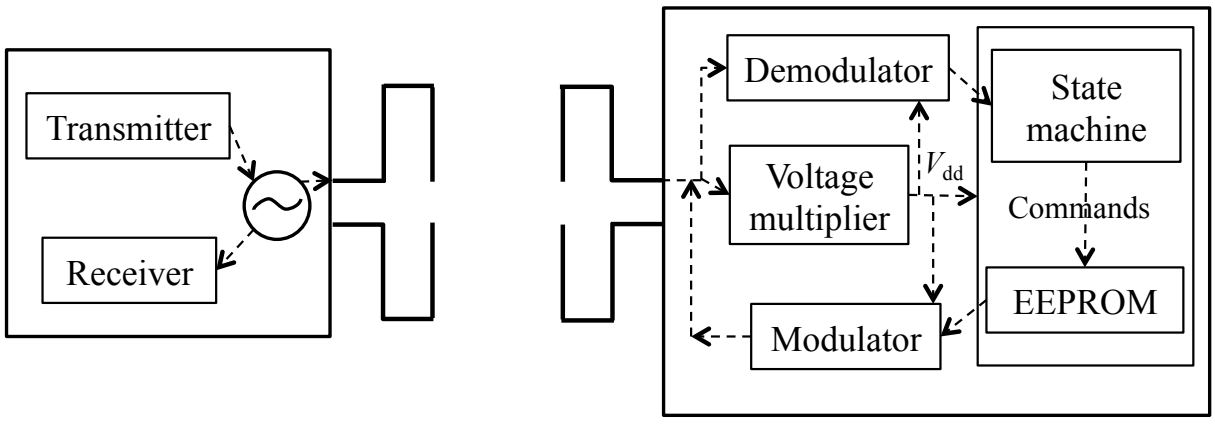

Fig. 6-1. Block diagram for a UHF RFID reader (left side) and transponder (right side)

Part of the RF signal incoming from the reader is converted to DC by a voltage multiplier operating as a power supply for all active circuits in the chip. The demodulator converts the modulated input signal to digital data and generates a synchronous system clock, and the EEPROM is thus driven by a sequence of commands. Finally, the modulator turns the data –

acknowledgements of the received commands or data from the EEPROM – from control logic into variations in the tag input impedance using a MOS varactor. The logic circuitry handles the communication protocol, cyclic redundancy checks, anticollision features, and so on.
In the present work thesis only monostatic readers will be considered – as in the picture above, thus including a circulator device.

Limitations and proposed solution

Despite the countless number of advantages of such technology, UHF RFID systems lack of efficient locating capabilities: both signal strenght (RSSI, e.g. [1]) or phase (e.g. [2],[3]) are used exclusively for ranging the tags. The direction of the tag would require either multiple antennas and trilateration or a narrow-beamed, highly directional reader antenna, enabling localization by manual scanning or by angle-of-arrival (AoA). Especially the last solution is impractical at the working frequency of, e.g. 900 MHz, because of the resulting massive dimensions of the antenna itself.
On the other hand at millimeter waves a directional small radiating element can be easily designed and integrated [4][5], but a straightforward implementation of the entire existing RFID system has a significant drawback: the rectifier in the tag – the key component for passive tag operation. Efficiencies of 60% can be obtained at UHF (see previous chapter), but although scaling of CMOS to higher frequencies has enabled the design of integrated rectifiers at millimeter waves also [6], rectification at low power levels is nevertheless too inefficient at those frequency ranges.

An intriguing alternative solution is presented here to exploit the benefits of millimeter-wave radio design in conjunction with UHF RFID technology: in integration of a commercial RFID chip into a microwave or millimeter-wave front-end. The block scheme is furnished in Fig. 6-2.

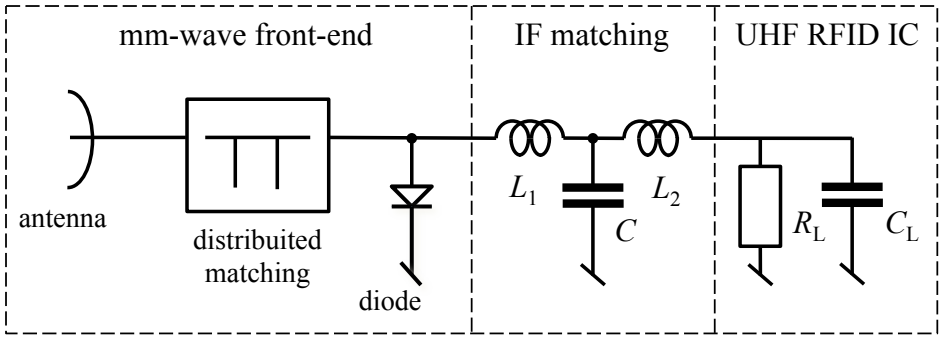

Fig. 6-2. Block diagram of the proposed millimeter wave RFID tag

Such tag design principle – totally passive – makes use of an external nonlinear component between tag antenna and RFID chip for mixing millimeter waves to RFID carrier frequency for a standard RFID chip, as illustrated in picture above. The tag receives a millimeter wave carrier at ω_0 with the UHF RFID signal in sidebands at $\omega_0 \pm \omega_{IF}$, with ω_{IF} in a range of [850 ÷ 950] MHz. The received signal is down-converted in the external mixing element – here a Schottky diode – to ω_{IF}. This UHF signal is then fed to the UHF RFID chip, which operates as usual. Modulation of the RFID chip at $\omega_{IF} \pm \omega_{mod}$ propagates similarly through the mixing element to frequencies $\omega_0 \pm \omega_{IF} \pm \omega_{mod}$, which are then transferred through the tag antenna to the reader's receiver antenna.

The reader setup consists of a standard UHF RFID reader on PCB, whose TX/RX output is connected to an external circulator (Fig. 6-3). The TX signals are up-converted in an external mixer to millimeter-waves, amplified and fed to a directive millimeter-wave antenna. The transmission includes the mm-wave carrier frequency ω_0 and the sidebands at $\omega_0 \pm \omega_{IF}$. The received signal is similarly down-converted by an external mixer to $\omega_{IF} \pm \omega_{mod}$, which is fed to the UHF RFID reader again.

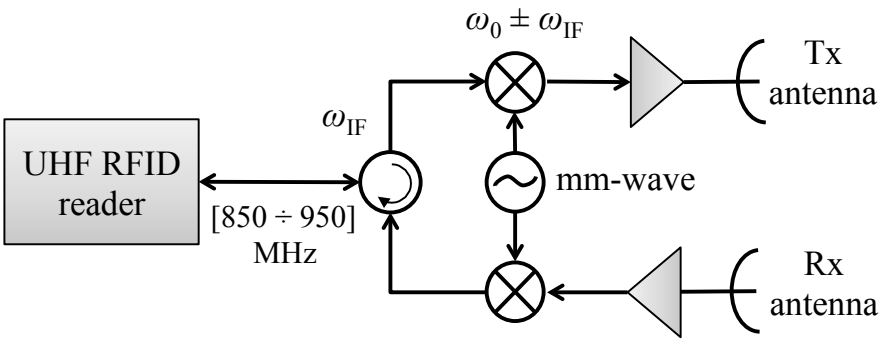

Fig. 6-3. Reader block diagram

The entire system enables passive RFID communication with standard EOC protocol, including all the features of the UHF RFID, such as anticollision, data rates, etc. In this paper, operation is demonstrated at 10 GHz, but the idea works at any carrier frequency substantially higher than Ultra High Frequencies. Also HF RFID chips could be used, but their power consumption is higher than UHF chips, leading to even shorter range. On the other hand, semipassive UHF RFID chips have better sensitivity than passive ones, which would theorically enable higher range.

Theory

Theoretical analysis of the tag can be divided to two separate parts by speculatively assuming that the millimeter wave matching circuit presents a high impedance at UHF, and vice versa. We model the diode as an ideal nonlinear resistor through the well-known exponential *I-V* relation:

$$I_D = I_0\left(e^{qV_D/nkT} - 1\right) \tag{6.1}$$

Further, we assume constant diode capacitance, which can be bundled into the matching network in the following analysis. Omitting the reactive matching the tag is presented in Fig. 6-4, with a simplified scheme capable to illustrate the operation principle of the external mixing element.

In practice, the nonlinear capacitance also affect the results and it is taken into account in the detailed simulation in the next section.

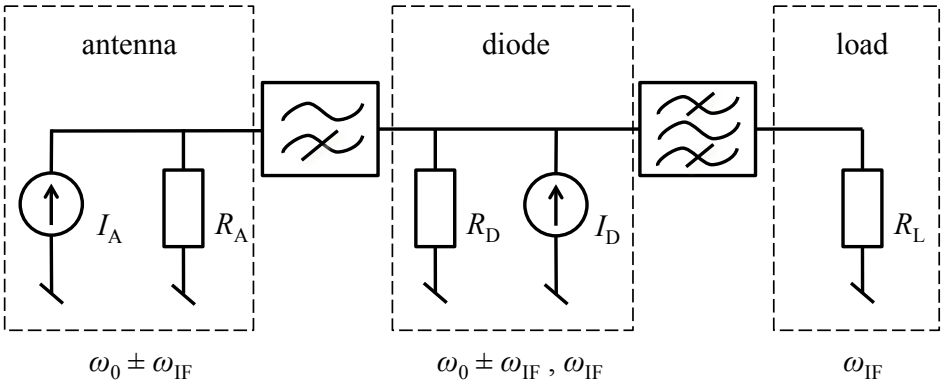

Fig. 6-4. The circuit schematic for theoretical analysis.

Power conversion efficiency in forward link

The antenna is modeled as a current source I_A with internal resistance R_A. The antenna receives three tones from the reader device: carrier at ω_0 and sidebands at $\omega_0 \pm \omega_{IF}$. The highpass and bandpass filters divide the circuit into two subparts: the millimeter-wave domain with antenna highpass filter and diode, and IF domain with diode and load.
The antenna current is hence written as

$$I_A = A_1 \sin(\omega_0 t) + A_2 \sin\left[(\omega_0 + \omega_{IF})t\right] \tag{6.2}$$

The maximum voltage over the diode is

$$V_D = \frac{R_A R_D}{R_A + R_D} I_A = \frac{R_D}{2} I_A \tag{6.3}$$

with the last expression under the hypothesis of simmetric current divider – i.e. $R_A = R_D$.
At the UHF section, the diode is modeled as a current source defined by the Taylor expansion of the ideal diode *I-V* curve:

$$I_D = I_{D0} + \left(\frac{\partial I_D}{\partial V_D}\right) V_D + \frac{1}{2}\left(\frac{\partial^2 I_D}{\partial V_D^2}\right) V_D^2 \tag{6.4}$$

and, assuming zero DC bias $(I_{D0} = I_0)$, we get to the second order

$$I_D = I_0 + \frac{A_1}{2}\sin\left(\omega_0 t\right) + \frac{A_2}{2}\sin\left[\left(\omega_0 + \omega_{IF}\right)t\right] + \frac{1}{2^3}R_D\gamma\{A_1^2 + A_2^2 - A_1^2\cos\left(2\omega_0 t\right) - \\ - A_2^2\cos\left[2\left(\omega_0 + \omega_{IF}\right)t\right] + 2A_1A_2\cos\left(\omega_{IF}t\right)\}. \tag{6.5}$$

here we have used the relations

$$R_D = \left(\frac{\partial I_D}{\partial V_D}\right)^{-1}, \qquad \gamma = \left(\frac{\partial^2 I_D}{\partial V_D^2}\right)\Big/\left(\frac{\partial I_D}{\partial V_D}\right) \tag{6.6}$$

The part of the signal delivered by the UHF matching network is

$$I_D = \frac{1}{4}R_D\gamma A_1 A_2\cos\left(\omega_{IF}t\right) \tag{6.7}$$

hence the power delivered to the load R_L is

$$P_L = R_L\left(\frac{1}{1 + R_L/R_D}\left|I_D\right|\right)^2 = \frac{A_1^2A_2^2}{2^7}R_D^3\gamma^2 \tag{6.8}$$

at conjugate match. This is maximized when $A_1 = A_2$, which gives for the power P_A available from the reader field

$$P_A = R_A\left(\frac{1}{1 + R_A/R_D}\left|I_A\right|\right)^2 = \frac{A_1^2R_D}{2^2} \tag{6.9}$$

Forward link conversion efficiency α_f is the ratio of P_L to the power P_A available from the reader field

$$\alpha_f = \frac{P_L}{P_A} = \frac{A_1^2}{2^5}R_D^2\gamma^2 = \frac{P_A}{2^3}R_D\gamma^2 \tag{6.10}$$

The system can be designed for single or dual sideband transmission. The former requires twice the bandwidth but enhances the available power at the chip side. (6.3) would become

$$V_{\mathrm{D}} = \frac{R_{\mathrm{D}}}{2}\left\{A_0 \sin(\omega_0 t) + \sum_{-,+} A_{\pm} \sin\left[(\omega_0 \pm \omega_{\mathrm{IF}})t\right]\right\} \tag{6.11}$$

All the following formulas should be changed accordingly.

Return link conversion efficiency

Communication on return link is based on backscattering modulation. The UHF RFID chip modulates its input impedance, in this model its resistance by a value of ΔR_{L}. The modulation in the chip resistance is seen as a change in the voltage over the diode

$$V_{\mathrm{D}} = \Delta R_{\mathrm{L}}\left(\frac{\partial}{\partial R_{\mathrm{L}}}\frac{R_{\mathrm{D}}R_{\mathrm{L}}}{R_{\mathrm{D}}+R_{\mathrm{L}}}\right)I_{\mathrm{D}} = \frac{1}{2^4}R_{\mathrm{D}}^2\gamma\frac{\Delta R_{\mathrm{L}}}{R_{\mathrm{L}}}A_1A_2\cos\left(\omega_{\mathrm{IF}}t\right) \tag{6.12}$$

where the latter equality follows from evaluating the derivative at the complex conjugate match. This voltage represents a third input voltage for the diode, leading to new output current components from the diode nonlinearity. By developing a similar analysis as in the previous paragraph the output current component at $\omega_0 \pm \omega_{\mathrm{IF}}$

$$I_{\mathrm{D}} = \frac{1}{2^5}R_{\mathrm{D}}^2\gamma^2\frac{\Delta R_{\mathrm{L}}}{R_{\mathrm{L}}}A_1^2A_2\cos\left[\left(\omega_0+\omega_{\mathrm{IF}}\right)t\right] \tag{6.13}$$

similarly the power delivered to antenna at conjugate match is

$$P_{\mathrm{A,return}} = \frac{A_1^4A_2^2}{2^{13}}R_{\mathrm{D}}^5\gamma^4\left(\frac{\Delta R_{\mathrm{L}}}{R_{\mathrm{L}}}\right)^2 \tag{6.14}$$

The return link power conversion efficiency α_r is the ratio of the power returned to the antenna $P_{\text{A, return}}$ and the power P_{A} available from the reader field, evaluated at the optimal power condition of the forward link, i.e. $A_1 = A_2$

$$\alpha_r = \frac{P_{\text{A,return}}}{P_{\text{A}}} = \frac{P_{\text{A}}^2}{2^7} R_{\text{D}}^4 \gamma^4 \left(\frac{\Delta R_{\text{L}}}{R_{\text{L}}} \right)^2 = \frac{1}{2} \left(\frac{\Delta R_{\text{L}}}{R_{\text{L}}} \right)^2 \alpha_f^2 \tag{6.15}$$

The return link power conversion efficiency is proportional to the forward link conversion efficiency squared and the modulation index $\Delta R_{\text{L}} / R_{\text{L}}$ squared. Hence the diode attenuates the incoming and outgoing signals equally, as does the free space between the reader and the tag.

Simulations

An accurate antenna characterization through EM simulation is compulsory for a correct nonlinear optimization process. The nature of the problem imposes a new antenna topology and a suitable EM tool for the analysis.

HFSS

One serious weakness of FIT method is the staircase approximation for curved surfaces based on cubic cells: the resulting grid becomes computationally demanding and too heavy to handle.

Ansoft HFSS simulator is a 3D EM solver based on *Finite Element Method* technique (FEM). FEM involves subdividing a large problem into individually simple constituent units which are each soluble via direct analytical methods, then reassembling the solution for the entire problem space as a matrix of simultaneous equations. Model ‘subdivision’ is generally accomplished by use of tetrahedral elements which are defined to fill any arbitrary 3D volume: given that EM properties can differ from element to element inhomogeneus structures can be modeled.

Modern versions of FEM simulators include Delaunay 3D tessellation algorithms. Therefore the required mesh density for particular topologies is furnished by some built-in intelligence: high density meshing corresponds to somehow critical points or hard discontinuities in EM

field values. It is very easy to define arbitrary geometries with various levels of resolution in the problem space.

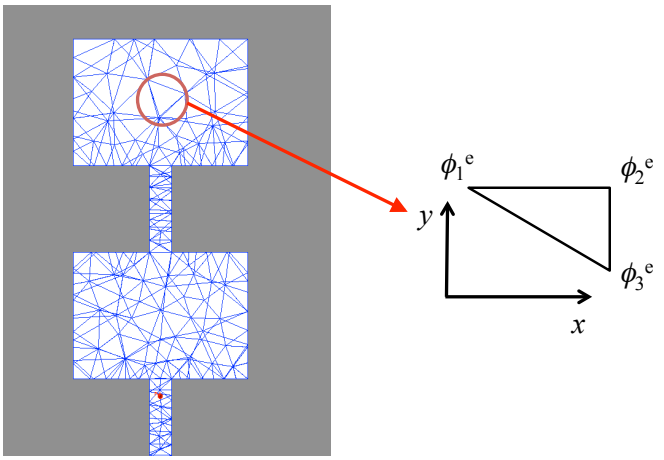

Fig. 6-5. Mesh view from HFSS: discretization into triangular (2D) – or tetrahedral (3D) – finite elements.

As all general-purpose field simulators here the approach of subsectional basis function is exploited: the finite subsections (finite elements) over which they are defined, are contiguous and of the simplest possible shape, which provides maximum flexibility in the discretization of arbitrary shapes.

The primary unknown quantity in FEM analysis is a field or a potential: subsectional basis functions are usually linear functions expressed in terms of the potential or field values at the vertices of the finite elements: continuity is thus preserved. Considering the triangular (2D case) decomposition in Fig. 6-5, the potential expression ϕ^e within the subdomain element can be thus expressed as

$$\phi^e = \sum_{n=1}^{3} N_n^e \phi_n^e \tag{6.16}$$

with N^e as shape-functions.

The proceeding of final solution expansion with a set of unknown coefficients is regulated by the minimization of EM energy among the discretized structure expressed by a suitable integral function. The minimization can be implemented by putting the functional's first derivatives with respect to all coefficients equal to zero (Rayleigh-Ritz procedure).

Unlike FIT, FEM solution is created in the *frequency domain*, assuming steady-state behaviour.

Antenna design

The necessity to operate at microwave frequencies force us to operate as follows: at the transmitter side a baseband AM-modulated signal will be produced by an ordinary DSP-based RFID reader and internally up-converted to ω_{IF} among a range of [0.86 ÷ 0.96] GHz. Then an external customized mixer will perform the follow-up conversion to $\omega_0 \pm \omega_{IF}$ by a suitable oscillator tone ω_0 – at 10 GHz in this case – at the end of our reading bloch scheme.

The double up-conversion architecture implies a transmitted relative signal bandwidth $\omega_{IF} / \omega_0 = 10\%$ at least – by means of a suitable image-rejection mixer – and the necessity to require huge-bandwidth antennas. An endfire Vivaldi planar topology was preferred due to its simple structure, high gain, good efficiency and wide band. Its working mechanism consisting of high order modes generated by wave travelling down a curved path along the antenna was firstly described by Gibson in 1979 [7]. The most critical elements for the antenna performances such as microstrip-to-slotline transition and exponential tapered parts have been analyzed and refined by HFSS 3D Simulator.

Rogers RO4350B (h = 0.762 mm, Cu ½ oz, ε_r = 3.66, tanδ = 0.004) was chosen for the substrate material. The layout of the antenna is shown in Fig 6-6. The differences between measured and simulated return losses (Fig. 6-7) are most probably due to fabrication tolerance in the very narrow tapered slot in the microstrip-to-slotline transition.

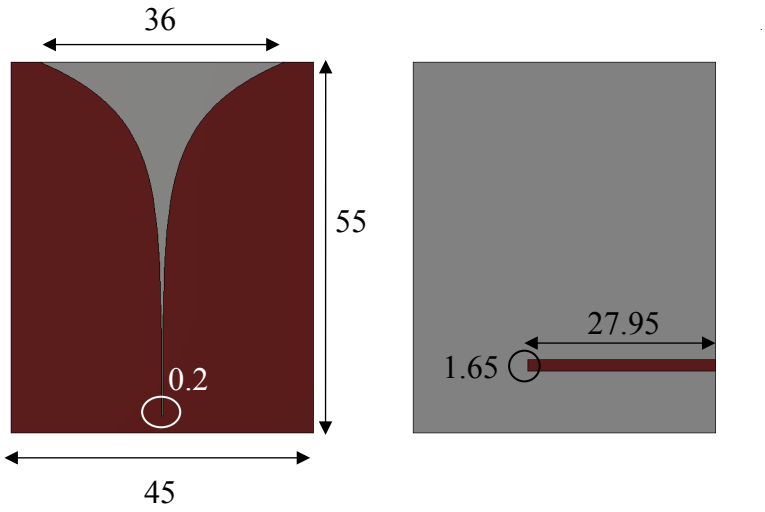

Fig. 6-6. Vivaldi antenna layout – top and bottom view. Dimensions in mm

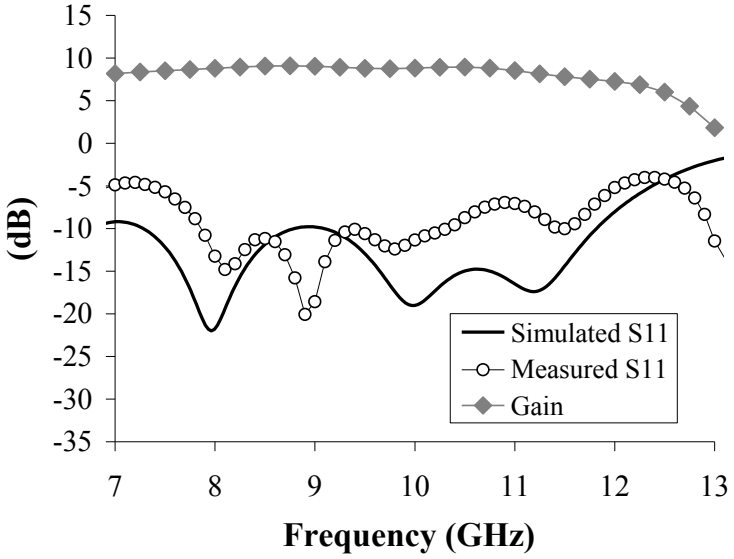

Fig. 6-7. Antenna Return Loss and Gain

The radiation pattern is furnished in Fig. 6-8 on E- and H-plane respectively. The single antenna does not provide an exceptional beam for efficient angle-of-arrival localization of the tags: reminding that an antenna array would be impractical at 10 GHz, to better demonstrate the localization a higher carrier frequency would be required.

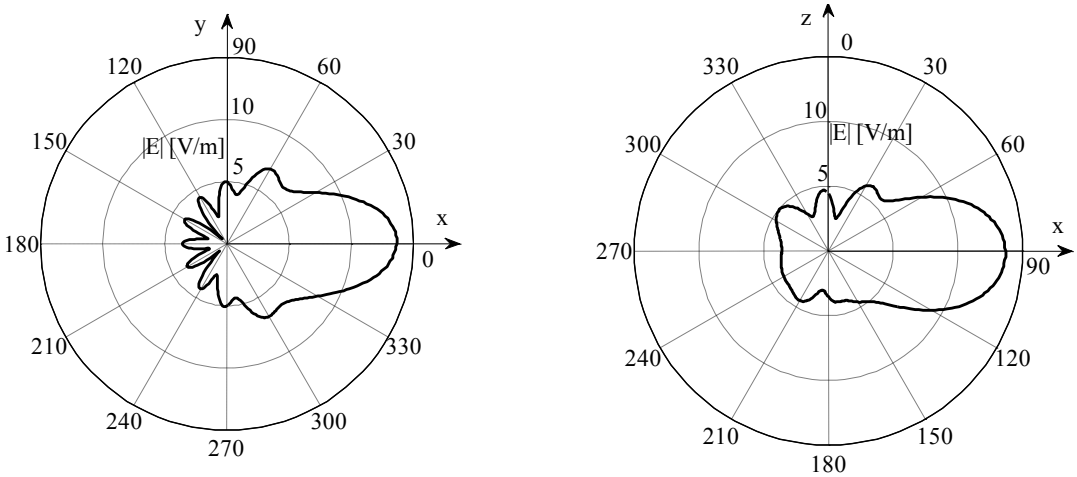

(a) (b)

Fig. 6-8. Antenna radiation pattern on (a) E-plane, (b) H-plane

Front-end design considerations

Since the ordinary RFID chip is expected to be operating at UHF (850 - 950 MHz), the tag working principle will basically consist of a nonlinear harmonic generation provided by a

single-diode mixer - simplest and most effective topology in the present case - with local oscillator tune furnished by the incoming continuous wave at ω_0 from the transmitter: the load will be only interested by the intermodulation product at ω_{IF} at the chip's side. A key feature in the mixer design is the choice for a suitable diode, in this case an Avago Technologies HSMS-286B (C_{j0} = 0.18 pF, $I_s = I_0$ = 50 nA, N = 1.08 and V_j = 0.65 V); then a suitable matching section between antenna and nonlinear device should be included and refined by means of *conversion gain* optimization goal. The simulations take fully into account also the nonlinear capacitance of the diode.

Inside the optimization loop without any loss of generality we will assume that the two driving tunes are sinusoidal, with incommensurate fundamental frequencies ω_0 and ω_{RF}. A minimum power of -14 dBm at ω_{IF} is required for the selected RFID IC - Alien Technologies Higgs 2 - in the acknowledgement phase. A block diagram of the tag is presented in Fig. 6-9 and a photograph of the tag in Fig. 6-10.

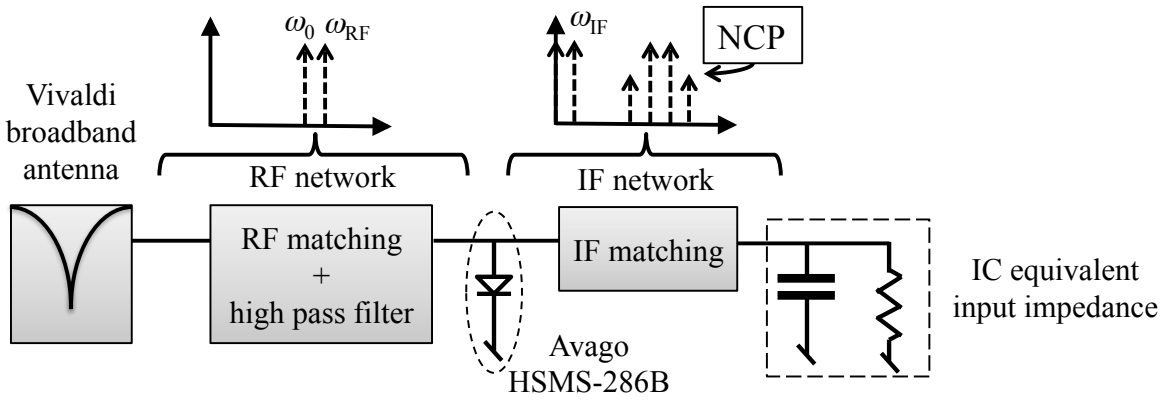

Fig. 6-9. Front-end block diagram

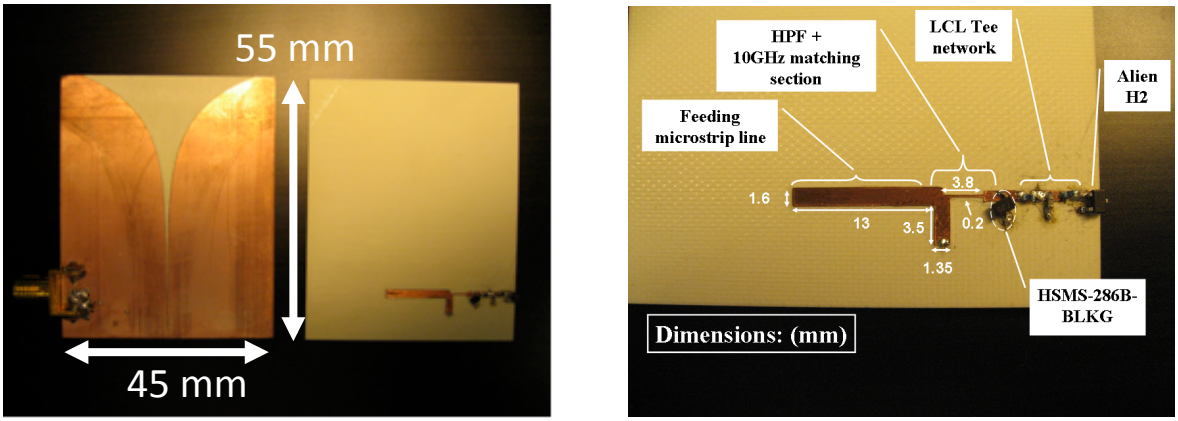

Fig. 6-10. Final Tag detailed view

The whole front-end can be roughly divided into two distinct subnetworks according to the respective working frequencies: the first one, depicted as RF network, provides for a conjugate matching between antenna and front-end in the neighborhood of the carrier wave – thus considering ω_{IF} as generically comprised in a range of 850 - 950 MHz depending on the communication protocol standard; at the same time a High Pass Filter (HPF) at 9.1 GHz is inserted to operate in conjunction with the antenna return loss for bouncing the consistent near-carrier intermodulation products (NCP in the picture) between antenna itself and IF network. Inserted to remix NCP's at the diode and thus form more IF power, HPF is simply realized by a shunt short-stub followed by a microstrip line.

The lumped Tee section is introduced as a band-stop filter for 10 GHz harmonic, exploiting inductors' self resonances – in this case 12 and 5.5 GHz respectively. Final values for the three lumped elements are 3.3 nH, 4.3 nH and 1.5 pF respectively.

A lumped shunt RC equivalent circuit is sufficient to model the electrical chip behaviour: in this case the nominal values of R = 1500 Ω and C = 1.2 pF were assigned and then successfully checked.

All the blocks have been modeled and refined by a unique optimization loop: all the parasitic effects due to diode package 0201 are taken into account. The entire front-end is totally passive. The simulated conversion gain is given in Fig. 6-11.

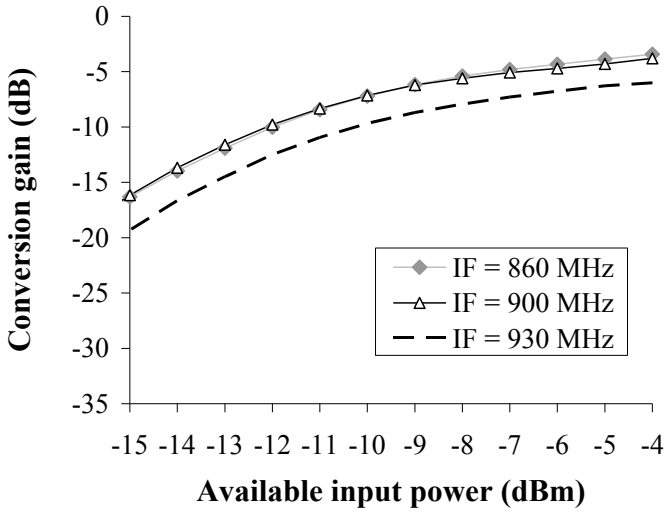

Fig. 6-11. Estimated conversion gain at different frequencies and input power levels.

Range estimation

The analysis approach introduced in the third chapter was succesfully exploited for reading range prediction. The scenario in Fig. 6-12 immediately recalls Fig. 5-1, with just a single incoming RF source:

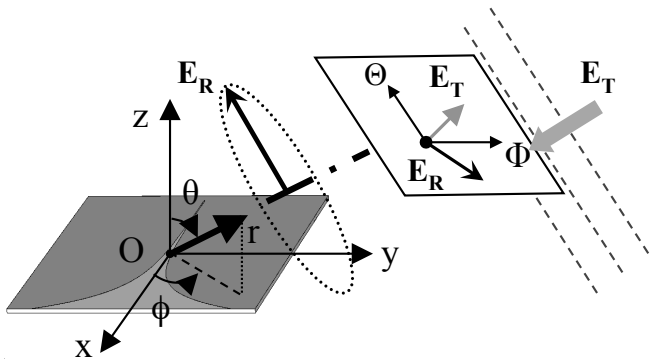

Fig. 6-12. Tag in presence of an incoming plane wave.

As before a straightforward application of the reciprocity theorem [8] leads to the following form generated by the relationship between the fields and associated currents:

$$I_{\mathrm{A}}(\omega) = j\frac{2}{\eta}\lambda Y_{\mathrm{A}}(\omega)\,\mathbf{E}_{\mathbf{Rn}}(\theta_{\mathrm{A}},\phi_{\mathrm{A}};\omega)\bullet\mathbf{E}_{\mathbf{T}}(r,\theta_{\mathrm{I}},\phi_{\mathrm{I}};\omega) \tag{6.17}$$

where I_A still plays the role of free source in the receiver analysis. $Y_A(\omega) = \left[R_A(\omega)\right]^{-1}$ is the frequency-dependent antenna admittance, r is the read range, (θ_1, ϕ_1) the angular coordinates of the direction of incidence of $\mathbf{E_T}$ in its respective reference frame and η is the free-space impedance.

The radiated far-field distribution $\mathbf{E_R}(r_A, \theta_A, \phi_A; \omega)$ as well as $Y_A(\omega)$ are derived by EM simulations through an arbitrary excitation by a current density I injected at the input port. Then the normalized field $\mathbf{E_{Rn}}$ is considered:

$$\mathbf{E_{Rn}}\left(\theta_A, \phi_A; \omega\right) = r_A \exp\left(j\beta r_A\right) \frac{\mathbf{E_R}\left(r_A, \theta_A, \phi_A; \omega\right)}{I} \tag{6.18}$$

where r_A is the generic distance at which $\mathbf{E_R}$ is evaluated.

By means of such approach a first evaluation of the effective read range can be performed by starting from some average values of radiated power from the transmitter: with 23 dBm ERP the required -14 dBm power level to the Alien chip can be guaranteed at about 15 cm distance. At the same distance by making use of (6.15) the backscattered signal power is proven to fulfill a standard reader sensitivity of roughly -80 dBm (a huge noise contribution among the entire block chain should be considered).

The atmospheric attenuation (15 dB/km at 60 GHz) can be neglected, because distances are small. For 1 m radio path length the additional attenuation due to atmosphere is 0.015 dB.

Of course the read range might be considerably increased through a suitable active device at the reader side, such a high-gain power amplifier. Using a more directive reader antenna would increase the TX power to 30 dBm ERP, a power level comparable to a standard UHF RFID reader output. This would extend the range to 30 cm. Adding a higher gain tag antenna would also extend the range: e.g. a 2×2 patch antenna provides 4-fold gain, or 2-fold range compared to a single patch, or a Vivaldi. The array is similar to UHF RFID tag antennas in size (5×5 cm^2). Further, using a semipassive tag IC, the tag sensitivity could be reduced at least 12 dB. Because the conversion loss also scales in the incoming power, this would only give two-fold range extension. Hence the range can be extended to over a meter. Capacitive mixing might help to extend the range further, especially with the extremely low input power of semipassive UHF RFID tags.

Measurements

Forward link measurements

The forward link conversion gain was measured by means of a continuous wave feeding system: a block scheme is given in Fig. 6-13, with the authentic tag load replaced by the – suboptimum – 50-Ohm spectrum analyzer input impedance. For the measurement, a new matching network at IF was implemented (L_1 = 3.3 nH, L_2 = 22 nH, C = 4.6 pF) to match the 50-Ohm load to the diode.

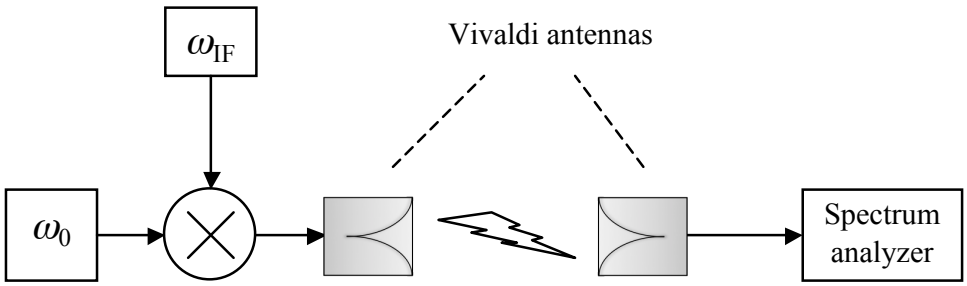

Fig. 6-13. Forward link measurement setup.

In the measurements, the power of the carrier at ω_0 and the upper sideband $\omega_0 + \omega_{IF}$ were tuned to -10 dBm at the diode input. The lower sideband power at $\omega_0 - \omega_{IF}$ was allowed to vary a few dB, in order to keep the carrier and upper sideband powers constant. The measured conversion gain is presented in Fig. 6-14 as a function of IF frequency.

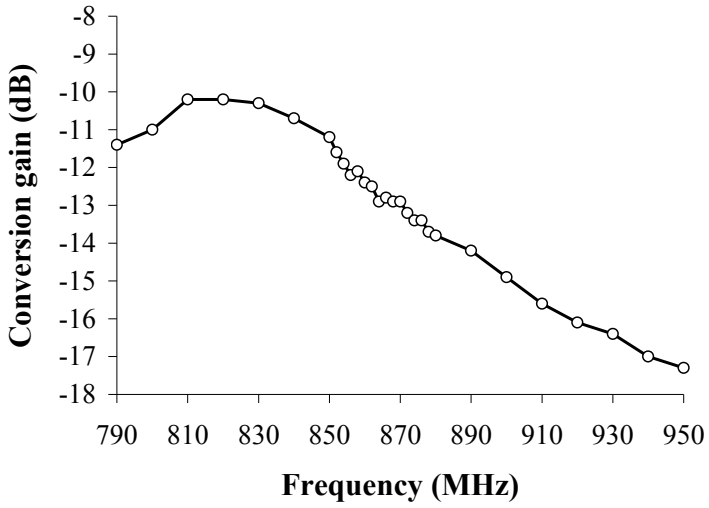

Fig. 6-14. Measured conversion loss of the diode at -10 dBm input power at carrier and upper sideband as a function of the IF frequency.

The IF matching is at its best at 820 MHz, were a conversion loss of about -10 dB is achieved. The conversion loss at the nominal operation frequency of 860 MHz is 2.2 dB lower.

Full operation

A full system as depicted in Figs. 6-15 and 6-16 was constructed for determining the actual read range: for sake of simplicity two-element Vivaldi array is employed as a transceiver at the reading side. Setup enhancements include two high-gain power amplifiers positioning (Quinstar QPJ and Miteq JS4) and tuning of reader RX and TX antenna separation as well as reader output power control at the RFID reader in order to keep the optimum feeding condition $A_1 = A_2$. The transmit power in the measurement is about 30 dBm ERP along all the frequency range.

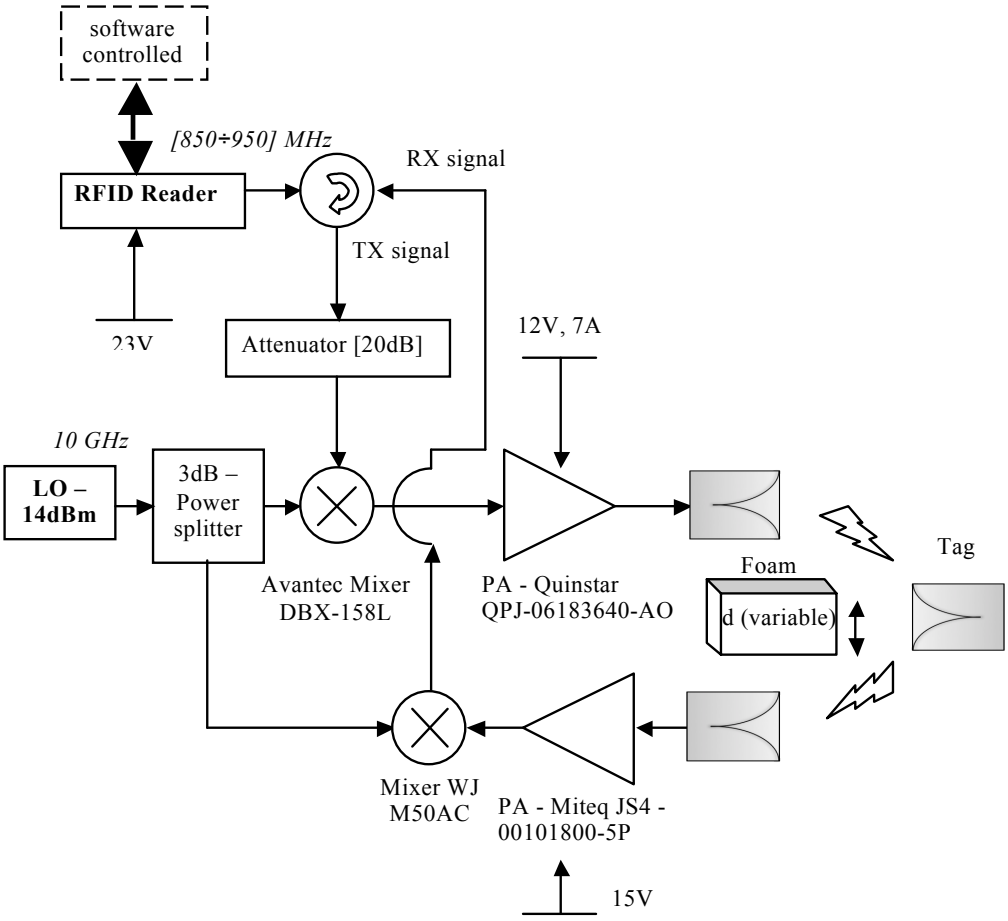

Fig. 6-15. Read range measurement setup schematic.

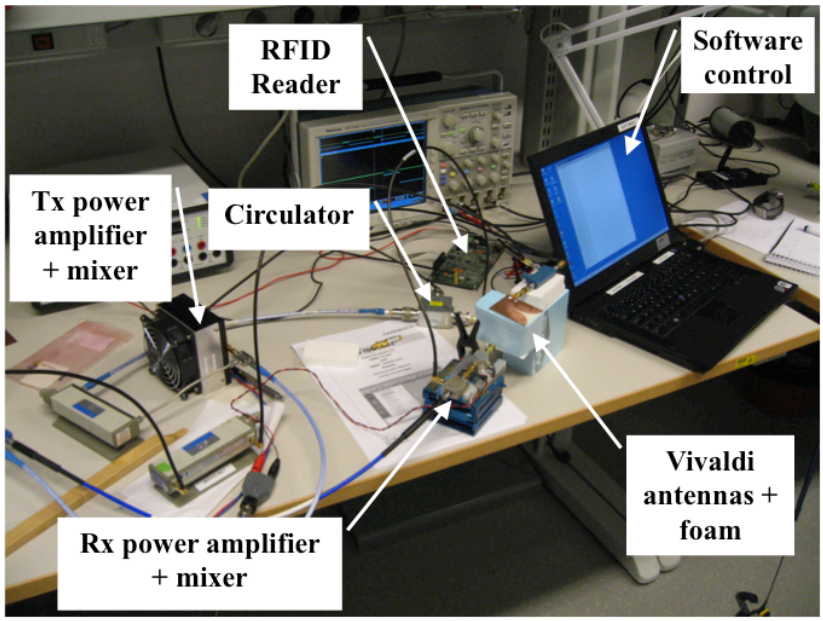

Fig. 6-16. Read range measurement setup photograph.

The measured tag range was about 30 cm. About 5 cm longer range was observed with the first query of the EPC protocol than with the acknowledgement including the EPC code. The IF frequency sweep in Fig. 6-17 shows high variation of the read range, which is probably due to two reasons: first, the laboratory demonstrator measurement setup can give rise to standing waves and multipath propagation, effects that are enhanced by the higher carrier frequency. Secondly, the power of the up-converted RFID reader signal was frequency dependent, leading to manual adjustment of the output power of the RFID reader at every frequency point. In addition to this, the achieved suppression of the lower sideband at ω_0 - ω_{IF} in the antenna and matching network was lower than expected. Hence the lower sideband propagates somewhat to the diode, contributing to the mixing results. Taking into account these non-idealities in the measurement setup, the measured results are in line with the simulated range.

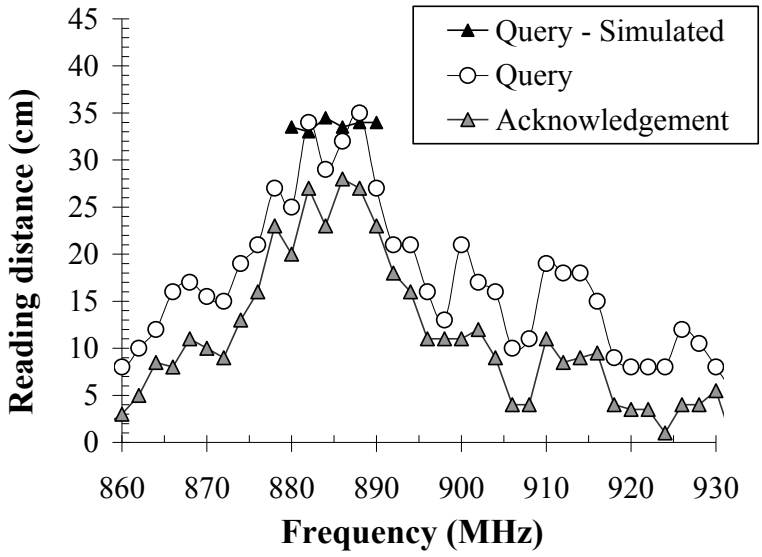

Fig. 6-17. Measured read range as a function of IF frequency.

REFERENCES

[1] J. S. Choi, H. Lee, R. Elmasri, D. W. Engels, "Localization Systems Using Passive UHF RFID," *INC, IMS and IDC, 2009. NCM '09. Fifth International Joint Conference*, Seoul, pp.1727-1732, Aug. 2009.

[2] P.V. Nikitin, R. Martinez, S. Ramamurthy, H. Leland, G. Spiess, K. V. S. Rao, "Phase based spatial identification of UHF RFID tags," RFID, *2010 IEEE International Conference on RFID*, Orlando, pp. 102-109, Apr. 2010.

[3] Viikari, P. Pursula, K. Jaakkola, “Ranging of UHF RFID Tag Using Stepped Frequency Read-Out”, *IEEE Sensors Journal*, vol. 10, no. 9, pp. 1535-1539, Sep. 2010.

[4] P. Pursula, T. Vähä-Heikkilä, A. Müller, D. Neculoiu, G. Konstantinidis, A. Oja, J. Tuovinen, “Millimetre Wave Identification — new radio system for low power, high data rate and short range”, *IEEE Tr. on Microwave theory and techniques*, Vol. 56, No. 10, pp. 2221-2228, Oct. 2008

[5] D. Neculoiu, G. Konstantinidis, T. Vähä-Heikkilä, A. Müller, D. Vasilache, A. Stavinidris, L. Bary, M. Dragoman, I. Petrini, C. Buiculescu, Z. Hazoupulos, N. Kornilios, P. Pursula, R. Plana, D. Dascalu, “GaAs Membrane-Supported 60 GHz Receiver with Yagi-Uda Antenna,” *MEMSwave 2007, 8th International Symposium on RF MEMS and RF Microsystems*, Barcelona, pp. 15-18, Jun. 2007.

[6] S. Pellerano, J. Alvarado, Y. Palaskas, "A mm-wave power harvesting RFID tag in 90nm CMOS," *Custom Integrated Circuits Conference CICC*, San Jose, Sep. 2009, pp.677-680.

[7] P. J. Gibson, “The Vivaldi aerial,” *Proc. 9th European Microwave Conf.*, pp. 101–105, 1979.

[8] V. Rizzoli, A. Costanzo, G. Monti, “General electromagnetic compatibility analysis for nonlinear microwave integrated circuits”, *2004 IEEE MTT-S Int. Microwave Symp. Digest*, Fort Worth, TX, pp. 953-956, June 2004.

TRANSPONDERS FOR MILLIMETER WAVE IDENTIFICATION

Radio frequency Identification at millimeter waves enables new applications, such as high data rate short range communication and location sensing through narrow-beam antennas. In this chapter a tag consisting of a Schottky diode and an antenna and front-end on liquid crystal polymer (LCP) is presented. Then the design and fabrication of the tag is compared to a much more expensive LTCC-based counterpart.

The study has been carried out in a 6-month stage at VTT Technical Research Centre of Finland (Espoo, Finland).

Motivation

Lyquid crystal polimer technology

As frequencies tend to increase for the next generation of wireless applications, new types of materials are emerging as new potential substrate technologies.

Some of the requirements are ordinary such as low cost, low losses and mechanical stability, chemical resistance and multilayer lamination capabilities and be cost competitive. But at millimeter-wave frequencies also water and gas permeability characteristics must be included for acceptable long service lifetimes: for example as circuits get smaller material expansion related to material's water absorption can seriously affect functional reliability [1].

Microwave composites such as variations of Rogers Duroid or Taconic RF series materials use proprietary mixes of materials like polytetraflouroethylene (PTFE), glass weave and ceramic fills. These engineered materials can offer excellent electrical properties but at the same time they result being too much expensive. Alumina is likewise attracting for high frequency applications due to its zero-water-absorption characteristics. Nevertheless dielectric constant near 10 makes it not-ideal for antenna application and another drawback is its high sensitivity towards temperature.

Low-temperature co-fired ceramics (LTCC) is one of the very few substrate technologies that satisfy all the requirements above. Advantages are a stable dielectric constant among a wide range of frequencies (RF up to mm-wave), low dielectric loss up to mm-wave frequencies, vertical integration capability with high number of layers, excellent packaging characteristics and very low water and moisture absorption properties. All these features

makes it a very attractive material technology for applications that require the greatest functionality in the smallest footprint, such as wireless handsets.

But LTCC is not ideal for any kind of application: the relatively high dielectric constant – $\varepsilon_r \in [5.4 \div 9.1]$ – make the material not suitable for antenna application because of a reduced radiation efficiency. Antenna performances are particularly problematic since most of mm-wave antenna applications are in the automotive area – e.g. collision radar – where an important addictional contribute to free-space attenuation is given by atmospheric absorbtion of electromagnetic energy.

And one of the most serious disadvantage of LTCC technology is its process temperature (800 ÷ 1000°C) – not acceptable for some fully integrated solutions: MEMS and many unpackaged chips which contain the active devices cannot survive such temperatures. For instance one of the major manufacturing philosophies, *System-in-Package* (SiP) fabrication process, is based on a single packaging phase after mounting all the required chips on a dielectric substrate. A separated packaging procedure to overcome temperature would increase seriously the overall cost and consequently the major advantage of such approaches would be obviously lost [1]. So new technologies become necessary.

Liquid crystal polymer (LCP) [2] is a well suited candidate for that matter, with excellent packaging characteristics and all the manufacturing difficulties completely overcome in the last few years. LCP is a unique combination of desired properties for RF applications: it can be employed as a package and substrate because it is quasi-hermetic; it is cheaper than ceramics and other composite materials; and it is capable of homogeneous multilayer lamination so it can be diffusely employed in complex transceiver modules.

In addition stable electrical properties, excellent electrical prooperties ($\tan\delta$ = 0.002-0.005 up to 110 GHz) low processing temperature (ca. 285°C) and low cost make it ideal for a material for integrated RF systems also for antenna applications. Finally the mechanical flexibility of LCP material can produce aerospace applications where antenna arrays can be conformed to the aircraft fuselage or other external surfaces (Fig. 7-1).

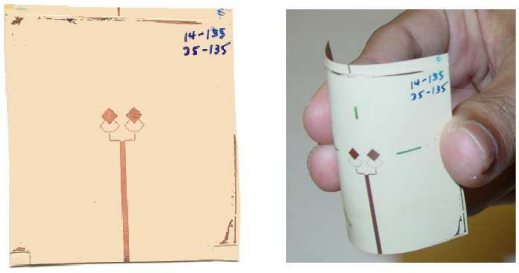

Fig. 7-1. Example of 2×1 microstrip-fed array from the Georgia Institute of Technology.

Many examples of design, implementation and measurement of mm-wave devices on multilayer LCP technology have been developed at the Georgia Institute of Technology [1], [3] which demonstrated the great versatility of LCP material for a wide class of passive components and antennas.

Millimeter-wave indentification: generalities

As described in the last chapter, Ultra High Frequency Radio frequency identification (UHF RFID) has rapidly spread throughout the industry during the last decade and especially in logistic applications. Most recent developments has brought the reading range up to 10m with a data rate of 640 kbit/s.

Millimeter-wave frequency identification (MMID) is a similar concept, but updated to millimeter waves.

There are many reasons for such preference: at millimeter waves, e.g 60 GHz, high-data-rate can be implemented with a dramatic enhancement of the link channel capacity. Furthermore, at millimeter waves, directive antennas are small and easy to integrate. Today's UHF RFID systems lack of localization capabilities because directive antennas are too large at their working frequencies (see previous chapter). A directive antenna would considereably help in locating transponders in high-density sensor networks or other places where transponders are densely located. Some examples of RFID at microwaves have been alrealy demonstrated, at 24 GHz [4], 60 GHz [5] and 77GHz [6].

Automotive applications offer a great range of opportunities given that millimeter-wave radars are already used and in principle they might be inexpensively converted into MMID reader devices. The scaling of CMOS process technologies up to 60 GHz [7] allows promising development perspective in the research field.

Working principle

Both MMID and RFID systems are based on a backscattering mechanism for transmitting data from the tag to the reader. The semipassive tag topology is shown in Fig. 7-2:

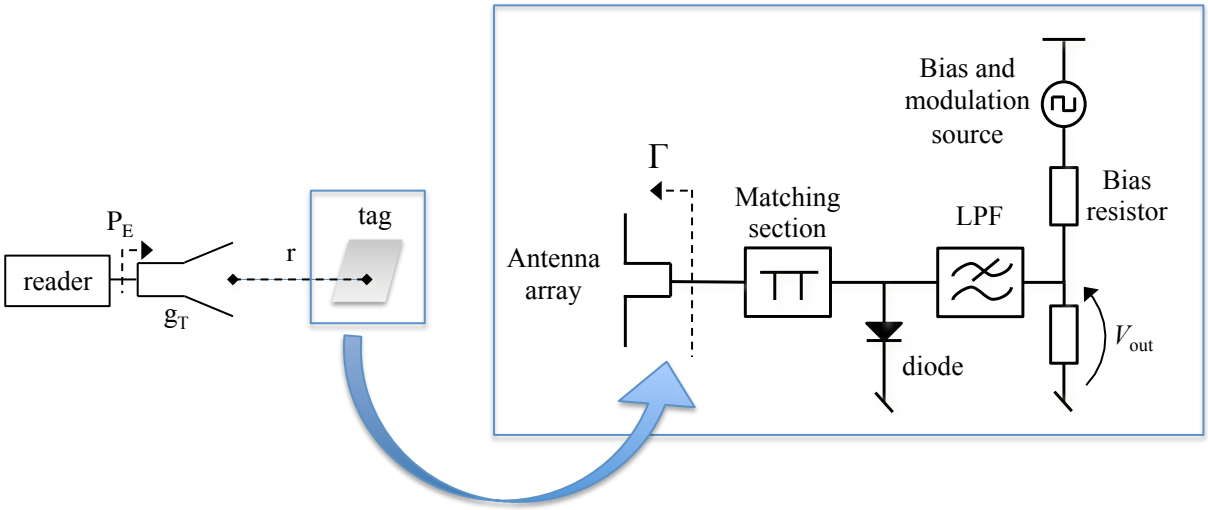

Fig. 7-2. Block diagram of the MMID transponder

A variation in diode bias conditions allows the tag to assume different mm-wave impedance states at the diode section. The backscattered power is proportional to the impedance matching between the antenna and the receiver diode. Thus, by changing the diode impedance, the backscattering of the tag can be modulated.

To formalize these concept the well known radar equation for the power P_R at the receiving antenna terminals can be stated as [8]:

$$P_R = P_E g_T^2 \frac{\lambda^2}{64\pi^3 r^4}\sigma \tag{7.1}$$

The formulation of (7.1) directly follows the application of reciprocity theorem from a link budget perspective: g_T is the reader antenna gain, P_E the input power at the terminals of the transmitting antenna, λ the free-space wavelenght at the working frequency and r the reciprocal distance between reader and tag. The expected term for polarization mismatch will be neglected for brevity – more in detail considering two rectilinear polarization antennas at the reader and tag side. σ is defined as *radar cross-section*: under the hypothesis of unique TEM port at the tag side, the expression is

$$\sigma = \frac{\lambda^2}{4\pi} g_0^2 \left| A - \Gamma \right|^2 \tag{7.2}$$

through which two separated scattering terms can be isolated: a structural named generically A (for the antenna topologies here considered the assumption is $A \approx 1$ in far-field region) and not dependent to the antenna load. Then a reflection coefficient Γ at the antenna port. g_0 is the transponder antenna gain.

Assuming a fixed bias level, the tag can first operate as a voltage detector in order to demonstrate a basic practicality. In this case the action is to convert amplitude-modulated microwave signals to baseband (or video) signals, generally providing a signal that is of one polarity, either all positive or all negative, to a bypass capacitor (usually directly provided by the test instruments at their input such as oscilloscopes), with an amplitude proportional to the input power level:

$$V_{\text{out}} = \beta_{\text{V}} \frac{\left\| \mathbf{E}_{\text{inc}} \right\|^2}{2\eta} \delta \frac{\lambda^2}{4\pi} d(\theta_{\text{C}}, \phi_{\text{C}}) \tag{7.3}$$

where δ is Tag antenna radiation efficiency, $d(\theta_{\text{C}}, \phi_{\text{C}})$ the antenna directivity towards the direction of arrival of the incoming $\mathbf{E}_{\text{inc}}$, and β the socalled responsivity - according to [9] a measure of gain for the detector in terms of power in vs voltage out. In terms of power in vs current out and it is called current responsivity.

$$\beta_{\text{V}} = \frac{\left| \Delta V_{\text{out}} \right|}{P_{\text{R}}} \tag{7.4}$$

(7.4) can be defined as the ratio between the detected current ΔV, time average increment in voltage due to the application of microwave power.

On the other hand MMID backscattering operation requires to have two different load impedances at the transponder: assuming a square wave modulation between two impedance states, namely Γ_1 and Γ_2, in [5] the expression for the radar cross-section is furnished:

$$\sigma^m = \sigma_0 + \sigma_m = \frac{g_0^2 \lambda^2}{4\pi} \left| 1 - \frac{1}{2} \left(\Gamma_1 + \Gamma_2 \right) \right|^2 + \frac{g_0^2 \lambda^2}{16\pi} \left| \Gamma_1 - \Gamma_2 \right|^2 \tag{7.5}$$

The first term (σ_0) of the radar cross-section describes scattering at the carrier frequency, and the other term (σ_m) describes scattering that carries information at the sideband frequencies. Now the contradiction between good matching and high modulation is evident. The higher the difference between the modulation states, the higher the scattered power, but lower the power transferred to the load. The quantity $|\Delta\Gamma|$ between the two possible states significantly affects the read/write sensitivity in any identification tag.

In conclusion a single millimeter diode can act as a detector and a modulator in uplink operation by means of bias modulation. In the second case the switching operation requires a fast device such as a diode or a transistor-based switch. An optimal choice would be a zero-bias detector diode providing low-power consumption while waiting for reader commands.

For its simplicity and low power consumption a Schottky diode is here employed.

Transponder design

One of the most significant advantages of MMID technology is the opportunity to integrate small directive antenna inside the chip with a relative small effort. The present topology already presented by [10] can provide excellent performances at the working frequency of 60 GHz: Fig. 7-3 and 7-4 provide for a top view and the radiation patterns for E- and H-plane respectively.

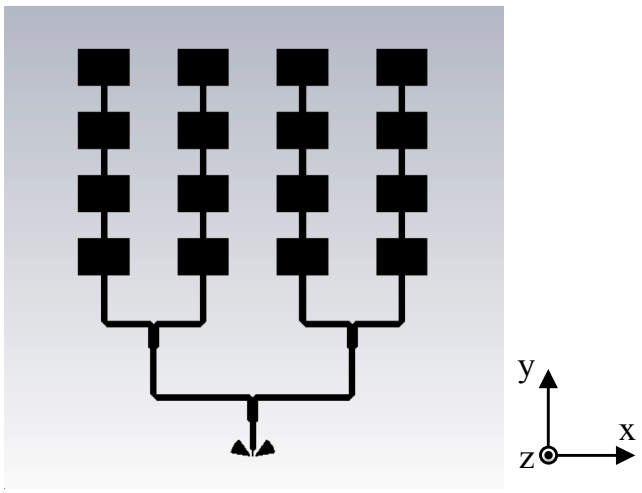

Fig. 7-3. 4×4 patches antenna layout, with radial stubs at the antenna port for S-parameter measurements with a probe station.

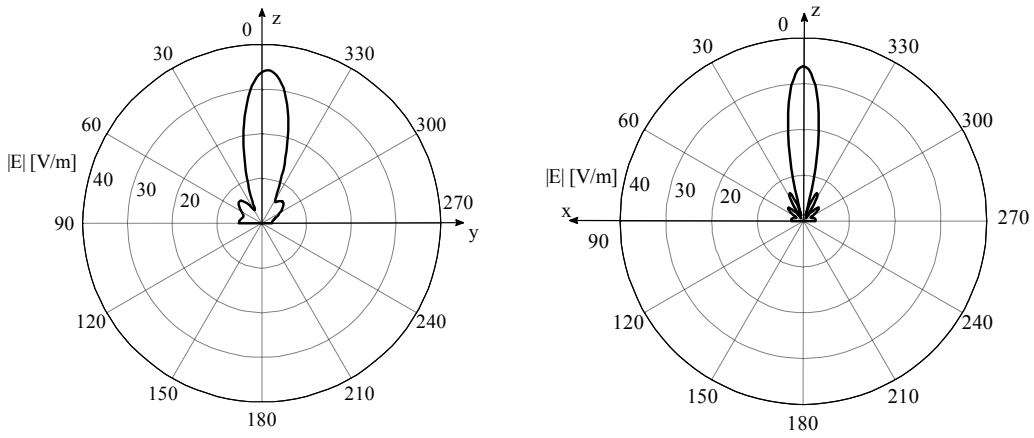

Fig. 7-4. Simulated radiation patterns on (a) E-plane and (b) H-plane

Provided that the four patch elements on each branch are not perfectly fed in-phase a fine tuning for width (W) and length (L) of each element and array step (L_s) is considered for a correct broadside behaviour: through intensive electromagnetic simulations carried by HFSS, final values are found to be W = 2 μm, L = 1.43 μm and L_s = 2.43 μm. The power splitter replaces the common Wilkinson divider in order not to deal with a lumped resistor of 100 Ohm. The result is a directivity of more than 18 dB among the frequencies of interest. The LCP substrate is Rogers UltraLam3850 (h = 100 μm, Cu thickness =5 μm, ε_r = 2.9, tanδ = 0.0025).

By means of 50-Ohm mmwave probe pad based on CBCPW-to-microstrip line transition, the simulated antenna return loss is measured (Fig. 7-5), revealing a shift between the two peaks of just a little more than 2% of bandwidth.

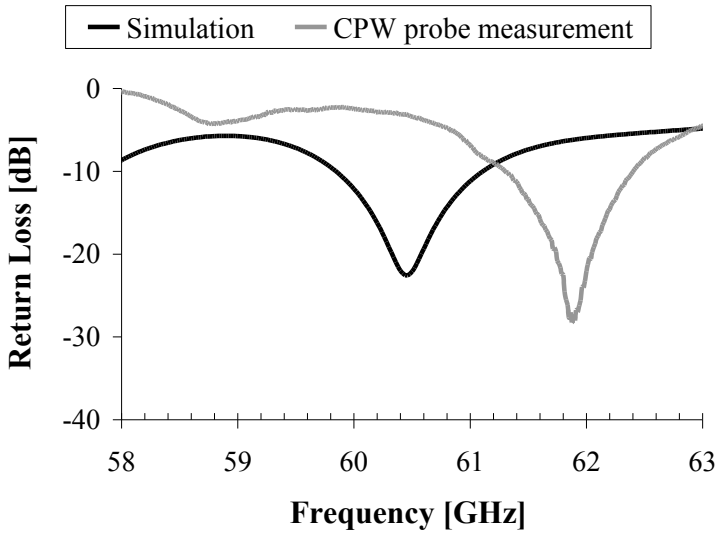

Fig. 7-5. Simulated and measured antenna return loss.

The core of the millimeter-wave front end is the nonlinear device Agilent GaAs HSCH-9162 Schottky diode. A correct nonlinear modeling requires an anti-parallel diode pair configuration, whose electrical specifications are series resistance R_{S_1} = 50 Ohm, saturation current I_{S_1} = 12 μA, zero-bias junction capacitance C_{j0_1} = 0.03 pF and ideality factor $N_{\_1}$ = 1.2 for the forward device and R_{S_2} = 10 Ohm, I_{S_2} = 84 μA, C_{j0_2} = 0.03 pF and $N_{\_2}$ = 40 for the reverse one. All those values found correspondence with measurement during specific semiconductor device testing:

The detector is basically placed in parallel between a 60 GHz matching section towards the antenna side and two radial-stub-based low pass filters positioned on both cathode and anode. A further radial stub inserted near the anode does provide for a virtual DC return, thus avoiding challenging via-holes on LCP material.

The whole front-end is depicted in Fig. 7-6:

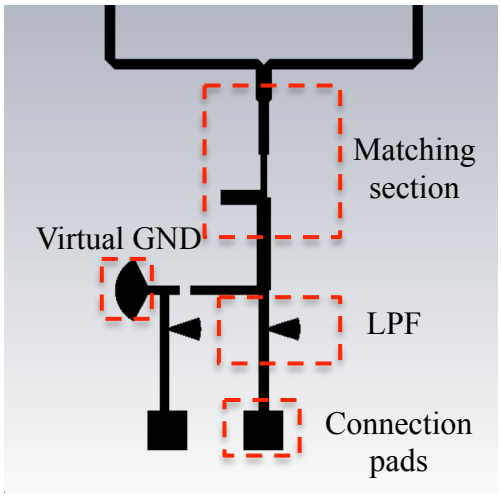

Fig. 7-6. Matching network layout

LPF (Fig. 7-7) and virtual ground plane are studied separately, then inserted in the whole front-end:

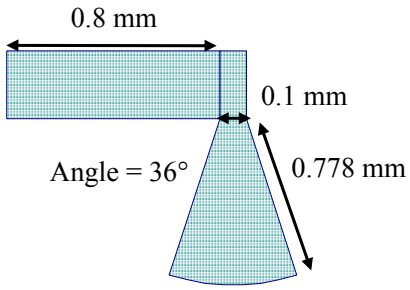

Fig. 7-7. Radial-stub-based LPF with dimensions in mm

On the other hand the main project guideline for matching circuit is to guarantee for fixed levels of diode biasing a suitable return loss $|\mathbf{S}_{11}|$, while phase values $\arg(\mathbf{S}_{11})$ ensure good modulation depth during backscattering operation. Supposing video shunt resistance equal to 10 MOhm between the two connection pads and a reference available power level of -5dBm at the tag antenna terminals, the final results of the nonlinear optimization process are shown in Fig. 7-8 for two distinct diode bias levels.

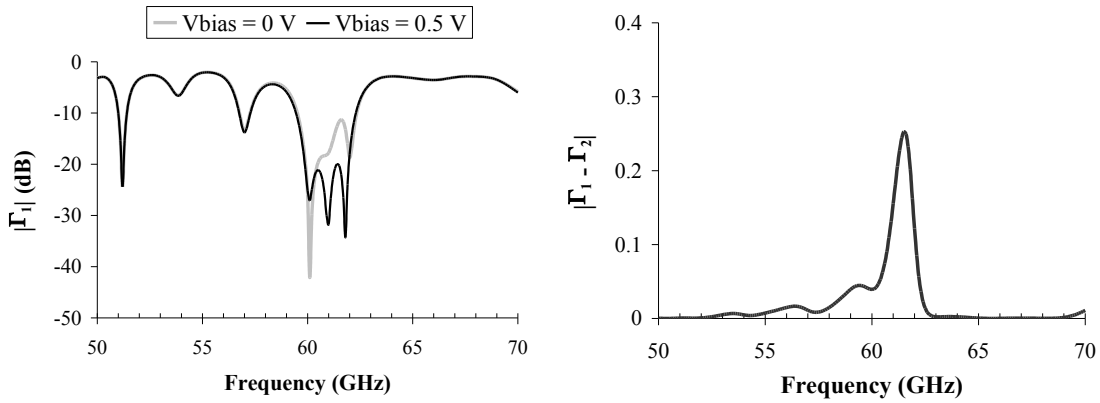

(a) (b)

Fig. 7-8. Simulated (a) LCP transponder matching, (b) modulated reflection coefficient

Between 60 and 62 GHz a good matching is guaranteed for the incoming signal while a 20% shift between the two impedance levels looks promising for uplink modulation – by the designer's knowledge.

Low pass filter at each terminal ensures the RF tune to be cut off at the baseband pads section by means of an isolation of 30 dB. Scattering from pads can be neglected.

Measurements

For comparative purposes two similar tags are evaluated on the same downlink and uplink scenario: the one presented, based on LCP technology substrate, and one built on LTCC material with a resonant backward diode. The latter represents a high-end solution with a highly sensitive diode on an expensive but high-performance substrate.

The LTCC module takes advantage of the proved multilayer properties of the LTCC technologies. The aperture coupled 2×2 uses four layers of Ferro A6-S LTCC material, and Wilkinson power dividers were used in the binary feed network. The antenna arrays are similar to the one shown in [11] but 4 array elements were used instead of 16. The simulated working band is in the range [58.8 ÷ 62.6] GHz and gain up to 11 dBi at 61 GHz.

The resonant backward diode is manufactured by HRL [12]. It has excellent curvature and responsivity at zero bias. The diode is supplied as bare die, which is flip chip connected to the LTCC substrate.The module is shown in Fig. 7-9 at the antenna side and the bottom view with the feed area network in evidence.

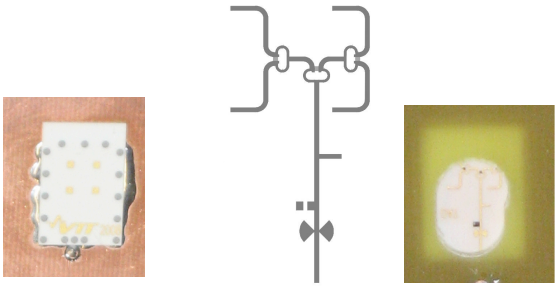

(a) (b) (c)

Fig. 7-8. LTCC tag: (a) photograph of the antenna element side, (b) photograph of the feed network side, (c) schematic of the feed network.

Then the optimization results previously acquired for such tag are furnished in Fig.7-9.

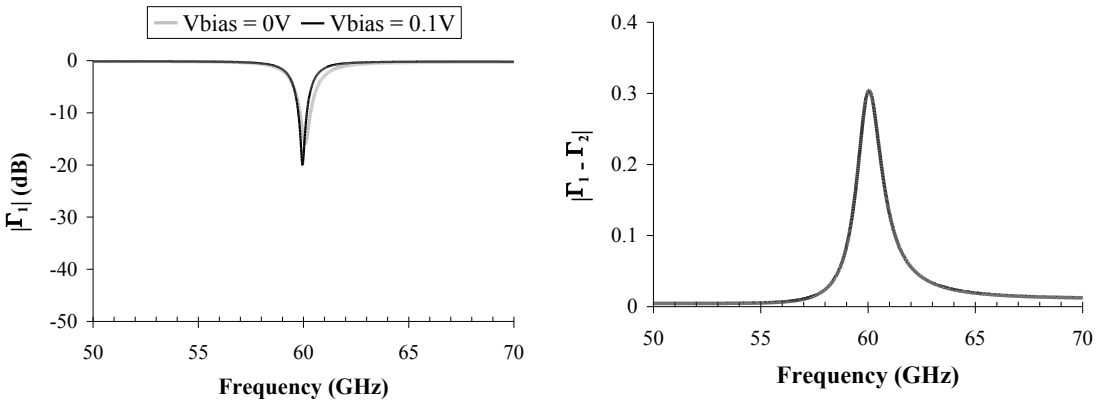

(a) (b)

Fig. 7-9. Simulated (a) LTCC transponder matching, (b) modulated reflection coefficient

In Fig. 7-10 the conceptual scheme of the downlink setup is furnished. A modulated 60 GHz signal is transmitted to a transponder using a waveguide-based laboratory transmitter, consisting of a modulated signal generator (Agilent E8257C), multiplier (HP83557A) and a horn antenna (Quinstar). An oscilloscope - possibly aided by a LNA at the receiver side - is used to monitor the envelope of the amplitude modulated transmitted signal.

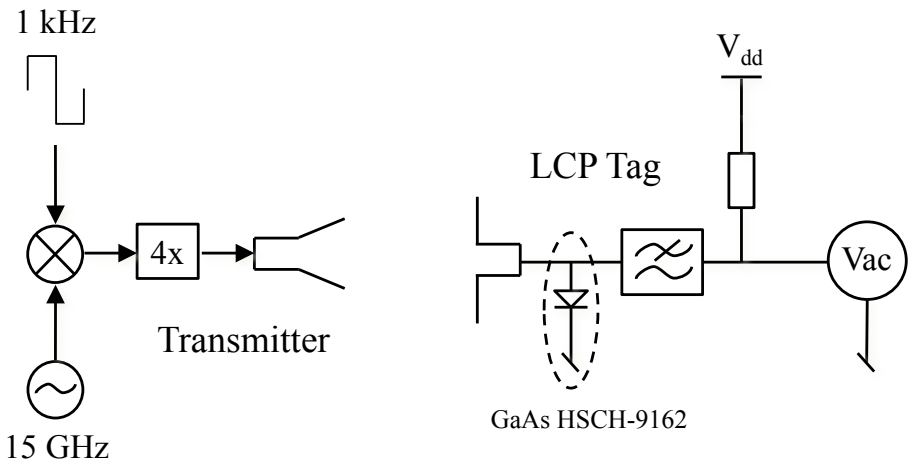

Fig. 7-10. Setup for downlink measurement

The setup - mostly due to many contributes to the overall noise figure by some elements - is obviously not suitable for real data transfer applications but enables measuring the backscattered power levels of the transponder.

The output voltage of the diode, as previously stated, is measured to characterize the diode as a receiver. The transmitted power varies between 6 dBm and 12 dBm and the distance is between 20 and 25cm. The results in Fig. 7-11 show that the backward diode is an order of magnitude better in sensitivity.

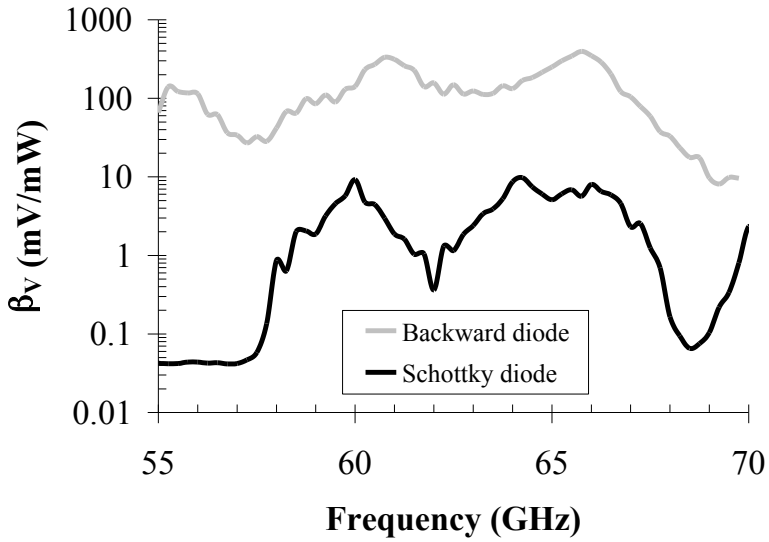

Fig. 7-11. The measured diode responsivities

The uplink experiment (Fig. 7-12) is used for demonstrating the MMID concept in a similar manner: the goal is to demonstrate modulated backscattering from the transponder. As

before the reader consists of a waveguide-based transmitter and receiver. The former is the same than in downlink experiment. The receiver consists of a signal generator (HP83650A), a multiplier (Spacek Laboratories AV-4XW), a mixer (Spacek Laboratories PV-VB), isolators, and a horn antenna.

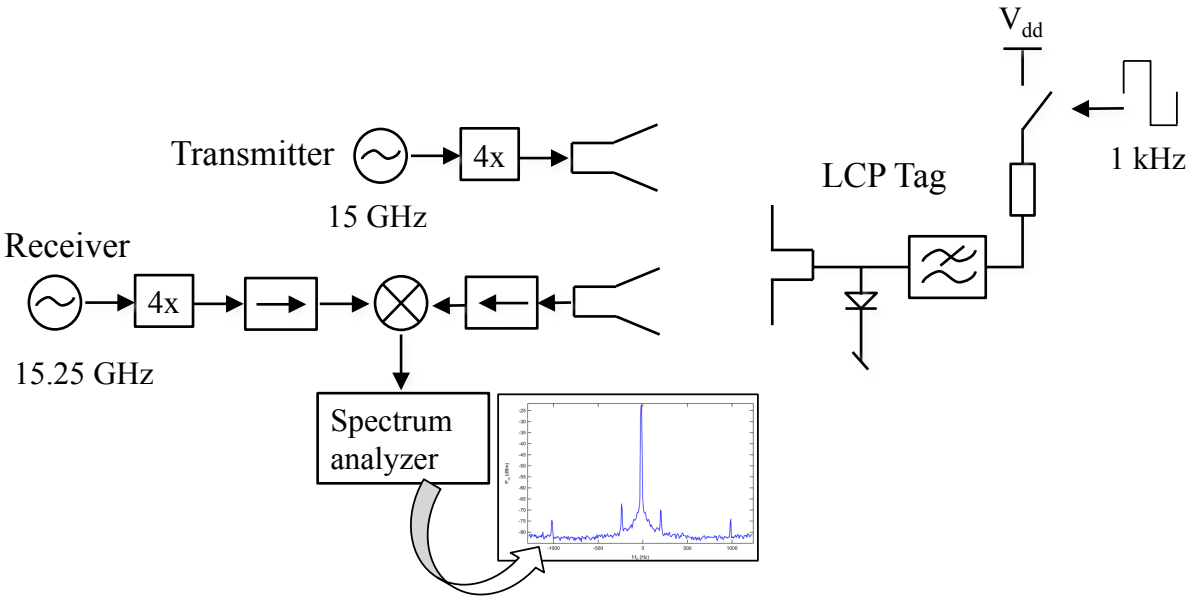

Fig. 7-12. Setup for uplink measurement

A 60 GHz continous wave signal transmitted by the reader is modulated by the transponder and the backscattered signal is received and monitored by the reader after a down-conversion to 1 GHz. The outputs of the spectrum analyzer are shown in Fig. 7-13, with a baseband modulation frequency of 100 kHz and 1 kHz respectively – the LTCC antenna intrinsecally provides wider bandwidth, because of the aperture-coupled antenna topology.

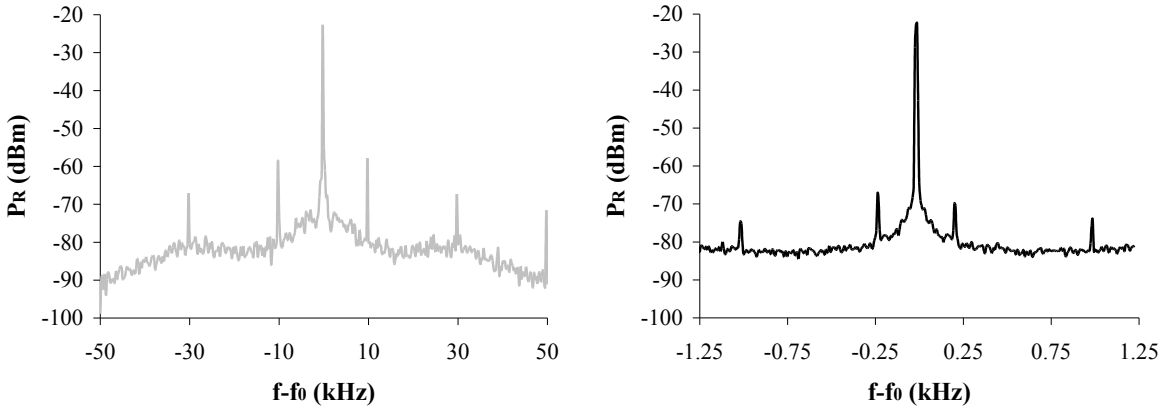

(a) (b)

Fig. 7-13. Received scattered power of (a) the LTCC transponder with a modulation frequency f_{mod} = 10 kHz, (b) the LCP transponder with a modulation frequency f_{mod} = 1 kHz

LTCC transponder is definitely more sensitive as a receiver, but the backscattered principle is roughly demonstrated for both tags. The LTCC is however much more expensive compared to the LCP, which can be fabricated with standard PCB processes. A detailed comparison between the two technologies can be found in [13].

The HRL diode is more expensive than the Schottky (~20 $ a piece, small quantities), but allows zero bias detection. The backward diode is a bare die, and requires flip chip assembly, whereas the Schottky is delivered in beam lead package allowing reflow-type assembly.

REFERENCES

[1] D. C. Thompson, "Characterization and Design of Liquid Crystal Polymer (LCP) Based Multilayer RF Components and Packages", Ph. D. dissertation, Georgia Institute of Technology, Atlanta, 2006.

[2] L. M. Higgins III, "Hermetic and Optoelectronic packaging concepts using multiplayer and active polymer systems," *Adv. Microelectron.*, vol. 30, no. 4, pp. 6–13, Jul./Aug. 2003.

[3] R. Bairavasubramanian, "Development of microwave/millimeter-wave antennas and passive components on multilayer liquid crystal polymer (LCP) technology", Ph. D. dissertation, Georgia Institute of Technology, Atlanta, 2006.

[4] E. M. Biebl, “RF systems based on active integrated antennas,” *Int. J. Electron. Commun. (Arch. Elektr. Ubertragung),* vol. 57, no. 3, pp.173–180, 2003.

[5] P. Pursula, T. Vähä-Heikkilä, A. Müller, D. Neculoiu, G. Konstantinidis, A. Oja, J. Tuovinen, “Millimetre Wave Identification — A New Short-Range Radio System for Low-Power High Data-Rate Applications”, *IEEE Transactions on Microwave theory and techniques*, vol. 56, no. 10, pp. 2221-2228, Oct. 2008.

[6] A. Müller, D. Necoliou, P. Pursula, T. Vähä-Heikkilä, F. Giacomocci, J. Tuovinen, “Hybrid integrated micromachined receiver for 77 GHz millimeter wave identification systems”, *the 37th European Microwave Conference*, Munich, Germany, Oct. 2007, pp. 1034-1037.

[7] S. Pellerano, J. Alvarado, Y. Palaskas, "A mm-wave power harvesting RFID tag in 90nm CMOS," *Custom Integrated Circuits Conference CICC*, San Jose, Sep. 2009, pp.677-680.

[8] C. A. Balanis, Advanced Engineering Electromagnetics. New York: Wiley, 1989.

[9] A. M. Cowley, H.O. Sorenson, “Quantitative Comparison of Solid-State Microwave Detectors,” MTT-14, No. 12, pp. 588- 602, Dec 1966.

[10] S. Cheng, P. Hallbjörner, A. Rydberg, “Array Antenna for body-worn automotive harmonic radar”, *Proc. of the 3rd European Conference on Antennas and Propagation (EuCAP)*, Berlin, Germany, Mar. 2009, pp. 2823-2827.

[11] A. E. I. Lamminen, J. Säily, and A. R. Vimpari, “60-GHz patch antennas and arrays on LTCC with embedded-cavity substrates,” *IEEE Trans. Antennas Propag.*, vol. 56, no. 9, pp. 2865–2874, Sep. 2008.

[12] J. N. Schulman, D. H. Chow, "Sb-heterostructure interband backward diodes," *Electron Device Letters, IEEE* , vol.21, no.7, pp.353-355, Jul 2000.

[13] S. Dumanli, D. L. Paul, C. J. Railton, "LTCC or LCP, A comparison using cavity backed slot antennas with pin curtains at 60 GHz," *Proc. of the 4th European Conference on Antennas and Propagation (EuCAP)*, Barcelona, Spain, Apr. 2010, pp.1-5.

PUBLICATIONS

I. V. Rizzoli, D. Masotti, F. Donzelli, F. Mastri and R. Gaddi, "Nonlinear Modelling of Reconfigurable Microwave Components Based on Resistive MEMS Switches", *Proceedings of European Microwave Week Conference 2007*, pp. 611 – 61, October 2007

II. V. Rizzoli, D. Masotti, F. Donzelli, A. Costanzo, P. Spadoni and E.M. Vitucci, "A CAD Procedure for MIMO Link Estimation by the Combination of Nonlinear, Electromagnetic and Propagation Analysis Techniques", *2008 IEEE MTT-S International Microwave Symposium Digest,* pp. 927-930, June 2008.

III. V. Rizzoli, D. Masotti, F. Donzelli, F. Mastri and A. Costanzo, "Computer-Aided Investigation OF MEMS-Reconfigurable Microstrip Antenna Behaviour", *Union Radio Scientifique Internationale - XXIX General Assembly,* August 2008, Chicago, USA.

IV. V. Rizzoli, D. Masotti, F. Donzelli, A. Costanzo, "Una procedura automatica per il calcolo delle prestazioni di un intero link MIMO mediante la combinazione delle tecniche nonlineare, elettromagnetica e propagatoria", *Atti XVII Riunione Naz. Elettromagnetismo*, Lecce, settembre 2008.

V. V. Rizzoli, F. Donzelli, F. Mastri and A. Costanzo, "Efficient Circuit-Level Nonlinear Analysis of Interference in UWB Receivers", *Proceedings of European Microwave Week Conference 2008,* pp. 438 – 441, October 2008.

VI. V. Rizzoli, D. Masotti, F. Donzelli, A. Costanzo and G. Bichicchi, "CAD of Multi-Resonator Rectenna for Micro-Power Generation", *Proceedings of European Microwave Week Conference 2009,* pp. 331-334, October 2009.

VII. V. Rizzoli, D. Masotti, F. Donzelli, A. Costanzo, "Rigorous Design of RF Multi-Resonator Power Harvesters", *4th European Conference on Antennas and Propagation*, April 2010, Barcellona, Spain.

VIII. V. Rizzoli, D. Masotti, F. Donzelli, A. Costanzo and A. Lipparini, "Nonlinear/electromagnetic co-design of microwave transceivers including integrated antennas", *The Applied Computational Electromagnetics Society Annual Conference Proceedings*, pp.852-857, April 2010, Tampere, Finland.

IX. V. Rizzoli, D. Masotti, A. Costanzo e F. Donzelli, “Integration of numerical and field-theoretical techniques in the design of single- and multi-band rectennas for micro-power generation”, *EuMA International Journal of Microwave and Wireless Technologies*, Vol.2, pp. 293-303, July 2010.

X. V. Rizzoli, D. Masotti, A. Costanzo e F. Donzelli, “Nonlinear/electromagnetic co-simulation of microwave/millimeter-wave radio systems”, *International Workshop on Advances in Modeling and Optimization of High Frequency Structure,* August 2010, Reykjavik, Island.

XI. V. Rizzoli, D. Masotti, A. Costanzo, A. Lipparini e F. Donzelli, “Integrazione di Tecniche Numeriche e Teoria Elettromagnetica per la generazione di Micro-Potenze da Antenne Rettificatrici”, *Atti XVIII Riunione Naz. Elettromagnetismo*, Benevento, settembre 2010.

SUMMARY